Measurements of Dynamics, Structure, and Flexibility of Macromolecules by Pulsed Electron Spin Resonance

by

Soraya Pornsuwan

B.S., Mahidol University, 1997

M.S., University of Wisconsin, Madison, 2001

Submitted to the Graduate Faculty of

School of Arts and Science in partial fulfillment

of the requirements for the degree of

Doctor of Philosophy

University of Pittsburgh

2007

UNIVERSITY OF PITTSBURGH

FACULTY OF ARTS AND SCIENCE

This dissertation was presented

by

Soraya Pornsuwan

It was defended on

August 16, 2007

and approved by

David Pratt, Ph.D., Professor, Department of Chemistry, Faculty of Arts and Sciences

Megan Spence, Ph.D., Assistant Professor, Department of Chemistry, Faculty of Arts and Sciences

Pei Tang, Ph.D., Associate Professor, Department of Anesthesiology, School of Medicine

Dissertation Advisor: Sunil Saxena, Assistant Professor, Department of Chemistry, Faculty of Arts and Sciences

Measurements of Dynamics, Structure, and Flexibility of Macromolecules by Pulsed Electron Spin Resonance

Soraya Pornsuwan, PhD

University of Pittsburgh, 2007

This thesis discusses the measurement of molecular dynamics and distances in spin-labeled macromolecules by pulsed electron spin resonance (ESR). We present a scheme to reduce the dead-time in a commercial ESR spectrometer. This achievement facilitates the acquisition of the ESR signal even when it is largely reduced due to short relaxation times. As a result, we obtain the two-dimensional (2D) ESR signal for a nitroxide labeled peptide over a temperature range of 192 K to 310 K. In that temperature range, molecular reorientations over the range of 10^{-10} to 10^{-4} s are sampled. The phase memory time (T_m) is measured at each experimental temperature. The phase memory times, T_m, as a function of rotational correlation are calculated using spectral simulations based on the stochastic Liouville equation. By comparing the plots of T_m versus temperature obtained from experiment and theoretical models, the details of molecular dynamics are elucidated. This accomplishment expands the application of 2D ESR to the measurement of dynamics in large proteins.

The second part of this research employs a pulsed ESR technique, double electron-electron resonance (DEER), to measure large-scale distances in bis-peptide materials composed of 4-8 monomers. Constraints on overall structure and flexibility of the oligomers are rapidly determined by the end-to-end distance distribution measured from the DEER data. The distance distributions from DEER data are compared with those obtained from molecular dynamics (MD) simulations. Discrepancies between the DEER and MD results are evident, especially for longer

oligomers. In order to rapidly predict the shapes of the oligomers, we introduce a joint stiff-segment model to represent the oligomer backbone. A scheme is established to exploit information on the end-to-end distance distribution functions obtained by ESR to optimize the force fields used in the joint-stiff segment model. The results provide information on the distribution of orientations of a monomer with respect to the preceding monomer. The model gives parameters that better fit the ESR results than those originally obtained from the MD simulations. The results enhance our ability to predict the shapes and flexibility of new oligomers constructed using an arbitrary number of monomer units.

TABLE OF CONTENTS

LIST OF SCHEMES

LIST OF TABLES

LIST OF FIGURES

PREFACE

This thesis is dedicated to all my family members; my father, mother, sisters, and brother, and everyone who has touched my life during my years of study in the US.

First, I am very grateful to my advisor, Professor Sunil Saxena, for his invaluable guidance and support throughout the course of my doctoral study. Sunil has given me much insight into the research of electron spin resonance and taught me to grow as a scientist. His insight into science has been a constant resource of inspiration and I am very fortunate to have had an opportunity to learn from him. I thank him for his encouragement and patience for working with me. Being part of his group from the beginning has been an adventure. I am very proud of being witness to how the group has grown from the start.

I thank the members of my dissertation committee, Professor David Pratt, Professor Megan Spence, and Professor Pei Tang for their assistance and precious advice on my research activity. I also thank Professor David Pratt and Professor Gilbert Walker for their advice in my comprehensive exam. I thank Professor David Waldeck for guiding me as the mentor for my proposal defense. I am indebted to Professor Christian Schafmeister for the collaboration in the *bis*-peptide project, for the help in providing the results from molecular dynamics simulations, and for the discussion of the future directions of the project.

I am thankful to all of my peers in the Saxena group for their friendship, support, and all good times in Pittsburgh. Dr. Marco Bonora had trained me for the spectrometer and worked

closely with me for my first three years. Katherine Stone was the only group member when I joined the group; we stayed together since then, and I value her friendship. I thank Sangmi Jun and Yushin Kim for teaching me some Korean words; it was fun. Zhongyu Yang always helped me when I had some problems with calculations. I also thank Jessica Sarver and Katherine Stone for proofreading my thesis. Jim Becker was an excellent undergraduate, and I was lucky to interact with him. I also thank him and his family for the warm welcome on Thanksgiving for four years in a row. I want to thank all my folks I have met since my first year. I thank Dr. Abdil Ozdemir for his suggestion of how to survive in graduate school.

My family has given me immeasurable encouragement and support; my father, mother, sisters, and brother. I would not have made it to this point without them. I admire my mother for setting an example in taking good care of my father who has been paralyzed for the last five years. I would personally grant her double degrees in Nursing and Physical Therapy for that matter. All I could do is to dedicate this thesis to her courage and to my father.

I am indebted to all my mentors at the University of Wisconsin, Madison for teaching and guiding me to the next level of my Ph.D.; Professor Arthur Ellis, Professor Frank Weinhold, Professor Thomas C. Bruno, and Professor Gilbert Nathanson. I thank Dr. Vichai Reutrakul, the faculty at Mahidol University, and The Development and Promotion of Science and Technology Talents Project (DPST) for the academic foundation during my undergraduate degree, which has driven me towards the career in science.

1.0 INTRODUCTION

Electron spin resonance (ESR), a synonym of electron paramagnetic resonance spectroscopy, is a technique for studying chemical species that contain one or more unpaired electrons. After its first observation in 1945[1], ESR has become a well-known method for the examination of local structures of paramagnetic molecules. In its early stage, applications of ESR to the study of biological molecules were primarily limited to naturally occurring paramagnetic compounds, such as metalloproteins. Later, the method of incorporating an extrinsic electron spin using a spin-label became available,[2-4] but only for small synthetic molecules or for a few proteins that carry natural cysteine sidechains to which a spin label can be selectively incorporated.[5-10] Since 1990, when Hubbell and his co-workers[11-13] pioneered the work that combines site-directed mutagenesis with spin labeling, the corporation of spin labels in any specific location of proteins has been possible. The spin-labeling technique has expanded the use of ESR for the study of many different types of proteins. In principle, the ESR spectra of the spin-labeled macromolecules provide the key features of dynamics at the labeled site. This feature occurs due to the sensitivity of the ESR to the reorientation, modulated by the motion of the macromolecular chain, of the spin label in solution. In addition to the dynamics information, several ESR techniques have been developed for distance measurement between two specific sites on proteins for the purpose of facilitating structural determinations. The distance measurement techniques are limited not only to proteins but also to any type of macromolecules that carry two nearby

electron spins. This research thesis investigates both aspects of the ESR applications; dynamics and distance (structural) measurement on macromolecules. The following sections describe the fundamental features of ESR for those applications.

1.1 SITE DIRECTED SPIN LABELING

For proteins lacking unpaired electron spins, the addition of an extrinsic electron spin is possible by site-directed spin labeling (SDSL). The (1-oxyl-2,2,5,5-tetramethylpyrrolidin-3-yl) methyl methanethiosulfonate spin label, MTSSL, is the most common spin-label used in biological applications. Figure 1-1 shows the structure of MTSSL containing a stable unpaired electron spin, which is delocalized between the N-O bond of the nitroxide moiety. The spin label MTSSL is very reactive to the thiol group of a cysteine side chain. Thus, substitution of MTSSL for the native residue at a selected site can be accomplished by 1) cysteine substitution mutagenesis followed by 2) selective reaction of MTSSL forming a disulfide bond to the cysteine thiol group. Figure 1-1a shows the reaction of labeling the protein with the MTSSL, while Figure 1-1b presents a protein structure after spin labeling with the MTSSL. The site specific labeling of two sites in a protein is also applicable.

For a peptide with a designed sequence, mutagenesis of a native amino acid is not necessary. The amino acid cysteine can be incorporated during the peptide synthesis and then incubated with the MTSSL at room temperature before purification. Labeling of many proteins with this spin label has been shown to result in minimal structural perturbation and, more importantly, little functional perturbation.[13]

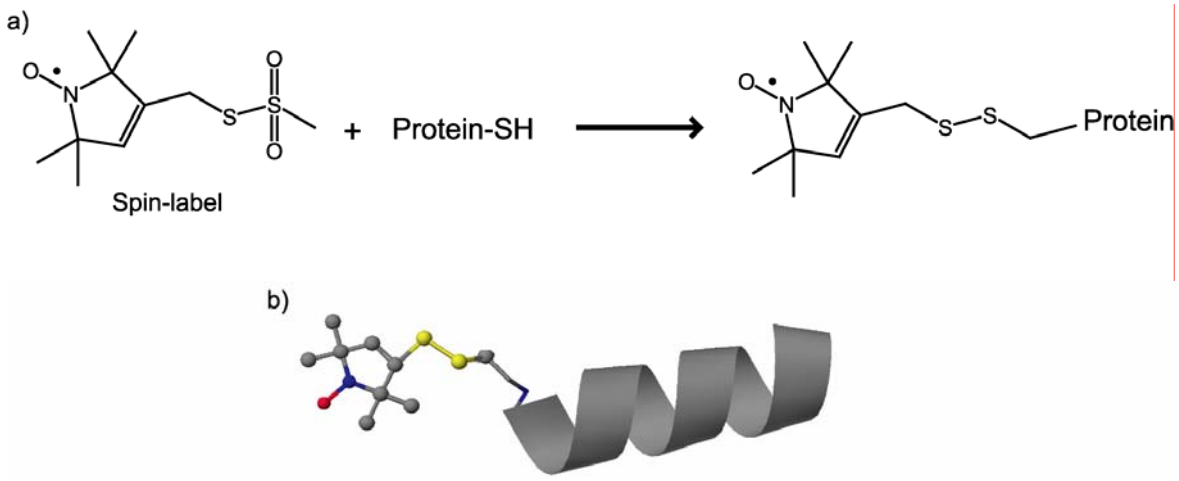

Figure 1-1: a) Structure of spin label and its reaction with the cysteine side chain; b) Structure of a helix peptide showing the sidechain of the spin label attached at the end.

1.2 DYNAMICS MEASUREMENTS FROM ESR

The key information obtained from an ESR spectrum results from the interaction of the electron spin with its surrounding environment; *i.e.,* with nearby nuclear spins, with the external magnetic field, and with each other. This section introduces the spin Hamiltonian, discusses how nitroxide interacts with its nearby surroundings, and how the spectrum depends on the orientation of the nitroxide-labeled macromolecule.

- *Spin Hamiltonian of Nitroxide*

ESR occurs when the microwave radiation is absorbed or emitted by paramagnetic molecules with at least one electron spin in the presence of a static magnetic field. For a nitroxide spin label attached to a specific site of a protein, an ESR spectrum can be interpreted by considering the spin Hamiltonian. The spin Hamiltonian of a nitroxide in a magnetic field is written as:

$$\hat{H} = \hat{H}_{EZ} + \hat{H}_{EN} + \hat{H}_{HFS} \tag{1-1}$$

where $\hat{H}_{EZ} = \beta_e \vec{B}_0 \cdot \overline{\overline{g}} \cdot \hat{S}$

$$\hat{H}_{EN} = -\beta_N \vec{B}_0 \cdot \overline{\overline{g}}_N \cdot \hat{I}$$

$$\hat{H}_{HFS} = \hat{I} \cdot \overline{\overline{A}} \cdot \hat{S} = \hat{H}_F + \hat{H}_{DD}$$

The term $\overline{\overline{g}}$ is the g-tensor, β_e is the Bohr magneton, β_N is the nuclear magneton, $\vec{B}_0$ is the vector of applied magnetic field, $\hat{S}$ and $\hat{I}$ represent electron and nuclear spin angular momentum operators, respectively, and $\overline{\overline{A}}$ is an anisotropic hyperfine tensor. The first and second terms are the *electron and nuclear Zeeman interaction*, respectively. These terms describe the interaction

of the electron and nuclear spins, respectively, with an external magnetic field. The first term, the electron Zeeman term, often yields information about excited electronic states and about the symmetry of the environment of the electron spin. The second term can be negligible due to the much smaller gyromagnetic ratio of the nitrogen (^{14}N) nuclear spin compared to that of the electron spin (~6500 times). The last term, the *hyperfine interaction*, represents the interaction of the electron spin with the magnetic moments of ^{14}N nuclear spin. The hyperfine interaction consists of two parts; the isotropic coupling called Fermi contact term ($\hat{H}_F$), and the anisotropic dipolar coupling ($\hat{H}_{DD}$).

- *Sensitivity of ESR to molecular orientation*

The ESR signal is extremely sensitive to the local environment. As the spin label mobility increases, the EPR linewidth narrows.[14-16] On the other hand, when the spin label mobility decreases; e.g., at low temperature or when it is attached to a restricted site of the protein, the EPR linewidth broadens and the spectral width increases.

Equation (1-1) shows that the g and hyperfine tensor are responsible for the orientational dependence of an ESR spectrum. In fact, the ESR lineshape of a nitroxide radical is very sensitive to the rotational diffusion of the spin-labeled molecule. To investigate an ESR spectrum based on the lineshape, and to then relate it to the rotational correlation time, we introduce a system of coordinates for the N-O paramagnetic moiety. Figure 1-2b shows the molecular coordinate system (x_m, y_m, z_m) of a nitroxide. This system is a common one for describing interactions of the nitroxide radical.[17] The z_m-axis is along the $2p_z$ orbital of the nitrogen, the x_m-axis is parallel to the N-O bond, and the y_m-axis is orthogonal to x_m and z_m following the right-handed rule.

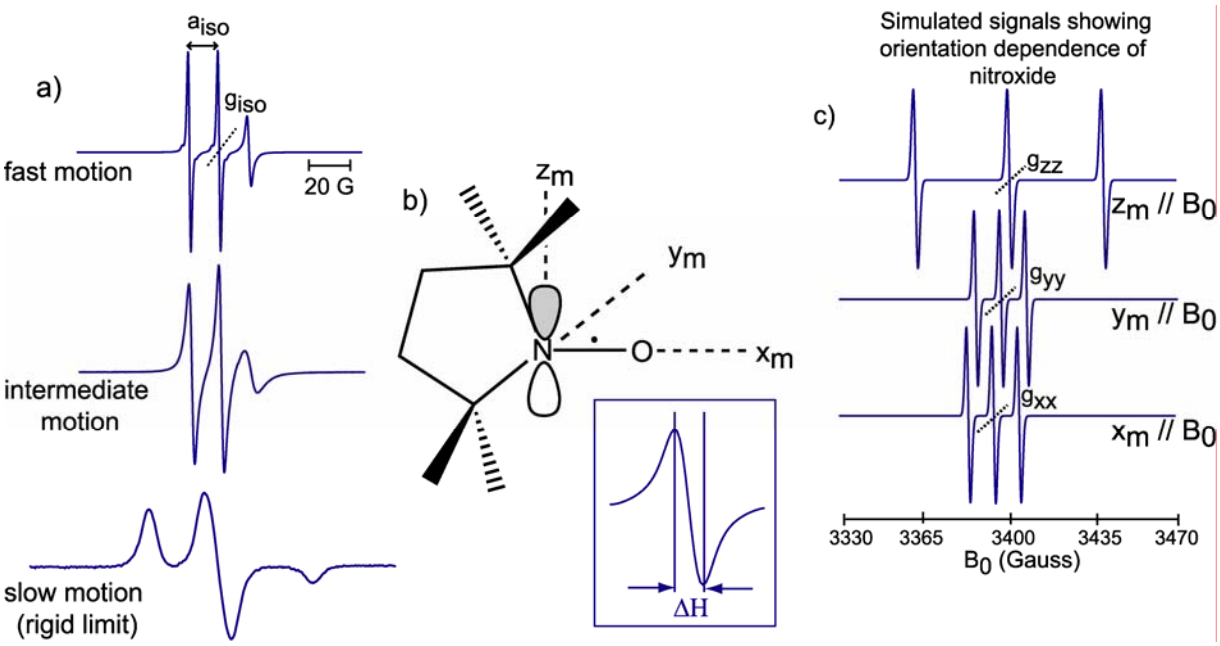

Figure 1-2: a) Continuous wave ESR spectrum in three motional ranges; the motionally narrowed limit (fast motion, top), intermediate motion (middle), and slow motion (bottom); b) Chemical structure of MTSSL spin label showing the molecular coordinate (x_m, y_m, z_m); c) Three simulated cw spectra showing orientation dependence. The direction of the three principal axes align parallel to the external magnetic field; $z_m//B_0$ (top), $y_m//B_0$ (middle), and $x_m//B_0$ (bottom). For typical nitroxide, $g_{xx} \sim 2.009$, $g_{yy} \sim 2.006$,and $g_{zz} \sim 2.002$. The splitting is due to hyperfine splitting, $a_{xx} \sim a_{yy} \sim 6$ G, and $a_{zz} \sim 35$ G. The inset shows the peak-to-peak linewidth (ΔH) of a cw spectral peak.

For a nitroxide, the values of the principal axes of the g (g_{xx}, g_{yy}, g_{zz}) and hyperfine tensors (A_{xx}, A_{yy}, A_{zz}) are typically $g_{xx}\approx2.009$, $g_{yy}\approx2.006$, and $g_{zz}\approx2.002$; $A_{xx}\approx A_{yy}\approx6$ G, and $A_{zz}\approx32$G.[18] These values, which may differ to some extent from one compound to another, also depend on the polarity of the environment.[18-20]

In the specific case where a nitroxide spin label is rapidly tumbling in a non-viscous solvent (i.e., in the case of fast rotational reorientation with a rotational rate of around 10^9-10^{11} s^{-1}), the g and hyperfine components in Equation (1-1) are averaged out and can be simplified to Equation (1-2) in the high-field approximation.

$$\hat{H} = g_{iso}\beta_e B_0 \hat{S}_z + A_{iso}\hat{I}_z\hat{S}_z \qquad (1\text{-}2)$$

where g_{iso} and A_{iso} are reduced to isotropic g and hyperfine components, respectively. The g_{iso} can be written as an average of the g-tensor principal components, *i.e.*, g_{xx}, g_{yy}, and g_{zz}.

$$g_{iso} = \frac{1}{3}(g_{xx} + g_{yy} + g_{zz}) \qquad (1\text{-}3)$$

For the hyperfine interaction, only the isotropic (Fermi contact) term, A_{iso}, exists. The A_{iso} arises from the non-vanishing electron spin density at the nucleus. Only an electron in *s* orbital has a non-zero probability density at the nucleus. Hence, this mechanism occurs through direct contact between the electron spin and the nucleus at the *s* orbital, as explained by its name; *contact interaction*. The isotropic hyperfine term can be written as:

$$A_{iso} = \frac{2\mu_0}{3\hbar} g_e \beta_e g_N \beta_N \left|\psi_0(0)\right|^2 \qquad (1\text{-}4)$$

where μ_0 is the vacuum permeability, g_e, β_e, g_N and β_N are previously defined, and $\left|\psi_0(0)^2\right|$ is the electron spin density at the nucleus. Solving the Hamiltonian in Equation (1-2) yields the energy eigenvalues. The spin operators $\hat{S}_z$ and $\hat{I}_z$ are replaced by the magnetic quantum numbers $m_{z,S}$ ($m_{z,S}=\pm1/2$), and $m_{z,I}$ ($m_{z,I}=0, \pm1$).

$$E = g_{iso}\beta_e B_0 m_{z,S} + A_{iso} m_{z,S} m_{z,I} \quad (1\text{-}5)$$

The resonance condition for the irradiated microwave becomes:

$$\Delta E = g_{iso}\beta_e B_0 + a_{iso} m_{z,I} \quad (1\text{-}6)$$

For a nitroxide radical, $\hat{S}_z$ = ½ and $\hat{I}_z$ = 1 for ^{14}N. Figure 1-3 presents the energy level diagram for the ESR transition of a nitroxide radical obtained from Equation (1-6). In the absence of magnetic field, B_0, the electron spin energy levels are degenerate. Within the applied magnetic field, the energy level of the electron is split into +1/2 (parallel) and -1/2 (antiparallel) spin states. The frequency of the transition between +1/2 and -1/2 energy levels is in the order of ~9.5 GHz for B_0 ~3400 G (X-band). Each electron spin energy level is further split into (2I + 1) sublevels due to the *hyperfine interaction*, which is on the order of MHz. The three distinct transitions are dictated from the selection rules; $\Delta m_{z,S}=\pm 1$, and $\Delta m_{z,I}=\pm 0$; *i.e.*, the electronic spin "flips" but the nuclear spin remains unchanged. The three allowed transitions lead to the three-line spectrum characteristic of nitroxides (Figure 1-2a, top panel).

The extreme opposite case to the isotropic condition is a rigid limit condition. In this situation, the rotational motion of the molecule does not exceed the lower limit of the ESR timescale (*c.a.* $<10^{-6}$ s for cw ESR at X-band only). The g and hyperfine terms become anisotropic. The ESR spectrum, which can be derived from Equation (1-1), generally, is composed of a superposition of spectra from every orientation of the molecular coordinates of nitroxide with respect to the external magnetic field. Figure 1-2c demonstrates the orientational dependence of the nitroxide spectra for the three principal orientations. If the three principal components of nitroxide spectra could be acquired, the spectra similar to that shown in Figure 1-2c would be obtained. From the bottom to the top of this panel, the molecular axes of x_m, y_m and z_m are parallel to B_0, respectively.

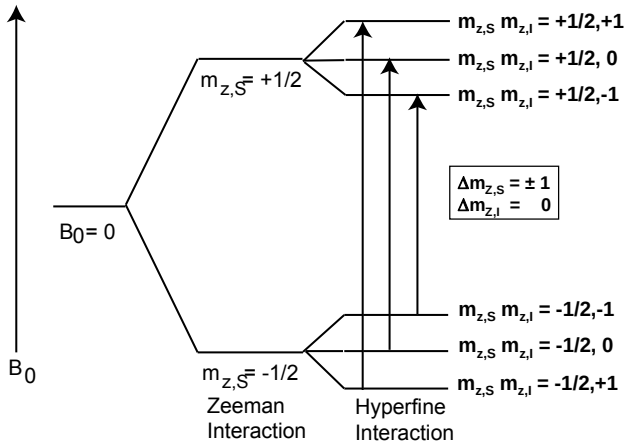

Figure 1-3: Energy diagram showing the three transitions of nitroxide. Symbols $m_{z,S}$ and $m_{z,I}$ denote electron and nuclear angular momentum quantum numbers, respectively. The transitions occur such that $\Delta m_{z,S} = \pm 1$, and $\Delta m_{z,I} = 0$.

The position of the spectrum slightly shifts to a lower magnetic field due to the minor changes in the g-values ($g_{xx} > g_{yy} > g_{zz}$). The splitting of the spectrum is due to the hyperfine interaction, which varies from one orientation to another. In this case, $A_{zz} > A_{xx} \approx A_{yy}$. The superposition of the spectra from every orientation yields the powder-like spectrum shown in Figure 1-2a (bottom panel).

For the intermediate timescale, the ESR spectrum consists of partially anisotropic contributions. The linewidth of the three hyperfine peaks is broader, and the overall spectrum extends to a wider range of magnetic field compared to that of the isotropic case (Figure 1-2a, middle panel). Therefore, the analysis of the ESR lineshape in this timescale provides information about the reorientation behavior of the spin labeled molecules.

- *Use of dynamics to infer structure of proteins*

The ESR lineshape reflects the motion of the nitroxide. As we have seen, the ESR spectra of nitroxide are isotropic when the rotational motion of nitroxide is so fast that the g- and hyperfine tensors are averaged out. However, the spectra are static in the rigid limit condition. In between these two limits, changes in the spectrum in response to changes in temperature, *etc.*, can be used to study the reorientational motion of the labeled molecules. The ESR linewidth is broadened when the mobility of nitroxide is slower, and *vice versa*. The linewidth produced by the reorientation motion of the nitroxide is *homogeneous broadening*. An ensemble of spin systems, when all spins experience the same local magnetic field and have the same spin-hamiltonian parameters, is called a 'spin packet'.[21] The ESR spectrum of a spin packet consists of a *homogeneous* linewidth. A single homogeneous linewidth, characterized by the decay time T_m, has a Lorentzian lineshape.

The sensitivity of the cw-ESR spectra to the mobility of a nitroxide side chain in a protein has been widely used to reveal the secondary structures and conformational changes of proteins. The relationship between side-chain mobility and protein structure has also been explored,[22] for example, in T4 lysozyme. Here, the single native side chains were sequentially replaced with a nitroxide side chain. In a sequence of regular secondary structures, the inverse linewidth (ΔH_0^{-1}) was found to be a periodic function of sequence number ("nitroxide scanning"). The periodicity is altered in different types of secondary structures; *e.g.*, the periodicity is 3.6 for α-helix, and 2 for β-sheet. Figure 1-4[23] shows the periodicity of the inverse linewidth *vs.* the sequence of T4 lysozyme (α-helix) and of cellular retinol-binding protein CRBP (β-sheet) in the nitroxide labeled region. Also shown in Figure 1-4 is another parameter, solvent accessibility (Π),[24] showing the periodicity as a function of sequence number. The nitroxide scanning method for detecting sequence-specific secondary structure has been applied to a number of membrane proteins.[25-27]

Recently, this method has also been used for monitoring the folding of a disordered protein,[28] and for determining the structural heterogeneity of a lipoprotein.[29] The sensitivity of nitroxide mobility to tertiary interactions has been applied to detect conformational changes of proteins in rhodopsin, T4 lysozyme, and cytochrome c.[22, 30, 31] Hubbell, *et al*[22] have systematically verified the relationship between the inverse lineshape and the inverse second moment, $\langle H^2 \rangle^{-1}$, for T4 lysozyme. Figure 1-5 presents this relationship for hindered, tertiary contact, helix surface, and loop sites. The linewidth is broader in the hindered (*i.e.,* motionally restricted site); on the other hand, it is narrower in the loop site where the nitroxide mobility is not confined.

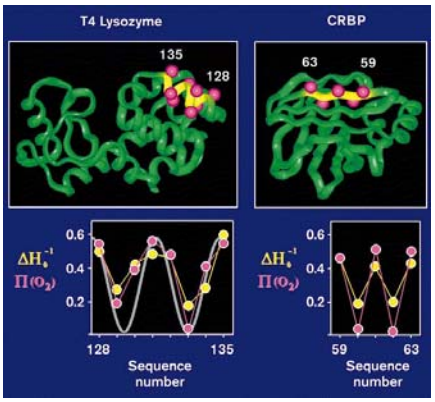

Figure 1-4: Determination of secondary structure by 'nitroxide scanning'. The upper panel shows the structures of T4 lysozyme and CRBP with sites of single nitroxide substitutions. The lower panel shows the periodicity of ΔH_0^{-1} and solvent accessibility as a function of sequence position (this figure was taken from Reference 23).

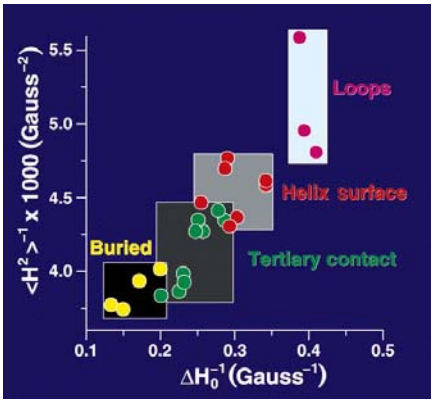

Figure 1-5: A plot of the inverse spectral second moments, $\langle H^2 \rangle^{-1}$, and the inverse central linewidths for the nitroxide side chain at twenty sites in T4 lysozyme (this figure was taken from Reference 23).

- *Measurement of rotational rate by cw-ESR*

Generally, a cw spectral linewidth, which contains both *homogeneous* and *inhomogeneous* broadening, is characterized by the decay time T_m^*. In the motionally narrowed limit (fast motion regime), the spectral anisotropies are averaged and the linewidth is determined by the modulation of anisotropic Zeeman and hyperfine interactions due to molecular motion.[32] The cw linewidth approximately represents the decay time T_m ($T_m \approx T_m^*$).

The peak-to-peak linewidth (ΔH) is related to the full width at half maximum (FWHM) of the absorption linewidth.[21, 33] The reorientation dependent contribution to linewidth has the following form:

$$\Delta H = \frac{1}{\gamma_e T_m} = \frac{FWHM}{\sqrt{3}} \qquad (1\text{-}7)$$

where FWHM is the full width at half maximum of the Lorentzian absorption lineshape. The parameter, T_m, is the *phase memory time*, and $\gamma_e = g_e\beta_e/\hbar$.

To obtain detailed information regarding the motional rate and anisotropy of the ESR spectrum, theoretical simulations are required. First, the rotational correlation time, τ_R, is obtained. In general, the rotational diffusion of spin-labeled molecules can be characterized by correlation time (τ_R), based on the ESR lineshape, in three motional regimes; 1) motionally narrowed (isotropic) limit, $\tau_R < 10^{-9}$ s, 2) intermediate regime, $10^{-9} < \tau_R < 10^{-6}$ s, and 3) rigid limit ($\tau_R > 10^{-6}$ s).

In the fast motion regime, τ_R can be estimated using Redfield theory. The relaxation rate, T_m, is given by[21, 33, 34]

$$\frac{1}{T_m} = (\frac{g\beta_e}{\hbar})^2 \overline{B_Z} \tau_R \qquad (1\text{-}8)$$

where $\overline{B_Z}$ is the mean square amplitude of the fluctuating fields along the z-axis. The linewidth ($1/T_m$) broadens with an increasing τ_R. Due to the limitation of the Redfield theory at short τ_R, this behavior cannot be extrapolated towards very long τ_R.[35, 36]

For the near rigid limit (slow motion regime), the ESR spectra are complicated both by the motions and the magnetic spin interactions. The cw linewidth can no longer be described by a simple Lorentzian line because the inhomogeneous contribution dominates the cw linewidth. The analysis requires a comprehensive treatment of relaxation theory. Freed, *et al*[17, 37, 38] have extended the calculation to cover the whole range of molecular motion, including the slow molecular tumbling using the stochastic Liouville equation.

The measurement of the phase memory time in the slow motion regime requires a pulsed technique that separates the homogeneous from inhomogeneous linewidth. The two-dimensional Fourier Transform (2D-FT) ESR provides such a measurement. The following section presents the principle of the pulsed ESR techniques of 2D-FT ESR.

- *Measurement of rotational rate by two-dimensional electron spin resonance (2D-FT ESR)*

The 2D-FT ESR experiments applied in this study are COSY (correlation spectroscopy), and SECSY (spin-echo correlated spectroscopy). Figure 1-6 presents the two-pulse sequences used in these experiments. The first $\pi/2$ pulse creates a transverse magnetization (*i.e.,* $\pm$ 1 coherences) which evolves for a period of t_1. During t_2, the signal is measured. After the first array of signal collection in t_2, the signal is repeatedly detected with an increment in t_1. The difference between these two experiments is the time delay of signal acquisition in t_2. After the second pulse, the signal is collected immediately following the dead time (FID format) for COSY, whereas it is delayed at time t_1 (echo format) for the SECSY experiment.

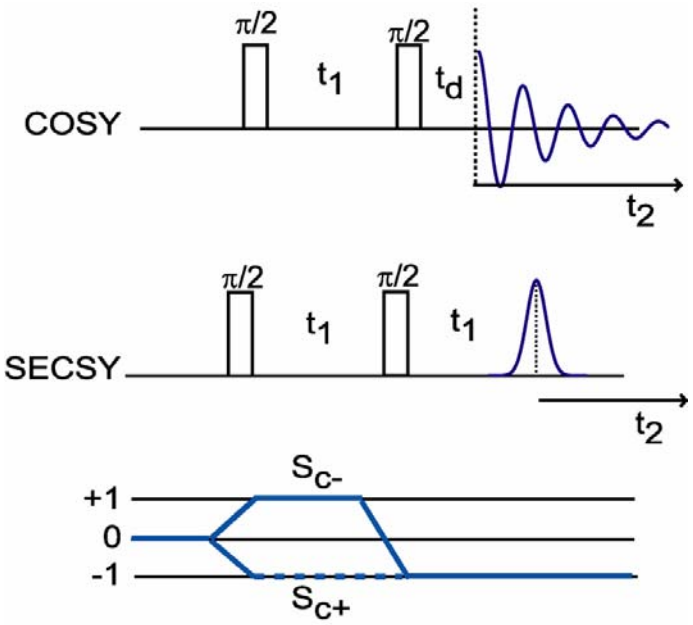

Figure 1-6: Pulse sequence for COSY and SECSY, and coherence pathway diagram. The solid and dashed lines in the coherence pathway diagram represent S_{c-} and S_{c+} signals, respectively. The S_{c-} signal is the corresponding coherence pathway to form the echo.

The SECSY experiment has the advantage of spin-echo spectroscopy by providing homogeneous linewidths across the inhomogeneously broadened dimension of the ESR spectrum.[39-42]

The quantitative analysis of motional effects can be incorporated into the signal by using the stochastic Liouville equation (SLE). The details of the analysis are provided elsewhere.[17, 40, 43] In general, the signal is detected using a dual-quadrature detector that provides two types of coherence signals, S_{c-} (echo-like) and S_{c+} (FID-like),[39, 40] see Figure 1-6.

For the COSY experiment, the $S_{c\pm}$ signal (corresponding to the 0 → ∓1 → -1 coherence pathways) excluding inhomogeneous broadening, are given by

$$S_{c\pm}(t_1,t_2)=\sum_{jn}K_{jn}\exp[-(\Lambda_{\mp 1})_j t_1]\times\exp[-(\Lambda_{-1})_n t_2] \qquad (1\text{-}9)$$

$$\text{where } (\Lambda_{\pm 1})_i=\frac{1}{T_{m,i}}\pm i\omega_i \qquad (1\text{-}10)$$

Here, K_{jn} is the amplitude, ω_i is the oscillation frequency, and $T_{m,i}$ is the relaxation decay for each component *i*. For fast motions, the eigenvectors are real, and the relation $(\Lambda_{-1})_i=(\Lambda^*_{+1})_i$ is valid. By replacing Equation (1-9) with Equation (1-10), and making *n=j*, the Fourier transform of the S_{c-} signal of nitroxide shows main three peaks at $f_1 = -f_2$, and at $f_1=f_2$ for S_{c+}. The peaks are labeled 1, 2, and 3 in Figure 1-7.

Even though the S_{c-} COSY looks like an FID signal, it is the same signal that would generate an echo at $t_1=t_2$; *i.e.*, the S_{c-} COSY can be transformed into a SECSY-like format to generate the homogeneous linewidth along the t_1 dimension. From Equation (1-9), replacing t2 → t1+t2, the Sc- signal becomes the SECSY signal:

$$S_{c-}^{SECSY}(t_1,t_2)\propto\sum_{nj}\exp[-(\Lambda_{+1})_n+(\Lambda^*_{+1})_j]t_1\times\exp(-\Lambda^*_{+1})_j t_2 \qquad (1\text{-}11)$$

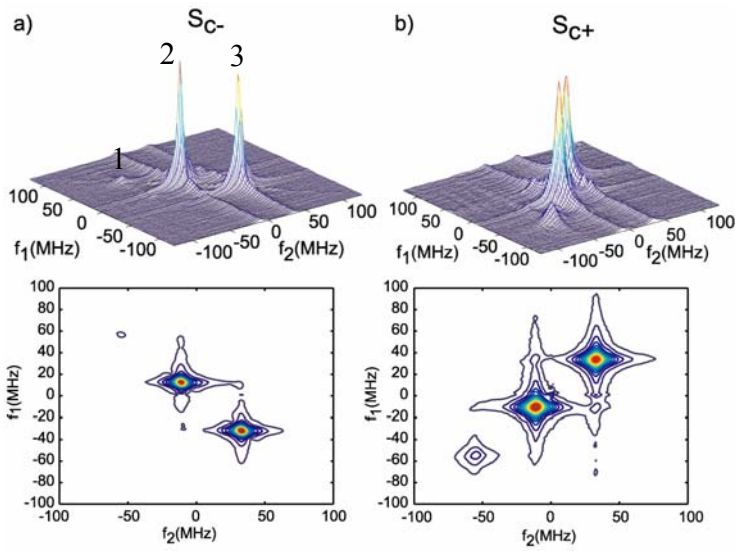

Figure 1-7: COSY spectra showing S_{c-} (a) and S_{c+} (b) signals in stacked and contour plots. The three hyperfine peaks of nitroxide occur at $f_1=-f_2$ for S_{c-}, and $f_1=f_2$ for S_{c+}.

The peaks that appear at $n=j$ can be written as:

$$S_{c-}^{SECSY}(t_1,t_2) \propto \sum_{jj} \exp[-2\,\mathrm{Re}(\Lambda_{+1})_j]t_1 \times \exp(-\Lambda_{+1}^{*})_j t_2 \qquad (1\text{-}12)$$

The SECSY spectrum shows the following: a) the homogeneous linewidth, which appears along the f_1 direction, is recovered due to the cancellation of the imaginary part; b) the cw-equivalent spectrum appears along the f_2, which contains the inhomogeneous linewidth. In practice, the SECSY data can be obtained by performing a shearing transformation on the data from the COSY experiment. Figure 1-8 shows the signal and the spectrum before (COSY) and after (SECSY) the shearing transformation.

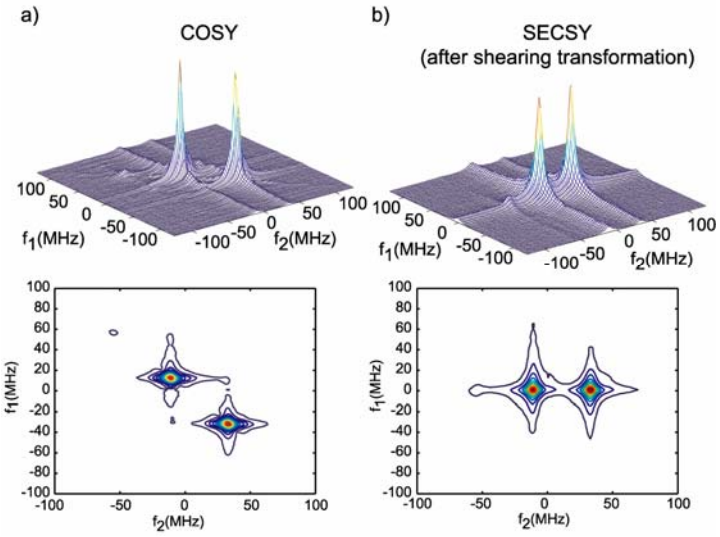

Figure 1-8: a) COSY spectrum in stacked and contour plots of Sc- signal; b) COSY spectrum after shearing transformation (equivalent to SECSY) in stacked and contour plots.

1.3 DISTANCE MEASUREMENTS BY ESR

- *Dipole-dipole coupling between two interacting electron spins*

In a system composed of two interacting nitroxides, in addition to the individual spin Hamiltonian, the magnetic electron-electron dipole-dipole and exchange interactions also become important. The Hamiltonian of two interacting electron spins is given by

$$\hat{H} = \hat{H}_1 + \hat{H}_2 + \hat{H}_{12}$$

where $\hat{H}_i = \hat{H}_{EZ,i} + \hat{H}_{EN,i} + \hat{H}_{HFS,i}$, $i = 1, 2$

$$\hat{H}_{12} = \hat{S}_1 \cdot \overline{\overline{D}} \cdot \hat{S}_2 - J\hat{S}_1 \cdot \hat{S}_2 \qquad (1\text{-}13)$$

Here $\overline{\overline{D}}$ is the electron dipolar coupling tensor and J is the magnitude of the electron exchange interaction (J-coupling). The indices 1 and 2 denote the electron spins of the first and second nitroxides, respectively. The Hamiltonian, H_i, is discussed in Section 1.2. For distances less than ~12 Å, the strength of the J-coupling, the measurement of the overlap between two electron orbitals, is important. This J-coupling results from two mechanisms of interaction; through-bond and through-space interactions. If there are a large number of single carbon-carbon bonds between the two nitroxides, then the through-bond interaction is negligible. The through-space coupling is sensitive to the interspin distance. Fiori & Millhauser[44] have modeled a through-space interaction as a decreasingly exponential function of interspin distance.

For distances longer than 12 Å, the exchange interaction can be neglected,[45] leading only the dipolar interaction to be considered. This is (in SI units)

$$\hat{H}_{12} = \hat{S}_1 \cdot \overline{\overline{\mathrm{D}}} \cdot \hat{S}_2 = \mathrm{c} \cdot \frac{1}{\mathrm{r}_{12}^3} \left[\hat{S}_1 \cdot \hat{S}_2 - \frac{3}{r_{12}^2}(\hat{S}_1 \cdot \vec{r}_{12})(\hat{S}_2 \cdot \vec{r}_{12})\right] \qquad (1\text{-}14)$$

where c is a constant having the value

$$c = \frac{\mu_0}{4\pi\hbar} g_1 g_2 \beta_e^2 \qquad (1\text{-}15)$$

The parameter r_{12} represents the distance between the two electrons, μ_0 is the permittivity of vacuum, and β_e is the Bohr magneton. For spin ½ and in the high field approximation, the Hamiltonian $\hat{H}_{12}$ can be written as[46]

$$\hat{H}_{12} = \omega_{12} \hat{S}_{z1} \hat{S}_{z2} \qquad (1\text{-}16)$$

where

$$\omega_{12} = c \cdot \frac{1}{r_{12}^3} (3\cos^2 \theta - 1) \qquad (1\text{-}17)$$

ω_{12} is the angular frequency due to the dipolar interaction. The $\hat{S}_{z1}$ and $\hat{S}_{z2}$ are the angular momentum spin operators along a magnetic field (B_0), c is the constant given by Equation (1-15), and θ is the angle between the magnetic field and the interspin vector as shown in Figure 1-9.

- *ESR Techniques for distance measurements*

For double spin-labeled molecules, the distance between two nearby spins can be quantified. The range of distances obtained from conventional continuous wave spectra is between ~5 and 20 Å. However, it was not until the 1980s[47] that pulsed ESR underwent rapid development; a decade later, ESR techniques were developed for the determination of long-range distances (~15 – 80 Å) between two sites in biological and synthetic macromolecules (see review articles in cited reference).[48]

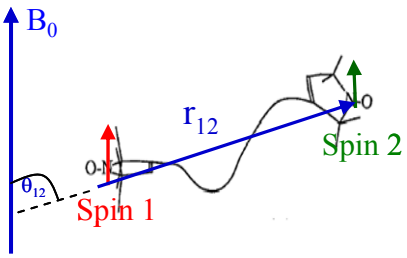

Figure 1-9: Diagram showing the orientation, θ, of a vector connecting the two interacting spins, r_{12}, with respect to the magnetic field.

The wide range of accessible distances makes ESR a useful technique for structural analysis of proteins and other macromolecules. In addition, ESR is a powerful tool for studying samples that other physical techniques find challenging. For example, even though X-ray crystallography has resolved a huge number of protein structures,[49] it is limited to crystallizable proteins and does not reveal protein structures in solution. In nuclear magnetic resonance (NMR),[50] the measurement of high molecular weight proteins, such as membrane protein complexes, is difficult, and a larger amount of sample is required. Furthermore, only short distance (up to 5 Å) information can be obtained. Fluorescence resonance energy transfer[51, 52] is another technique for determining the distance between two fluorescent sites, which are a donor and an acceptor. While, in principle, it is sensitive to large distances (*c.a.* 50 Å), the energy transfer depends on the relative orientations of the two chromophores. In a macromolecule, the relative orientations are poorly defined, leading to large uncertainties in the measured distances.

Distance measurements in ESR are based on the determination of the magnetic dipolar interaction between two electron spins. Most cw-ESR approaches rely on calibrating the broadening of the ESR lines due to the dipolar interaction. For small distances (*i.e.,* for $4 < r < 12$ Å), the dipolar interaction leads to a transition that occurs at half the normal resonant field. An empirically derived method, developed by Eaton and co-workers,[45, 53] exists for obtaining a distance from the intensity of this half-field transition ($\propto r^{-6}$ where r is the interspin distance). Shin, *et al*[54, 55] developed another cw approach, based on the comparison of the extent of broadening in singly and doubly labeled samples. The ratio of the Fourier transforms of doubly and singly labeled spectra gives a broadening function that is inversely proportional to the distance cubed between the labels. This method was shown to accurately reproduce known distances in the range between 8 and 20 Å for synthetic peptides.[56]

A drawback of these two methods is the necessity of freezing the samples since biological molecules mostly function at physiological conditions. However, ambient temperature measurement is available.[57] This procedure also requires a comparison of the line broadening between singly and doubly labeled samples. It is sensitive to the inverse interspin distance to the sixth power (instead of r^{-3}) and is, therefore, valid only for small proteins (<12 KDa).[58] The estimate distances between 8 and 20 Å were applied using T4 lysozyme as a model system. Later, using a pulsed technique, the measurement at room temperature was extended to a nitroxide-copper distance of an alanine-based peptide.[59]

Several pulsed methods have been developed in recent years to enhance the spectral resolution and to extend the distance range to between 15 and 80 Å.[48, 60] Two of these are double electron-electron resonance (DEER),[46, 61, 62] and the double quantum coherence (DQC).[63-66] These methods, which use the pulse sequence to project the dipolar interaction, do not rely on the spectral line-broadening. Although the experimental features of these two techniques differ, both techniques provide a signal modulation that directly relates to the electron-electron dipolar coupling, and scales as r^{-3}. Table 1-1 summarizes the ESR distance measurement techniques described above.

This thesis uses the DEER technique for the determination of the size and shape of synthetic nanostructures, *i.e., bis*-peptide polymers. The following section presents the fundamentals of the DEER technique.

Table 1-1: Comparison of ESR techniques for distance measurements as described in the text

ESR technique	Distance range (Å)	Dependence on r	Sample condition	Signal
cw (Half-field transition)	4-12	r^{-6}	Frozen	cw spectrum
cw (Fourier deconvolution)	8-20	r^{-3}	Frozen	comparison of line-broadening between single and double labeled samples
cw	8-20	r^{-6}	Room temperature	comparison of line-broadening between single and double labeled samples
pulse: Inversion recovery	17-25	r^{-6}	Room temperature	Comparison of T_1 relaxation of nitroxide in the presence and absence of copper
pulse: DEER	15-80	r^{-3}	Frozen	modulation in time domain
pulse: DQC	15-80	r^{-3}	Frozen	modulation in time domain

- **Distance measurement by double electron-electron resonance (DEER)**

Double electron-electron resonance (DEER),[67] also known as pulsed electron-electron double resonance (PELDOR),[68, 69] is a pulsed ESR technique applied for distance measurements between two interacting electron spins. The method directly separates the *weak* electron-electron coupling (a few MHz) from other interactions (*e.g.*, ~9.5 GHz for the Zeeman interaction at 3000 G). The dipolar Hamiltonian involving dipolar interaction described in Equation (1-16) can be directly applied. One limitation of this experiment, however, is that it must be performed at low temperatures (usually ≤ 80 K) so that the molecular motion is 'static'.

The experiment relies on using microwave pulses of two different frequencies. Each frequency excites the spins in different parts of the spectrum (see Figure 1-10c for a nitroxide absorption spectrum at low temperature), represented as 'spin 1' and 'spin 2'.[46] A soft pulse (*i.e.*, a pulse that excites only one transition of a spin packet) is used in order to separate the excitation bandwidths between the two frequencies.

The pulse scheme shown in Figure 1-10a detects the dipolar interaction between 'spin 1' and 'spin 2'. The 'spin 1' is excited by the main frequency, ω_1, called the *observing* or *probe* pulse. This pulse can be a two- or three- pulse sequence. For the three-pulse sequence, a primary echo is generated after the $\pi/2-\tau_1-\pi$ sequence, which is refocused at time τ_2 after the last π pulse. Another frequency, ω_2 (the *pump* pulse), irradiates 'spin 2' with a flip angle π at a varied delay time, T, starting from the position of the primary echo to the last observed π pulse. When the 'spin 2' is inverted by the pump π pulse, it induces a change of the local magnetic field at 'spin 1'. As the timing of the pump pulse varies, the amplitude of the refocused echo is modulated with a frequency related to the distance between the spins (ω_{12}). The modulation of the refocused echo is observed as a function of time T. The modulated signal in the time domain, V(T), is proportional to $\cos(\omega_{12}T)$ where ω_{12} is given by Equation (1-17).

For two spins at a fixed distance in a sample with a random orientation distribution, the analysis of the DEER signal is straightforward. The functional form, V(T), of the observed signal is an integral of all possible orientations (θ) between the interspin vector, $\overrightarrow{r_{12}}$ and B_0 as:

$$V(T) = \int_0^{\pi/2} \cos(\omega_{DD} \frac{(3\cos^2\theta - 1)}{r_{12}^3} T) \sin\theta d\theta \qquad (1\text{-}18)$$

$$\text{where } \omega_{\text{DD}} = \frac{\mu_0 \, g_1 \, g_2 \, \beta^2}{4\pi\hbar}$$

Figure 1-11 (left) shows the signal derived from Equation 1-18. The fast decay in the beginning of the signal is due to the superposition of the signals at each orientation. The spectrum after Fourier transform provides a *Pake pattern*[70] (Figure 1-11, right).

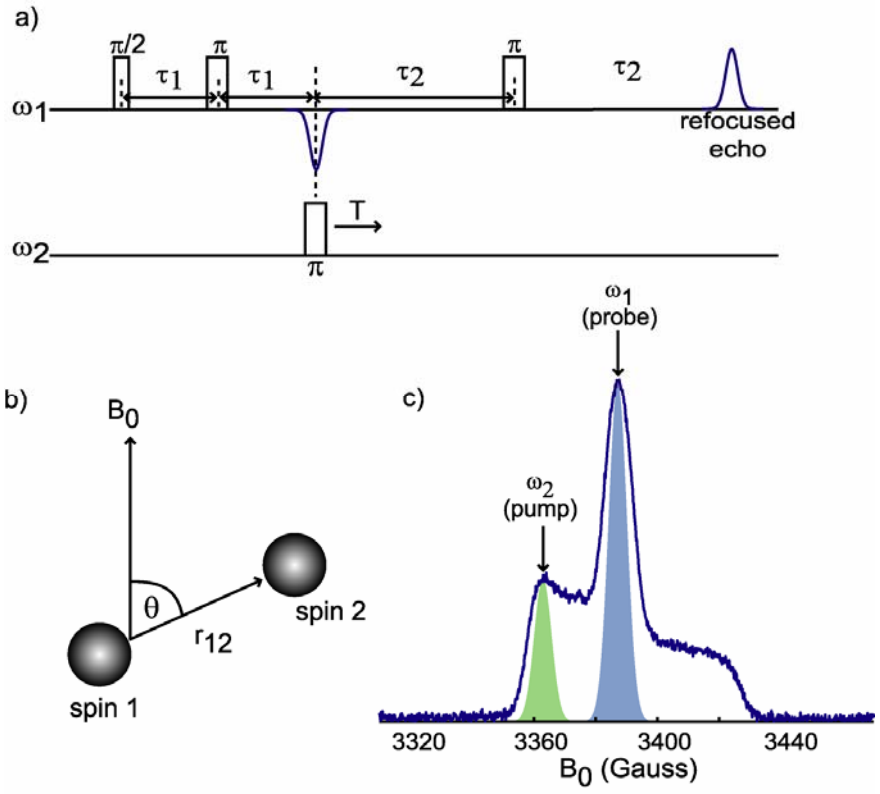

Figure 1-10: a) Pulse sequence applied in a DEER experiment; b) Orientation of the interspin vector with respect to the external magnetic field (B_0); c) Excitation profile of probe and pump frequencies.

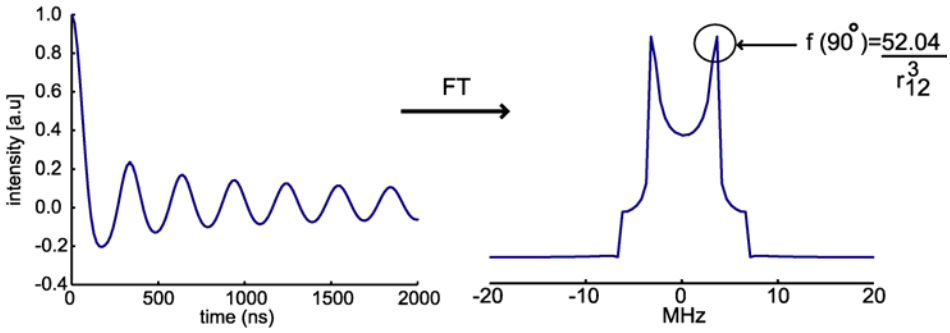

Figure 1-11: Modulation of DEER signal due to a dipolar interaction between two interacting spins; a) in the time domain, and b) after Fourier transform providing a symmetric spectrum. The maximum peak occurs at θ=90° and is related to inverse cube distance r_{12}.

The frequency appearing in the Pake pattern depends on the orientation angle, θ. The most distinct orientation is at the singularity θ=90° where sin(θ) is a maximum. By using Equation (1-18) and assuming that the g-values (g_1 and g_2) are 2.0, and θ = 90°, the frequency ω_{12} at 90° is related to the interspin distance, r_{12}, as

$$\frac{\omega_{12}(90^\circ)}{2\pi}\,\mathrm{MHz} = \frac{52.04}{r_{12}^{\ 3}\ (\mathrm{nm})} \tag{1-19}$$

For a sample with a short and narrow distance distribution, the distance obtained from Equation (1-19) is a good approximation.

More demanding calculations are required for samples with a broad distance distribution, which is mostly the case for flexible macromolecules. A simulation of the DEER signal is needed to acquire the full distance distribution, P(r).[71] Typically, time domain data are used for the analysis; they provide a more accurate analysis than the frequency spectrum because the singularity in the Pake pattern might not always be easily detected. The signal, V(T), can be expressed in the following form of the Fredholm equation of the first kind given by the kernel κ(r,T)[72]

$$V(T) = \int_{R\,\min}^{R\,\max} \kappa(r,T)P(r)dr \tag{1-20}$$

$$\text{where } \kappa(r,T) = \int_0^1 \cos[(1-3x^2)\omega_{DD}T]dx \text{, and } x = \cos\theta\,.$$

Here R_{min} and R_{max} are the range of possible distances for P(r). Inversion of this equation to obtain P(r) is known to be an ill-posed problem; *i.e.*, many functions of P(r) may yield a predicted V(t) that agrees with the experimental V(t) within the error bounds of the experiment.[72] Approximation of the kernel, κ(r,T), has been reported using an analytical expression; *e.g.*, shell factorization analysis.[73] In addition, a model free method to convert the time domain data into a

distance distribution has been implemented using the Tikhonov regularization method[74] by Chiang, *et al*[75] and Jeschke, *et al.*[76] The two cited references present the details of the procedure.

The Tikhonov regularization method, also applied for data analysis in Chapter 3, is briefly discussed here. Equation (1-20) is converted into a discrete form for M data points and N solution points:

$$V(T) = \int_{R\min}^{R\max} \kappa(r,t)P(r)dr \approx \sum_{j=1}^{N} w_j \kappa(T_i, r_j)P(r_j) \qquad (1\text{-}21)$$

where $w_j = (R_{\max} - R_{\min})/N$, $r_j = (j - 1/2)w_j + R_{\min}$ for $j = 1, 2, \ldots, N$, and $t_i = (i - 1/2)\,(T_{\max}/M)$ for $i = 1, 2, \ldots, M$. The discrete from is converted into a system of linear algebraic equations represented by

$$S = KP \qquad (1\text{-}22)$$

Elements of K are $k_{ij} = w_j \kappa(T_i, r_j)$, and S are $s_i = V(T_i)$; for i=1,2,…M, and j=1,2,…,N. Here, K denotes an operator that maps the function P onto the experimental data vector S. The Tikhonov regularization method modifies the equation to the following functional form, Φ[P]:

$$\Phi[P] = \left\|KP - S\right\|^2 + \lambda^2 \left\|LP\right\|^2 \qquad (1\text{-}23)$$

where λ is the so-called regularization parameter and L is an operator identity ($LP = P$ or $LP = P'$). The regularized solution P_λ is obtained by minimizing Equation (1-24):

$$P_\lambda = (K^T K + \lambda^2 L^T L)^{-1} K^T S \qquad (1\text{-}24)$$

The quality of the result depends strongly on the regularization parameter λ. If λ is too small, the result will show artificial peaks. If λ is too large, the result will be over-smoothed, providing a distance distribution that is too broadened. The cited references[72,76] provide the criteria for choosing the optimum λ using the L-curve method. Jeschke[77] has implemented a program

package for fitting DEER data (DEERAnalysis 2006) based on the Tikhonov regularization method, which can be freely downloaded.

2.0 NITROXIDE SPIN-RELAXATION OVER THE ENTIRE MOTIONAL RANGE

Part of this work, written in collaboration with Marco Bonora and Sunil Saxena, has been published in the Journal of Physical Chemistry B, 2004, V.108 (13), pages 4196-4198.

2.1 ABSTRACT

Homogeneous linewidths, characterized by the phase memory time, T_m, of a nitroxide spin-labeled peptide were measured over the entire motional range (~10^{-10} - 10^{-4} s at the spectrometer resonance frequency of 9.7 GHz) using spin echo correlated spectroscopy (SECSY) ESR. Phase memory times as short as 20 ns could be determined by using schemes designed to minimize the effects of pulse ring-down. Experimental T_m versus temperature curve (from 192 K to 310 K) clearly resolves the T_m minimum, which provides great sensitivity to the details of molecular dynamics.

2.2 INTRODUCTION

In recent years there has been a significant development of two-dimensional (2D) pulsed methods in electron spin resonance (ESR).[21, 39, 41, 78-80] These 2D Fourier transform (FT) ESR

methods provide improved sensitivity to reorientational dynamics[81-83] and large interspin distances (~15-70 Å).[46, 64-66, 84-88] However, experimental challenges have limited their usefulness when phase memory times, T_m, become small.

The ESR spectral extents from nitroxides can become as large as 200-250 MHz.[89] The pulse length for exciting the entire spectrum is given by

$$tp(ns) \leq \frac{1000}{\Delta f(MHz)} \qquad (2\text{-}1)$$

The shorter the pulse length, the wider the excitation bandwidth. To excite this large bandwidth, short high power (~kW) pulses are required. The ESR signal, on the other hand, is weak (~ nW) and decays rapidly (in 10-100's of ns). The power of the intense pulse cannot dissipate immediately after the pulse and, thus, generates a ring-down before decaying. The initial, intense part of the time decaying ESR signal is swamped by the ring-down of the pulse, creating a *dead time*. Therefore FT-ESR signals can only be obtained when the phase memory time of the sample is long. For nitroxides, T_m decreases with temperature in the fast motional regime ($T_m \propto \tau_R^{-1}$, where τ_R is the rotational correlation time), goes through a minimum, and then increases as temperature decreases in the slow motional regime ($T_m \propto \tau_R^{\alpha}$, $1 \leq \alpha \leq 0.5$).[90, 91] Resolving dynamics using FT-ESR when temperature is close to the T_m minimum has been very difficult. In this work, we apply a scheme to reduce the spectrometer dead-time and successfully determine the T_m minimum for a rigid nitroxide labeled proline peptide.

The lineshape of the nitroxide ESR spectrum reports on the local environment of a protein at the labeling site.[11] Different line-shapes of ESR spectra have been investigated for nitroxides attached on different sites of protein structures and interactions, such as loops, helix surfaces, tertiary interactions, and buried sites.[22, 23] In complex systems, such as membrane

proteins where the motion of the attached nitroxide sidechain is mostly restricted, the ESR line-shape is usually broad and anisotropic. This motional range usually falls near the minimum in the phase memory time, or into the slow motional regime. The feasibility of resolving the T_m minimum opens up the possibility of using 2D ESR for the study of spin-labeled membrane proteins.

2.3 EXPERIMENTAL

- *Sample Preparation*

A doubly spin-labeled peptide CPPPPC (C=cysteine and P=proline) was synthesized at the peptide facility of the University of Pittsburgh and was spin-labeled on the cysteines with methanethiosulphonate (MTSSL) purchased from Toronto Research Chemicals Inc. A 5×10^{-4} M solution of the labeled peptide in 70% glycerol, 15% 2,2,2-trifluoroethanol and 15% water buffered (pH 7.2) with MOPS [3-(N-Morpholino) Propane-Sulfonic Acid] was prepared. The sample was degassed using several freeze-pump-thaw cycles to a final pressure of 4×10^{-5} Torr and then flame-sealed.

- *ESR Spectroscopy*

ESR experiments were performed using a Bruker EleXsys E580 CW/FT X-band ESR spectrometer equipped with a Bruker ER 4118X-MS3 X-band split ring resonator. The cw ESR spectra were recorded with a quality factor, Q, of about 1000, a field-sweep of 200 G and a modulation amplitude of 1.0 G. The two-pulsed correlated spectroscopy (COSY-ESR) experiments were obtained with a resonator $Q \leq 100$ and an ASE TWTA with an output power

of 1 kW. The length of the π/2 pulse was 6 ns. The dead time in t_1 was 8 ns. Typically 32 to 128 points were collected in t_1 with a step size of 2 ns or 4 ns. In t_2, 256 points with a step size of 4 ns were collected. The repetition rate was 5-10 kHz and the number of averages ranged from 500 to 150,000. The COSY-ESR signal was obtained using the usual 8-step phase-cycle.[39, 41]

A short dead time in t_2 of 28-32 ns was achieved by a combination of two approaches that produced partial cancellation of ring-down artifacts. First, the phase cycle was divided into eight pairs. It was then implemented such that the signal from the second step, in each pair, subtracted from the first.[81] The phase cycle is provided in Appendix A. Second, when the signal became very weak (*i.e.*, near the T_m minimum) an off-resonance signal was subtracted from the on-resonance signal after each step of the phase cycle. This strategy allowed a reduction of dead time by as much as 20 ns (*i.e.*, from ~50 ns to ~30 ns).

- *Calculation of T_m*

The signals obtained from COSY experiments were converted to the SECSY signals by the 'shearing transformation'. Figure 2-1a shows a representative SECSY spectrum of the double-labeled poly-proline peptide 310 K. The lineshape along f_2 is similar to the absorption spectrum of cw ESR. Regarding the other dimension; *i.e.*, f_1, there is only a single peak centered at f_1 = 0 MHz. The line broadening along this f_1 dimension represents *homogeneous* linewidth, which is inversely proportional to the phase memory time, T_m. To determine T_m, a slice along f_1 at a given value of f_2 was extracted from the SECSY spectrum. In Figure 2-1a the lineshape along f_1 of the central peak is demonstrated by a solid black line. The line-shape was fit to a Lorentzian function as[92]

$$L(f_1) = c \cdot \frac{1}{\sqrt{\Delta f_1^2 + 4\pi^2 (f_1 - f_0)^2}} + b \qquad (2\text{-}2)$$

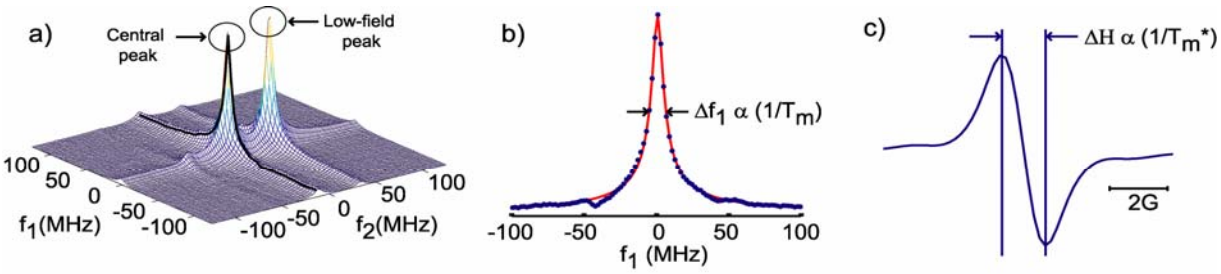

Figure 2-1: a) SECSY spectrum of bi-labeled poly-proline at 310 K. The lineshape along f_1 at the central peak is shown by the solid black line; b) The spectrum lineshape along f_1 (dotted line) is fit to a Lorentzian function (red line). T_m is inversely proportional to the linewidth, Δf_1; c) A cw spectrum of the same sample showing the peak-to-peak linewidth (ΔH). T_m^* is inversely proportional to ΔH.

where f_l is the frequency in s^{-1}, $L(f_l)$ is the intensity, f_0 is the frequency-offset, c is a normalization constant, Δf_l is the width at half height, and b is a baseline offset. The fitting along the f_l slice for the central peak at 310 K is demonstrated in Figure 2-1b.

The phase memory time is given by[21]:

$$T_m(\text{ns}) = \frac{2000}{\Delta f_l(\text{MHz})} \tag{2-3}$$

- *Calculation of T_m^**

A cw spectrum provides the linewidth containing the inhomogeneous contribution, which is characterized by T_m^*. T_m^* is calculated from the peak-to-peak linewidth, ΔH, as shown in Figure 2-1c. ΔH is related to T_m^* as [21, 33]

$$\Delta H = \frac{2}{\sqrt{3}\pi T_m^*} \tag{2-4}$$

The unit of ΔH in Equation 2-4 is in Gauss, and T_m^* is in Gauss^{-1}. To convert the unit of Gauss to a frequency unit, it must be multiplied by 2.8071 (1 Gauss ~ 2.8071 MHz for a g-value of 2.0056). Thus, the T_m^* can be calculated as

$$T_m^*(ns) = \frac{2000}{2.8071(\sqrt{3}\pi)\Delta H(MHz)} \tag{2-5}$$

- *Simulation models*

The dynamical parameter; *i.e.*, rotational correlation time (τ_R), can be quantified by simulating the SECSY spectra. Spectral simulations were performed using the 2D FT-ESR simulation package NL2DR[38, 40] modified to run on a LINUX based computer. A basis set (3% pruning tolerance) was calculated using a minimum truncation set[6,8] of L^e_{max}=32, L^0_{max}=17,

K_{max}=6, and M_{max}=2. The magnetic parameters used were g_{xx}=2.0086, g_{yy}=2.0064, g_{zz}=2.0032, A_{xx}=A_{yy}=6.23 G, and A_{zz}=35.7 G.

Theoretical SECSY spectra were calculated using two commonly used models for accounting for the motion of the peptide chain: 1) anisotropic Brownian diffusion[92] and 2) a Microscopic Order Macroscopic Disorder (MOMD)[93] model (see Figure 2-2).

1. Anisotropic Brownian diffusion

In this model the nitroxide is considered to be rigidly attached to the peptide. The peptide executes an anisotropic re-orientational motion given by rotational rates about the z-axis, $R_{||}$, and x,y-axes, R⊥ (i.e., axially symmetric). The ESR spectrum is treated in terms of two rotational correlation times, one that characterizes the motion about a principal molecular axis ($\tau_{R||}$), and one perpendicular to it ($\tau_{R\perp}$). The faster reorientation defines $\tau_{R||}$ providing the average τ_R as

$$\bar{\tau}_R = \sqrt[3]{\tau_{R\perp}^2 \tau_{R||}} \qquad (2\text{-}6)$$

The diffusion frame (x_d, y_d, z_d) is defined as $x_d = y_d \perp z_d$. The axis z_d is parallel to the $\tau_{R||}$.

2. Macroscopic Order but Microscopic Disorder

In this model, the long chain of the molecules is imagined to align along a specific direction called a director. The director tilt angle, ψ, is defined as the angle between the director axis and the magnetic field. The diffusion of the nitroxide is constrained by an ordering potential, U, which is expanded in a series of spherical harmonics as:

$$-U(\Omega)/K_B T = \sum_{L,K} \varepsilon_K^L D_{0K}^L(\Omega) \qquad (2\text{-}7)$$

where Ω represents the Euler angles (α,β,γ) relating the diffusion frame to the director frame. For the simulations performed in this work, only the first term with coefficient, ε_0^2, is considered.

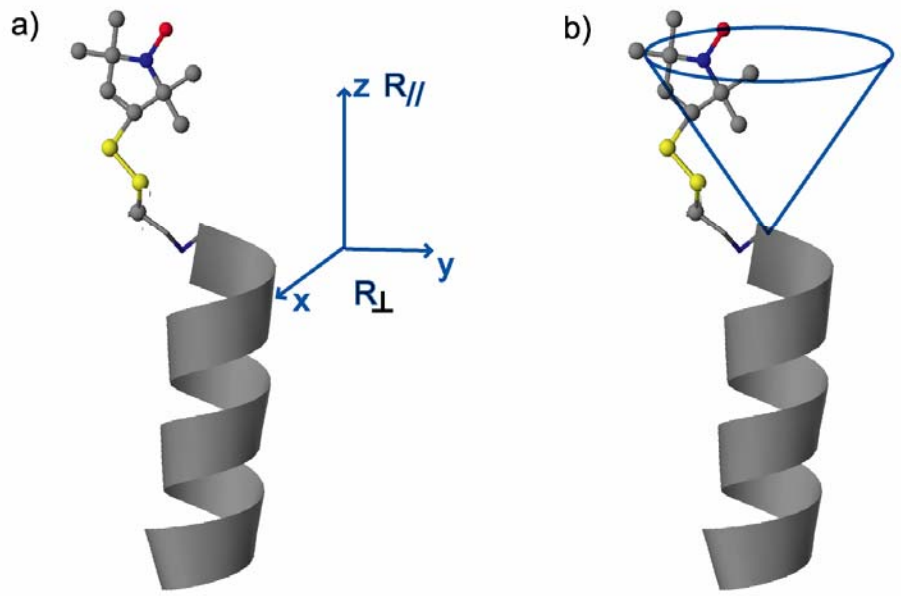

Figure 2-2: Models representing nitroxide reorientation on a rigid peptide chain used in the simulations. (a) anisotropic diffusion model, and (b) MOMD model.

Due to the ordering potential given by the main chain, the orientation axis of nitroxide is dispersed in various directions (macroscopic disorder), but within each orientation the axis is well aligned in a specific direction (microscopic order). The spectrum is then a superposition of the spectra from all orientations, which can be written as:

$$S_{c\pm}^{MOMD} = \int S_{c\pm}(\psi) \sin\psi d\psi \qquad (2\text{-}8)$$

where $S_{c\pm}(\psi)$ is the ESR spectrum with the director angle ψ. The effect of MOMD has been previously applied for the analysis of lipid bilayers[94] and liquid crystalline polymers.[95]

For a nitroxide attached to the proline peptide, the MOMD model accounts for the flexibility of the nitroxide linker. The nitroxide reorients in an orienting potential provided by the main chain, which restricts its amplitude of motion. The value used for ε_0^2 is kept at 1.0 for all correlation times, although it can be temperature dependent in general. The simulated spectra were summed over 10 orientations.

For each model axially symmetric rotational rates were used with the anisotropy factor $N = (R_{\|} / R_{\perp}) = 10$. The simulations were performed as a function of $\overline{R} = \sqrt[3]{R_{\|} R_{\perp}^2}$ and the average rotational correlation time, $\bar{\tau}_R$, was determined as $6\bar{\tau}_R = 1/\bar{R}$. A Gaussian inhomogeneous broadening of 1.0 G was used.

2.4 RESULTS AND DISCUSSION

- *Sensitivity of homogeneous linewidth to temperature change*

The 2D-FT ESR spectra of a bi-labeled poly-proline were thoroughly investigated in the temperature range from 192 to 310 K. A shearing transform[40] on the "echo-like" Sc-[40, 81-83, 92] of COSY signal converts these data into the spin echo correlated spectroscopy (SECSY) format. The linewidth of the 2D spectrum varies as the temperature changes indicating the sensitivity of the technique to the motion of the nitroxide. Figure 2-3 shows two representative 2D-SECSY and cw spectra in two regions of reorientational motion; fast motion (310 K to 280 K) and slow motion (247 to 192 K) regions. The lineshape along f_2 in the SECSY spectrum is equivalent to that obtained in absorption mode of cw ESR. Between the two extreme temperature limits (192 and 310 K), the shapes of the spectra along f_2 are very different. At 310 K, the spectrum shows discrete peaks and is characteristic of nitroxide reorienting *rapidly* (rotational rate from ~10^8 to 10^{10} s^{-1}) in solution. This motional reorientation is called a 'motional narrowing' case. On the other hand, at 192 K, the signal spreads out and shows a continuous line shape. This spectrum is characteristic of nitroxide reorienting *slowly* (rotational rate from ~10^4 to 10^8 s^{-1}) in solution. The linewidth along the f_2 dimension is broadened as the temperature is lowered. The line broadening along f_2 is influenced by both *homogeneous* and *inhomogeneous relaxation process*, and is characterized by T_m^*. The cw lineshape is used to calculate T_m^* as described in the Data Processing section. Both homogenous and inhomogeneous relaxation processes contribute to T_m^*; it can be, therefore, written as

$$\frac{1}{Tm^*} = \frac{1}{T_{\text{hom}\,ogeneous}} + \frac{1}{T_{in\,\text{hom}\,ogeneous}} \qquad (2\text{-}9)$$

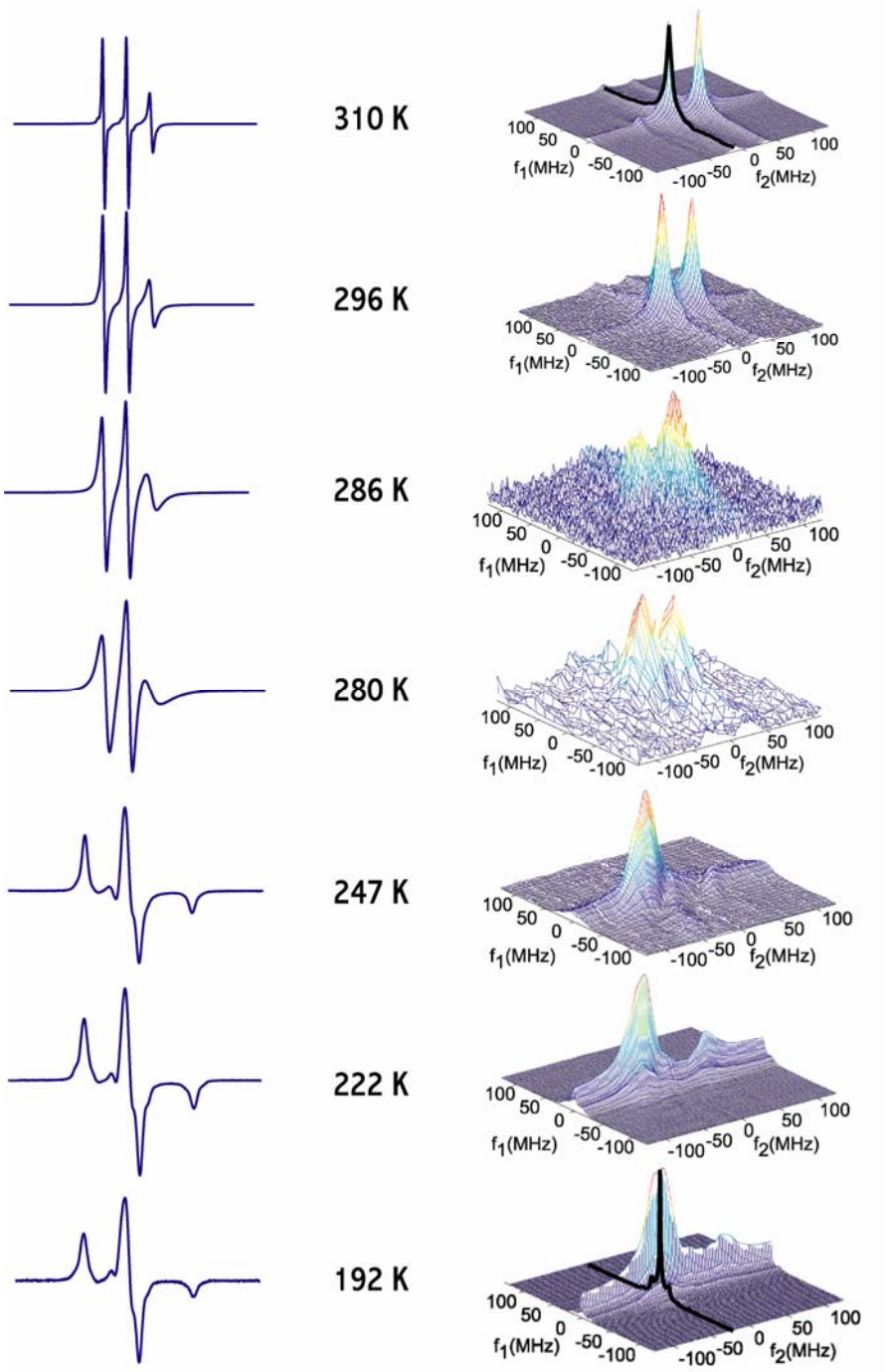

Figure 2-3: Representative cw and SECSY-ESR spectra of bi-labeled proline peptide at various temperature ranges; fast motion regime (from 310 to 280 K), slow motion regime (from 247 to 192 K), and near the T_m minimum (280 K). The line shape along the f_1 dimension for the central peak is shown (black solid lines) at 310 and 192K.

where $T_{homogeneous}$ and $T_{inhomogeneous}$ are the characteristic decay due to homogeneous and inhomogeneous processes, respectively. The time, $T_{homogeneous}$, is referred to as phase memory time (T_m). The ($1/T_m^*$) line broadening is temperature dependent in the fast motional regime, where the contribution of inhomogeneous broadening is negligible. On the other hand, in the case where nitroxide slowly reorients in solution, the contribution of inhomogeneous broadening dominates. Hence, the sensitivity of T_m^* to reorientational motion is lost, and the cw linewidth is insensitive to the motional rate.

Representative cw ESR and SECSY spectra in the slow motional regime are shown in Figure 2-4 at 222 K and 242 K. The cancellation of inhomogeneous broadening can be obtained from the other dimension; *i.e.*, the f_1 dimension. Along this dimension, there is only a single peak centered at $f_1 = 0$ MHz. The f_1 dimension provides the homogenous lineshape, characterized by the phase memory time T_m, leading to improved sensitivity to slow dynamics than possible with CW-ESR.[42] Despite the change in temperature by 20 K, the CW-ESR spectra are practically identical, indicating weak sensitivity to dynamics in this very slow motional regime. On the other hand, the f_1 dimension in the SECSY spectra shows clear changes - the linewidth changes by a factor of four (*cf.* Figure 2-4c versus 2-4d). Figure 2-5 compares the homogeneous linewidth, T_m, to the T_m^* to emphasize the sensitivity of SECSY-ESR to the change of temperature in the slow motional regime. In the temperature range between 250 and 310 K, the temperature dependence of T_m^* is comparable to that of T_m. Large inhomogeneities mask the spectral effects of motion and the cw linewidth, T_m^*, shows only a weak dependence on temperature. As the temperature further decreases, however, T_m^* is independent of temperature whereas T_m is increasing.

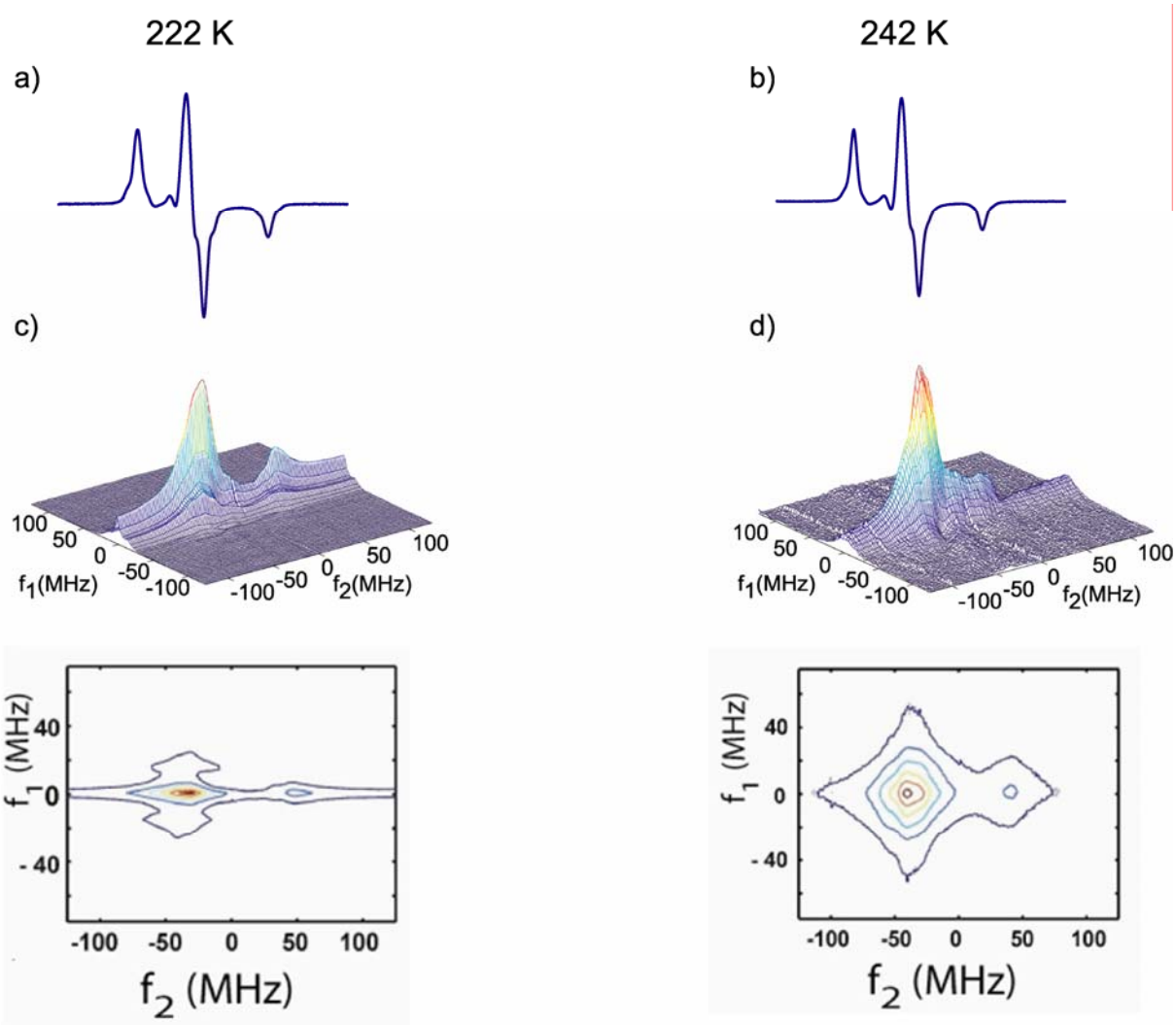

Figure 2-4: CW ESR spectra for the nitroxide spin-labeled poly-proline peptide are shown at temperatures of (a) 222 K, and (b) 242 K. SECSY-ESR spectra at 222 K and 242 K are shown in (c) and (d), respectively, in stack and contour formats. The change in slow reorientational motion due to change in temperature cannot be resolved in cw-ESR (*cf.* Figure 2-4a *vs.* 2-4b), whereas it leads to dramatic changes in homogeneous lineshapes (*i.e.*, the spectrum along f_1) in the SECSY-ESR spectra.

The temperature dependence of T_m can be described as the following; starting from the fast motional regime, T_m decreases with temperature ($T_m \propto \tau_R^{-1}$, where τ_R is the rotational correlation time), goes through a minimum, and then increases as temperature decreases in the slow motional regime ($T_m \propto \tau_R^{\alpha}$, $1 \leq \alpha \leq 0.5$) as found by Millhauser and Freed[42], and Saxena and Freed.[92]

Although the temperature dependence of T_m has been observed in the two motional regimes, measuring T_m near the minimum region is challenging due to 1) the broadening of the linewidth leading to lower S/N ratio, and 2) the limitation of the spectrometer to collect the signal immediately after the intense pulse, generating a spectrometer dead-time (see section 2.2).

By minimizing ring-down artifacts (*cf.*, Experimental Section) the dead time in t_2 was reduced by as much as 20 ns (*i.e.*, from ~50 to ~30 ns). For T_m ~20 ns this reduction leads to an increase in detectable echo signal by as much as a factor of 10, making 2D FT-ESR feasible. With the improved dead-time COSY-ESR, data were obtained over the entire motional range for the first time on a commercial pulse spectrometer. Thus, the plot of full curve between T_m vs. inverse temperature (Figure 2-5 and 2-6) is made possible. Such results have been previously obtained only with the help of a home-built spectrometer operating at 17 GHz using 2D FT-ELDOR.[80, 83, 96-98]

In addition, T_m varies as the frequencies in f_2 change. The variation is shown in Figure 2-6, where T_m values are extracted at the central peak and low field peak. The temperature dependence of T_m from both f_2 frequencies is comparable in the fast motional range (between 250 and 310 K). The values of T_m from the low field peak are slightly shorter than those from obtained from the central peak at temperature lower than 220 K. This feature of T_m variation is consistent with the T_m being dominated by the slow tumbling of the nitroxide.[92]

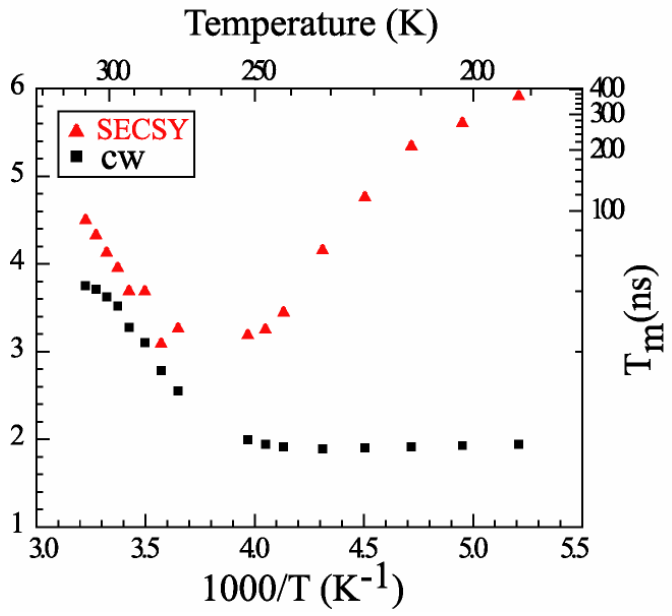

Figure 2-5: Comparison of linewidth *vs.* inverse temperature between cw (■) and SECSY (▲) experiments.

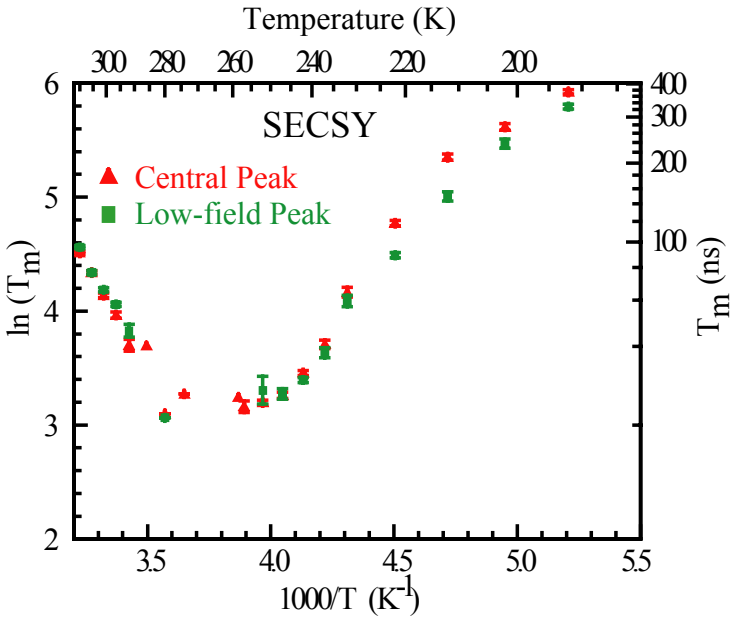

Figure 2-6: Plot of T_m *vs.* inverse temperature of central peak (▲) and low-field peak (■) of SECSY spectra**.**

- *Significance of T_m minimum in a theoretical model of rotational motion*

The phase memory time obtained by fitting along an f_1 slice, in general, depends on frequencies along f_2. A full analysis of this variation is sensitive to details of molecular dynamics.[42] We show that the resolution of the T_m minimum provides an easy distinction between the dynamical models commonly used to interpret ESR spectra. In Figure 2-5, the T_m for the central component is shown as a function of inverse temperature. Each phase memory time of the simulated spectrum was obtained by extracting a slice parallel to f_1 and determining the full-width at half-height. To quantitatively analyze the data SECSY spectra for a series of rotational correlation times, τ_R, were calculated using spectral simulations based on the stochastic Liouville equation.[38, 40, 90, 91, 99] These spectra were simulated for two models of microscopic dynamics (see Experimental Section).

Theoretical T_m values were obtained for each rotational correlation time by examining the lineshape along f_1 as described above. In order to fit theoretical T_m values (obtained versus τ_R) to experimental data (obtained versus temperature, T), a relationship between τ_R and T is needed. The correlation time is proportional to η/T where η is the viscosity of the solution and an Arrhenius-type relationship is usually used to relate τ_R and T[90, 92]

$$\ln(\tau_R/A) = E_a/RT \qquad (2\text{-}10)$$

where $A=8.4\times10^{-16}$ s and E_a=7.9 Kcal/mol. The activation energy, E_a, for this system was determined from experimental slow motional data, as described before.[92] Within experimental uncertainties this value is consistent with earlier results on analogous system in glycerol-water-trifluoroethanol solvent.[92] The parameter A was adjusted for best fit. Both parameters serve to shift the theoretical curve parallel to the 1/T axis.

Figure 2-7 illustrates the importance of the T_m values near the minimum. The resolution of the T_m values at minimum dictates the model that properly predicts the reorientation of nitroxide on the peptide chain. The model of anisotropic Brownian diffusion qualitatively predicts a similar curve but leads to reduced T_m minimum. The model of anisotropic diffusion in a reorientational potential (*i.e.*, the MOMD model) provides a better fit to the data. This model is intuitively pleasing for this system. Apparently, the nitroxide experiences an ordering potential, due to the peptide chain, which restricts its amplitude of rotation. This comparison demonstrates the sensitivity of *T_m's near the minimum* to details of motion. In addition, it has been shown that the microscopic molecular ordering but macroscopic disorder (MOMD) contributes to inhomogeneous broadening to the linewidth. This effect is observable from Figure 2-5. The comparison between T_m and T_m^* is shown. Even at the motionally narrowed limit, T_m^* is smaller than T_m. This occurs because nitroxide experiences the MOMD effect.

The scale of $\bar{\tau}_R$ at the temperature range around the T_m minimum obtained from the MOMD model is shown at the bottom of Figure 2-7. The rotational correlation time in the high temperature range (~ 310 to 280 K) is on the order of a few nanosecond. This range of τ_R is comparable to rotational motion of a small globular protein[100] (~10 KDa) whereas larger proteins trend to reorient slower, which corresponds to the dynamics at the low temperature range, including the T_m minimum. Therefore, the SESCY experiment is sensitive to the dynamics on large proteins, such as membrane-associated protein.

In conclusion, we have demonstrated the feasibility of resolving reorientational dynamics over the entire motional range in tethered nitroxides using FT-ESR even on commercial spectrometers. The scheme for minimizing the spectrometer dead-time is accomplished.

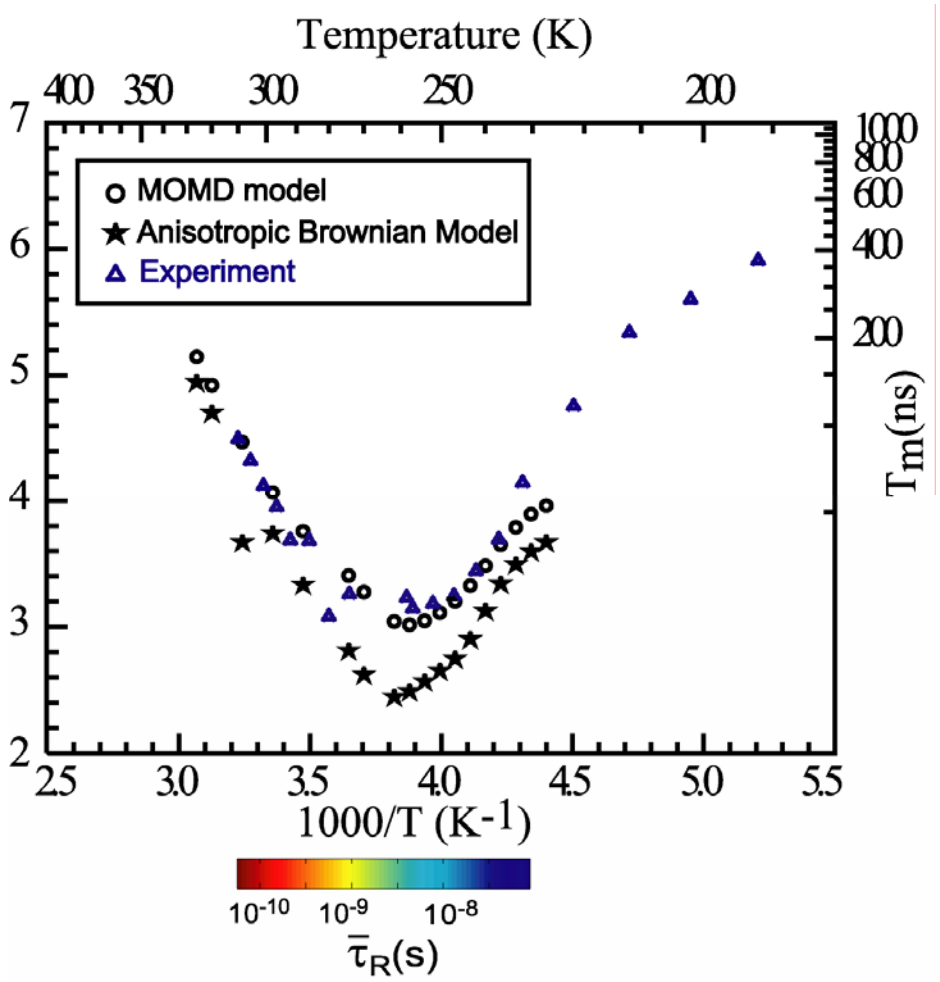

Figure 2-7: Experimental phase memory times plotted on a logarithmic scale *vs.* inverse temperature for the central component (▵). Theoretical T_m's are shown for two models of dynamics; an anisotropic Brownian diffusion model (★) and the microscopic order macroscopic disorder (MOMD) model (o). The T_m versus 1/T curve is sensitive to details of microscopic dynamics. The scale of average correlation rotational time at the temperature range from 230 to 320 K obtained from MOMD model is shown on the bottom.

The resolution of the T_m minimum allows easy distinction between commonly used models of dynamics. This opens up the possibility of using 2D ESR for the study of spin-labeled proteins, which is of significant current interest.[13, 101-108]

2.5 ACKNOWLEDGEMENT

Acknowledgment is made to the donors of the Petroleum Research Fund, administered by the American Chemical Society and the Central Research Development Fund, University of Pittsburgh for partial support of this research. Helpful discussions with Drs. Ralph Weber and Dave Schneider are gratefully acknowledged.

3.0 FLEXIBILITY AND LENGTHS OF BIS-PEPTIDE NANOSTRUCTURES BY ELECTRON SPIN RESONANCE

Part of this work, written in collaboration with Gregory Bird, Christian E. Schafmeister, and Sunil Saxena, has been published in the Journal of the American Chemical Society, 2006, V.128 (12), pages 3876-3877.

3.1 ABSTRACT

In this chapter, the application of DEER-ESR to measure structural constraints on nanomaterials is discussed. We demonstrate the use of electron spin resonance (ESR) to determine long range distances in water soluble *bis*-peptide molecular rods. ESR determined that the end-to-end length of the peptides is linearly proportional to the number of monomers. The linear shape is, therefore, easily interpreted from the data. In addition, the flexibility of the rods was quantified directly from the ESR determined the end-to-end distance distribution functions. The shape and flexibility are, then, characterized. The collaborative work presented here extends the efficacy of FT-ESR for the purpose in characterizing the structure and dynamics of organic nanomaterials; in this case, *bis*-peptide oligomers. In addition, the ESR result is compared with data from molecular dynamics simulations and paves the way to further work discussed in Chapter 4.

3.2 INTRODUCTION

We demonstrate the use of electron spin resonance (ESR) to determine long range distances in water soluble bis-peptide molecular rods. The synthesis of ever larger and more complex molecules with designed shapes and properties is an overarching goal of synthetic chemistry. An approach was developed by Levin, *et al*[109, 110] to the rapid synthesis of water soluble nano-scale molecules with designed shapes using conformationally restricted building blocks that are coupled through pairs of bonds to create spiro-ladder oligomers. In order to develop these oligomers as rod-like structural elements, quantitative information on the lengths and flexibility are required. We show that electron spin resonance (ESR) provides a natural spectroscopic method to rapidly assay these structural parameters.

Double electron-electron resonance (DEER) ESR[46,67] has been use to measure distances between two spin-labels in the range of 15-80 Å[67] for the determination of global folding patterns in proteins,[111,112,113,114] nucleic acids,[115] ionic polymers[116, 117] and conformational and aggregation states of polypeptides.[87] In this work, we use the DEER-ESR technique to quantify the end-to-end distances of *bis*-peptide molecular rods with 4-8 monomers. Not only the mean end-to-end distances were determined but also the flexibility of the molecular rods was characterized by the distance distribution functions. The shape and flexibility obtained from the series of DEER measurements of 4-8 monomer bis-peptides are both important criteria for the design of nanostructured materials with targeted functions.

3.3 METHODS

- *Synthesis of spin-labeled bis-peptide oligomers*

Figure 3-1a shows the structures of bis-peptide molecular rods of 4-8 monomers (compounds 1-5, respectively). The structure of four-mer compound is shown in Figure 3-1b in ball-and-stick format. The five *bis*-peptide oligomers, **1-5**, with n = 4-8 monomers were synthesized in parallel and labeled at the ends with nitroxides.[109] The synthesis procedures were reported by Leven, *et al*.[109, 110] The mass of each final product was confirmed by mass spectrometry.

- *Electron Spin Resonance Spectroscopy*
  - *Sample preparation*

For ESR experiments, 0.2 mM of the double-labeled molecules were dissolved in 70% buffer (50 mM phosphate buffer, pH 7.4, 200 mM NaCl, 3 mM NaN_3, 1 mM EDTA) and 30% glycerol. Each sample (~10 μl) was placed in a ~1.5 OD mm. pyrex capillary tube and flash frozen in liquid nitrogen immediately before insertion into the cavity.

  - *FT-ESR spectroscopy*

The ESR experiments were performed using a Bruker EleXsys E580 CW/FT X-band ESR spectrometer equipped with a Bruker X-band ER 4118X-MS2 split ring resonator for compounds **1, 3** and **4** (n=4, 6 and 7), and 4118X-MS3 for compound **2** and **5** (n=5 and 8). Both resonators provided identical results for the same measurement. The temperature was controlled by an Oxford ITC605 temperature controller and an ER 4118CF gas flow cryostat. All experiments were performed at the temperature of 80 K.

a)

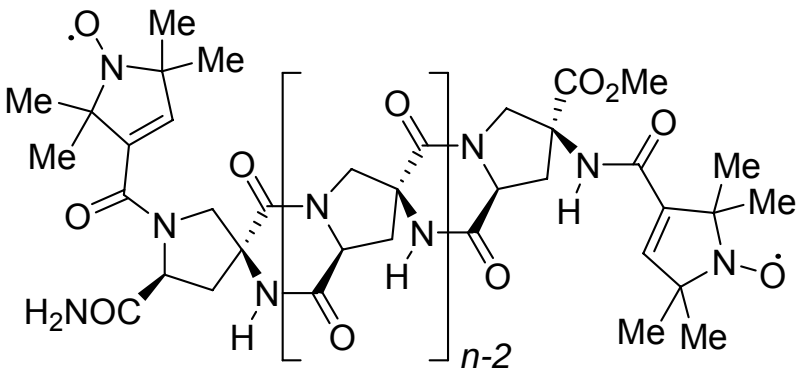

1 (*n* = 4), **2** (*n* = 5), **3** (*n* = 6), **4** (*n* = 7), **5** (*n* = 8)

b)

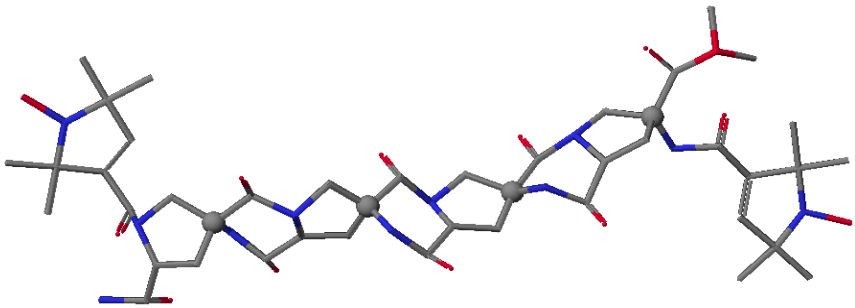

Figure 3-1: a) Structure of *bis*-peptide oligomers of 4-8 monomers (compounds 1-5, respectively); b) Ball-and-stick structure of a four-mer *bis*-peptide.

Four-pulse DEER experiments were obtained with a resonator Q ≤ 100 and an ASE TWTA with an output power of 1 kW. The pulse sequence for generating the dipolar time evolution data is shown in Figure 3-2. A two-step phase cycle was used for baseline correction. The observer frequency, ν_A, was set at the central field of the spin label peak which is around 9.5-9.6 GHz, and the pump frequency, ν_B, was set at 70 MHz higher. The lengths of the $\pi/2$ and π pulses were 24 and 48 ns, respectively. The interpulse delays were 200 ns for τ_1, and 2200 ns for τ_2. The increment of time T after the second pulse was 16 ns for 128 points. For each step of the phase cycle 500 averages were collected at a repetition rate of 1 kHz. The acquisition time used for each sample was roughly 24 hours.

- *Data Analysis*

The 4-pulse DEER time domain data were processed before acquiring the distance distribution functions. The background decay due to intermolecular interaction was subtracted by fitting the last 75% of the data with a first-order polynomial function. For compounds 3-5 (n=6-8), the time domain data was smoothed by applying a hamming function and zerofilled to 512 points before analyzing the data. Fourier transforms of the processed data provided the frequency spectra. The time domain data was analyzed using the DEERAnalysis 2004 program which is freely available on the web.[118] The distance distribution functions were obtained using the Tikhonov regularization method with the regularization parameter of 4.0 for compounds **1-2** (n = 4-5), and 50.0 for compounds **3-5** (n = 6-8). In this analysis no constraints on the maximum possible distance was imposed. The data for compound **5** (n=8) was also fit with the program from Chiang, *et al*[72] using a regularization parameter determined by the L-curve criterion. Both programs provided the same result.

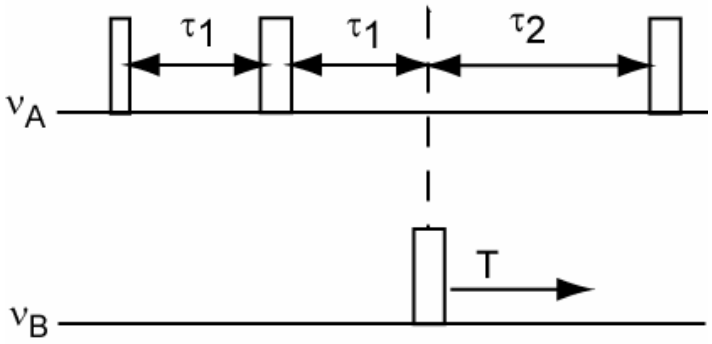

Figure 3-2: Four-pulse DEER sequence.

- *Molecular Dynamics Simulations*

Molecular dynamics simulations were carried out *in vacuo* using the Amber94 force field.[119, 120] Five-nanosecond *in vacuo* molecular dynamics simulations at 300 K were carried out on each compound **1-5** (n=4-8). Histograms of the distance between the two nitroxide nitrogens were calculated and overlaid on the population distributions determined by ESR.

- *Determination of mean distance and standard deviation*

The mean distance and standard deviation (σ) were calculated from the distribution functions using first and second moment as defined by Equations 3-1 and 3-2

$$< r > = \frac{\sum_{r_1}^{r_2} r \cdot P(r)}{\sum_{r_1}^{r_2} \mathrm{P(r)}} \qquad (3\text{-}1)$$

$$\sigma = \sqrt{\frac{\sum_{r_1}^{r_2} r^2 \cdot P(r)}{\sum_{r_1}^{r_2} P(r)} - < r >^2} \qquad (3\text{-}2)$$

where P(r) is the distance distribution function, r_1 and r_2 are the lower and upper range of the distribution function, and σ is the standard deviation.

3.4 RESULTS AND DISCUSSION

The four-pulse DEER data on compounds **1-5** performed at 80 K are shown in Figure 3-3. In general, the DEER signal, V(t), is composed of two contributions; *i.e.*, *inter*- and *intra*-molecular interactions, and can be represented as a multiplication

$$V(t) = V_{inter}(t)\, V_{intra}(t) \qquad (3\text{-}3)$$

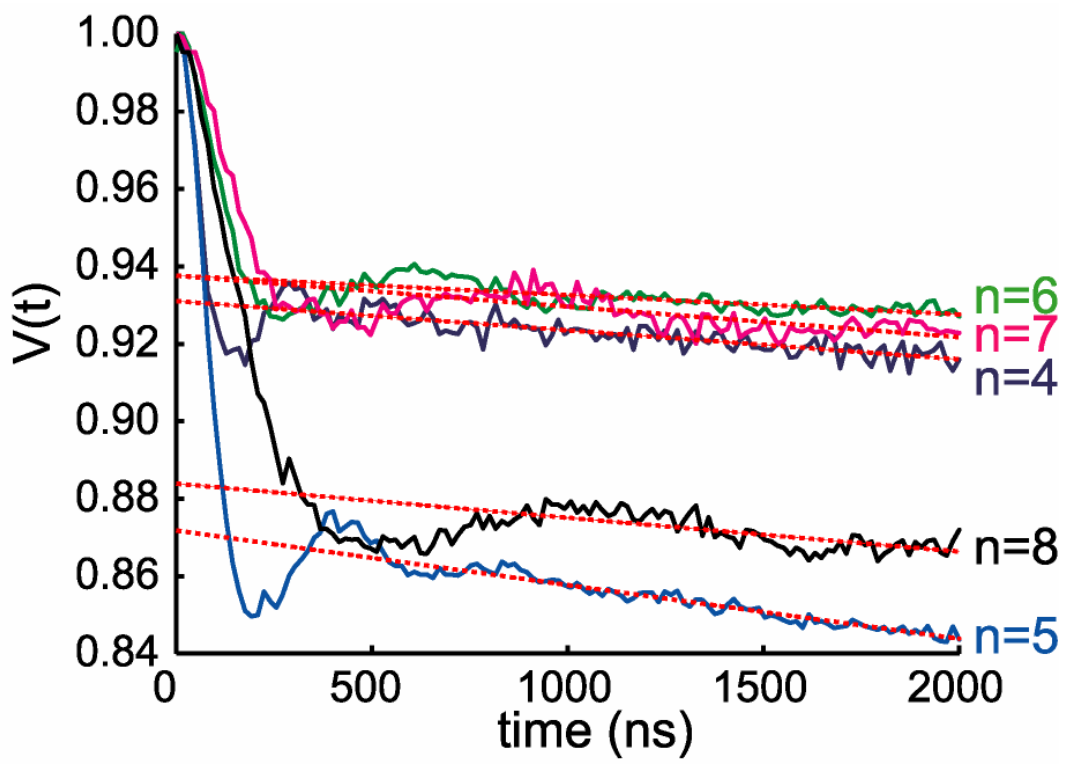

Figure 3-3: Time domain DEER data (solid line). The dashed lines indicate the functional form of the signal contributed to the intermolecular interaction (see text).

where $V_{inter}(t)$ and $V_{intra}(t)$ are the signals due to the intermolecular and intramolecular interactions between spin labels, respectively. Only the contribution of *intramolecular* interactions is of interest. The distance between interacting spins can be obtained from this $V_{intra}(t)$ signal. To obtain $V_{intra}(t)$ it is necessary to know $V_{inter}(t)$.

In most cases, the signal of $V_{intra}(t)$ oscillates due to the electron dipole interaction, and in the beginning of the acquisition it dominates the measured V(t). The $V_{inter}(t)$ signal contributes only to the background decay. The reduction of intermolecular interaction can be done by preparing diluted samples (usually 0.1-0.2 mM is sufficient for a rigid sample with interspin distance of ~20 Å) and by data processing. $V_{inter}(t)$ can be determined by fitting the latter part of V(t) as a background correction. The method of the background correction and the use of the data to determine the number of spins are discussed in Appendix B. In this case, $V_{inter}(t)$ signals of *bis*-peptide oligomers are subtracted out by fitting with a functional form shown as the dashed lines in Figure 3-3.

The intramolecular signal, $V_{intra}(t)$, after the subtraction of intermolecular contribution is shown in Figure 3-4a. The frequency pattern after Fourier transform of $V_{intra}(t)$ is given by

$$\nu_{1,2} = \frac{\mu_0 g_1 g_2 \beta^2 \left(3\cos^2\theta - 1\right)}{4\pi h r^3} + J \qquad (3\text{-}3)$$

where g_1 and g_2 are the isotropic g-factors of each electron, β is the Bohr magneton, μ_0 is vacuum permeability, h is Planck's constant, r is the interspin distance, and θ is the angle between the magnetic field and the interspin vector. J is the exchange interaction, which is negligible for r > 15 Å.

At 80 K a "Pake" pattern[62, 70] is obtained in which the characteristic turning points corresponding to the parallel and perpendicular orientations [*i.e.*, $\theta = 0^0$ and $\theta = 90^0$ in Equation (3-3)] of the interspin vectors with respect to the dc-magnetic field are readily observable. The θ

= 0^0 turning point has much lower intensity but typically the $\theta = 90^0$ peak is clearly visible. Thus the interspin distance, r, can be readily obtained from the DEER spectrum.

Qualitatively, the frequency of the $\theta = 90^0$ peak in Figure 3-4b decreases as the number of monomers, n, increases, indicating an increase in mean end-to-end length. The spectra were inverted to obtain the distance distribution functions, P(r), using the DEERAnalysis 2004 program.[118,21] In the analysis a Tikhonov regularization method[74] was used.

The distance distribution functions, P(r), for compounds **1-5** are shown in Figure 3-5a. The mean distance, $\bar{r}$, and the standard deviation, σ, for these P(r), calculated using a moment analysis (see methods section), are shown in Figure 3-5b, and c. The error in mean distance, estimated from the spectral resolution, is ~1.0-1.7 Å. The "linear" rod-like shape of these materials is readily interpreted from the plot of mean distances versus n. The linear fit to the data of Figure 3-5b indicates that each building block adds 2.7 Å to the average distance between the spin probes.

Five-nanosecond molecular dynamics simulations were carried out *in vacuo* at 300 K on each oligomer. Figures 3-6 to 3-10 show the distance distribution functions obtained from molecular dynamics and from ESR. Within experimental resolution, the estimates of the mean distances from dynamics are in reasonable agreement with the experiments for n=4 to 7. The distribution functions for compounds **1-2** (*cf.* Figures 3-6 and 3-7) appear to have physically unreasonable lobes on the upper end (large r values). These are possibly due to the fact that the Tikhonov regularization procedure is mathematically ill-posed in the presence of the noise.

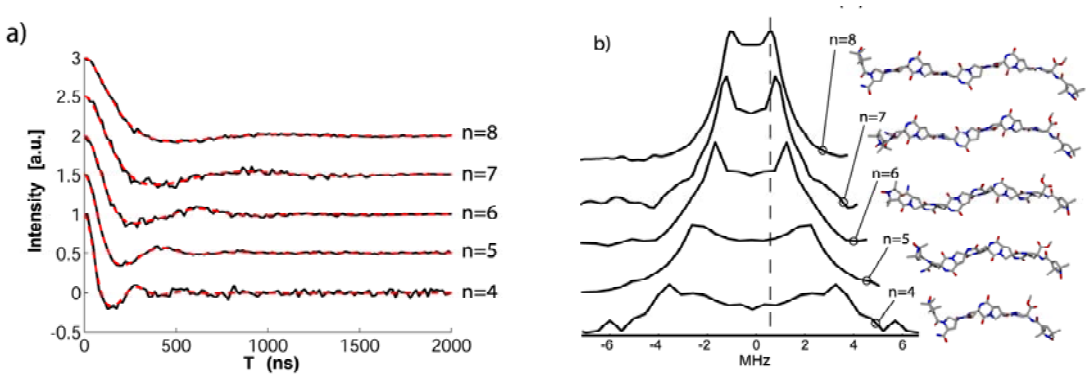

Figure 3-4: a) Time domain DEER data (black) with the simulated signal (red), b) Four-pulse DEER spectra and the structures of compounds 1-5 are shown. The vertical dashed line is to guide the eye in distinguishing the peaks.

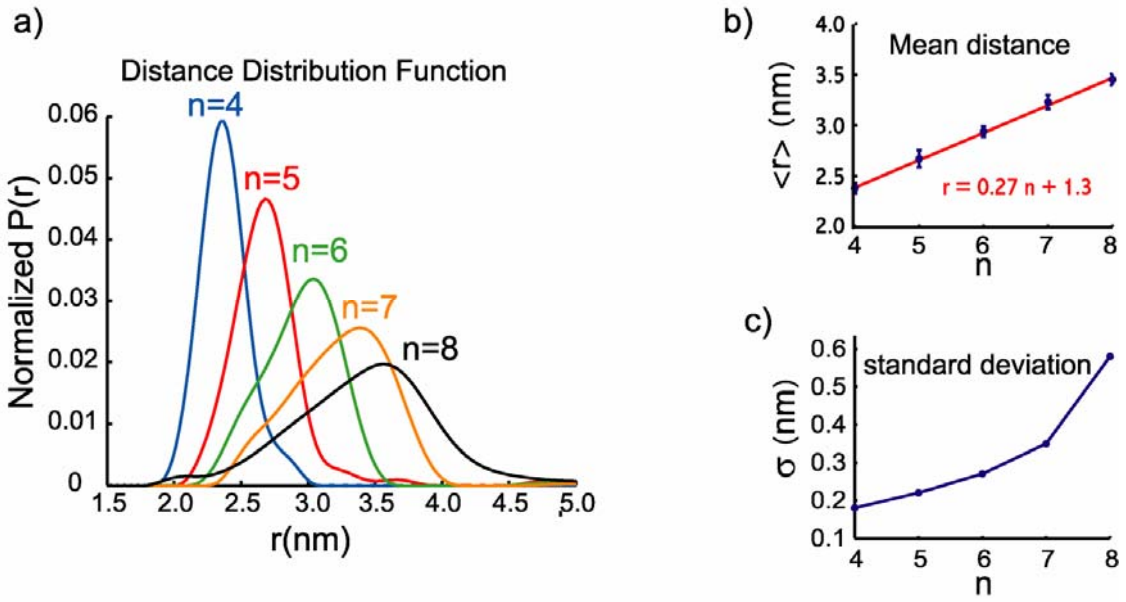

Figure 3-5: a) The experimental distance distribution function, P(r), (b) the mean distance and (c) the standard deviation for compounds 1-5 are shown.

The use of a better regularization parameter of 10, obtained by using an L-curve criterion, was successful in suppressing these lobes.

In an alternative approach the ESR data was also inverted using the Tikhonov regularization method with limits imposed on the maximum allowable distance. Both methods yielded virtually identical distance distribution functions for compounds **1**-**5** (Figures 3-6 to 3-10). For compounds **1** and **2** (n=4 and 5) molecular dynamics predicts a significant population of conformers with interspin distances shorter than 2 nm (*cf.*, Figures 3-6 and 3-7). These conformers are unlikely to be sampled by the DEER experiments due to the use of pump pulses of 48 ns.

Limitations in the excitation bandwidth of this pulse are expected to suppress the distance distribution function below 2 nm,[121] which possibly accounts for the discrepancy between experiment and dynamics in the lower wings of the distribution function. The mean distance and σ values obtained from MD compared with those from experimental values are reported in Table 3-1. Within this experimental limitation, the estimates of $\bar{r}$ from dynamics are in reasonable agreement with the experiments for n=4-7. However, molecular dynamics overestimates the mean distance for n=8 by ~3.5 Å. Distributions from molecular dynamics also progressively overestimate the most probable internitroxide distance for long scaffolds (by ~2, 2.5, and 7 Å for n=6, 7, and 8, *cf.* Figure 3-8 to 3-10). The results are summarized in Table 3-1. The flexibility of the molecular rods can be characterized by the standard deviation, σ, of the distribution function. The standard deviation increases from 1.8 Å for n=4 to 5.8 Å for n=8.

Table 3-1: Distance and standard deviation of n=4-8 oligomers

n	Experimental		Molecular Dynamics	
	<r> (Å)	σ (Å)	<r> (Å)	σ (Å)
4	23.7 ± 1.0	1.8	21.7	2.6
5	26.7 ± 1.7	2.2	24.0	3.4
6	29.4± 1.0	2.7	28.5	3.9
7	32.3 ± 1.4	3.5	32.9	4.1
8	34.5 ± 1.1	5.8	38.0	3.8

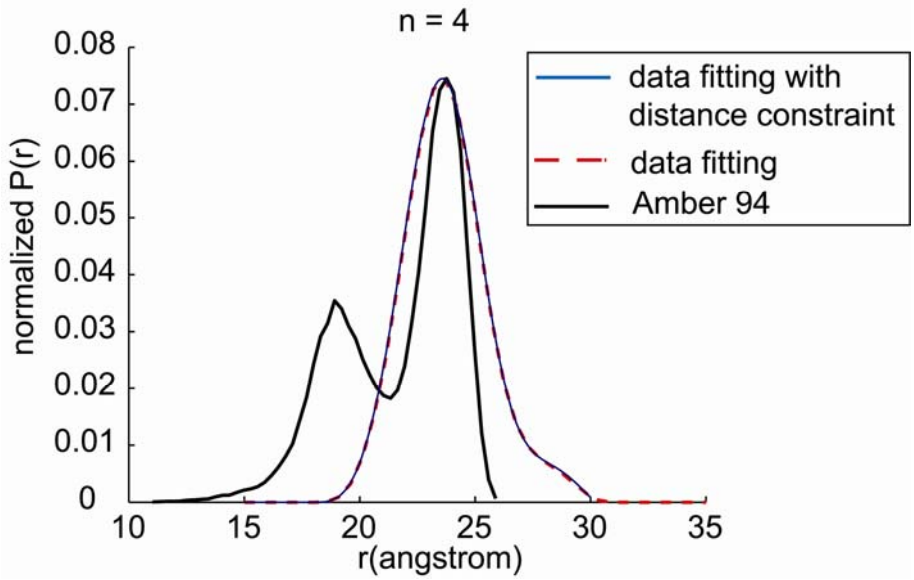

Figure 3-6: Comparison of the distance between nitroxide nitrogens calculated from a 5 nanosecond Amber molecular dynamics simulation at 300 K of the n=4 labeled scaffold (black) with the distance distribution determined from ESR for the same molecule.

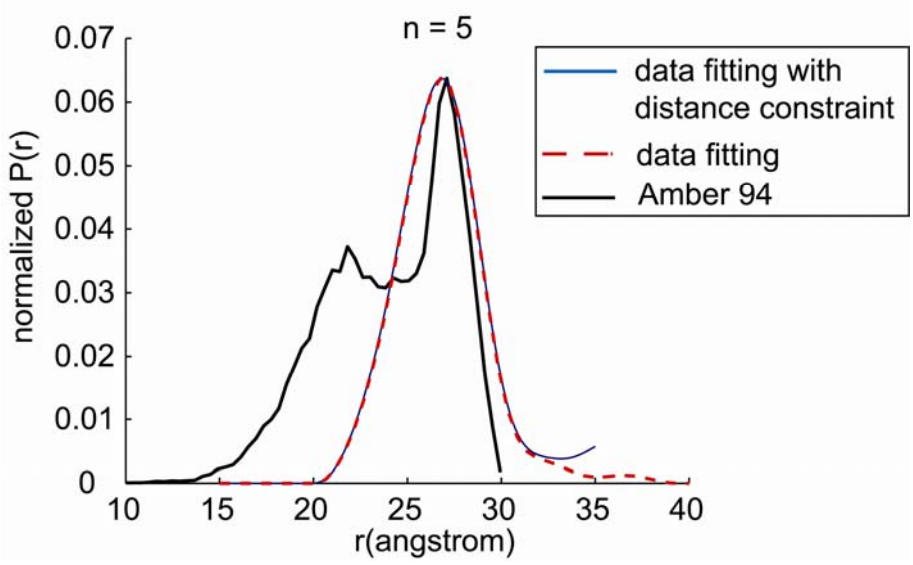

Figure 3-7: Comparison of the distance between nitroxide nitrogens calculated from a 5 nanosecond Amber molecular dynamics simulation at 300 K of the n=5 labeled scaffold (black) with the distance distribution determined from ESR for the same molecule.

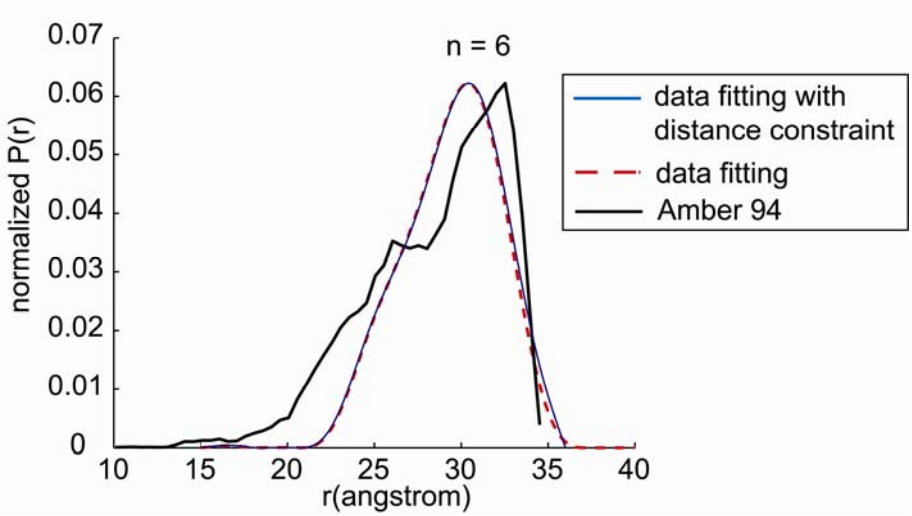

Figure 3-8: Comparison of the distance between nitroxide nitrogens calculated from a 5 nanosecond Amber molecular dynamics simulation at 300 K of the n=6 labeled scaffold (black) with the distance distribution determined from ESR for the same molecule.

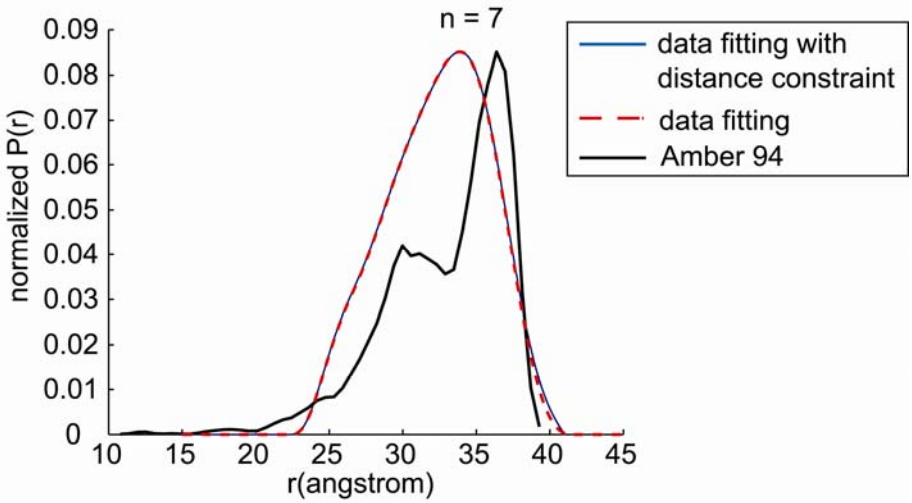

Figure 3-9: Comparison of the distance between nitroxide nitrogens calculated from a 5 nanosecond Amber molecular dynamics simulation at 300 K of the n=7 labeled scaffold (black) with the distance distribution determined from ESR for the same molecule.

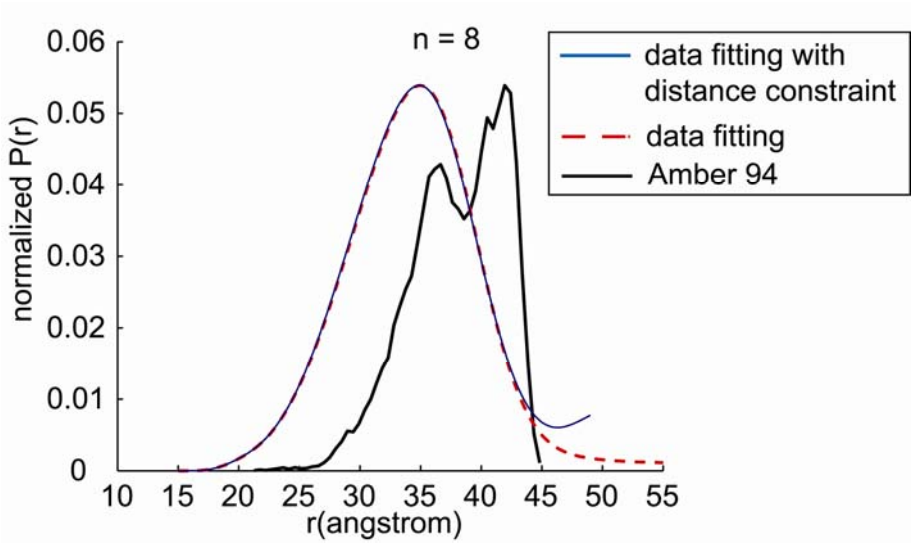

Figure 3-10: Comparison of the distance between nitroxide nitrogens calculated from a 5 nanosecond Amber molecular dynamics simulation at 300 K of the n=8 labeled scaffold (black) with the distance distribution determined from ESR for the same molecule.

In Figure 3-11, we compare the experimental data (red) for n=8 with simulated DEER data based on the probability distribution predicted by molecular dynamics (blue), and with the DEER data fit based on the Tikhonov method (dashed line). It is evident that the experimentally derived distribution function yields a better fit compared to the simulated data based on molecular dynamics results.

Snapshots from the dynamic simulations for n=4 and n=8 (Figure 3-12) are presented to illustrate the flexibility of these molecules according to the dynamic simulations. As the number of the *bis*-monomers increases in the nanochain, the flexibility also increases. It is interesting to note that a well-defined and rigid geometry of the monomer can be easily predicted due to the fused six- and five-membered rings of the di-keto-piperazine and pyrrolyl rings. From the results of ESR data and MD simulations, it is clear that when the monomers are joined together, each monomer creates higher flexibility as it is added to the chain. The increase of flexibility is more than what we first expected. Unfortunately, the MD simulations overestimate the distance distributions of long oligomers of n=6-8. Therefore, we also investigated the addition of explicit solvent and parameterizations of the force field for these molecules. The results are discussed in Chapter 4.

The key advantage of the use of ESR is twofold. First, large distance constraints can be measured from which the overall shape of the conformationally restricted material can be rapidly inferred. NMR has been used to determine short-range distances in bis-peptides[109, 110] but the rod-like nature of these materials precludes the measurement of distance between residues far apart in the linear sequence. This can lead to a substantial uncertainty in the modeling of the overall structure.

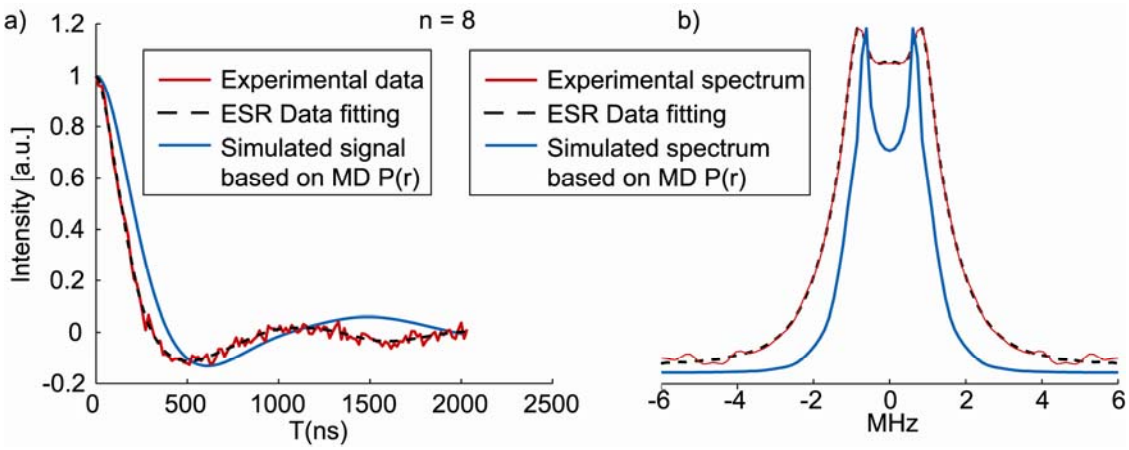

Figure 3-11: Overlay of the DEER time traces (a) and frequency spectra (b) of experimental data (red), ESR data fit (dashed black), and simulated DEER signal using the P(r) derived from molecular dynamics (blue) for n = 8 scaffold.

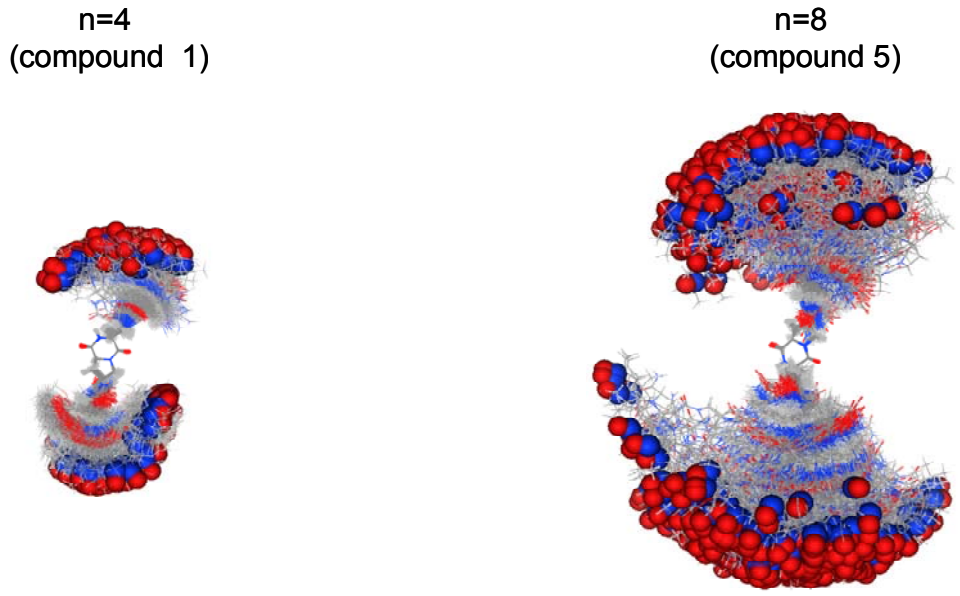

Figure 3-12: Superposition of the last 500 picoseconds of the five-nanosecond molecular dynamics simulation for the n=4 (left) and n=8 (right) oligomers. The central di-keto-piperazine ring was aligned for each structure and the nitroxide N-O atoms are rendered as solid spheres

In principle, energy transfer in FRET[51, 110, 122] is sensitive to distances in these length scales. However, the correct interpretation of the energy transfer in terms of distances requires a careful accounting of molecular dynamics.[52] Second, ESR measures the full distance distribution function, from which the flexibility of the nanostructured materials can be directly assayed. The shape and flexibility are both important criterions for the design of nanostructured materials with targeted functions.

We show that the overall shapes and flexibility of these rods can be obtained using ESR. In addition, the ESR result can be used to check the accuracy of force field for MD simulations. The data show that Amber94 force field calculations performed *in vacuo* provide similar mean distances and flexibility only for short oligomers (n=4 and 5), but overestimate the distances for long oligomers (n=6-8).

Given that the MD simulations are inefficient for predicting the flexibility and distances of the oligomers, we generate a jointly stiff-segment model to enhance our ability to rapidly determine the structure of the bis-peptides. The details of the model and the improved results compared to those from ESR are discussed in Chapter 4.

3.5 ACKNOWLEDGEMENT

This research is supported by the NSF CAREER Award (MCB0346898).

4.0 ANALYSIS OF THE DYNAMICAL FLEXIBILITY OF *BIS*-PEPTIDE NANOSTRUCTURES

This work, written in collaboration with Christian E. Schafmeister, and Sunil Saxena, has been submitted to the Journal of Magnetic Resonance.

4.1 ABSTRACT

We present an approach to predict the overall structure and flexibility of *bis*-peptide nanostructures from Electron Spin Resonance (ESR) distance measurements. These molecules are composed of conformationally restricted monomers, and results on a series of *bis*-peptide oligomers containing 4 to 8 monomers are presented. Based on Molecular Dynamics (MD), a joint-stiff segment model is generated to represent the *bis*-peptide backbones. A scheme is established to exploit information on end-to-end distance distribution functions obtained by ESR to optimize the force fields used in the joint-stiff segment model. The model provides end-to-end distribution functions for the oligomers that better fit the ESR results than those originally obtained from MD simulations. The results also provide information on the distribution of orientations of a monomer with respect to the preceding monomer. An optimized orientational angle of $\gamma\gamma_0$ was -21.06°. The other angles were consistent with MD predictions. The optimized

force constants of k_α=2.144 kcal/(mol.rad^2), k_β=3.245 kcal/(mol.rad^2), k_γ=2.876 kcal/(mol.rad^2), and $k_{\beta\beta}$=3.041 kcal/(mol.rad^2) were found. Information of these orientational parameters enhances our ability to predict the shapes and flexibility of new oligomers constructed using an arbitrary number of this monomer.

4.2 INTRODUCTION

Synthetic nanomaterials, including artificially-designed peptides and polymers[118], are composed of a chain of chemical building blocks. *Bis*-peptides[109, 110, 123] are a class of oligomers composed of conformationally restricted monomers. The oligomers are designed to hold specific well-defined structures and geometries. The global shape and flexibility of these nanomaterials depend on the orientations and flexibility of successive building blocks. Information on both shape and flexibility of the *bis*-peptide oligomers is essential for the design and applications of new nano-materials useful for future nanosized devices and bio-sensors. Therefore, a technique that provides both structural and dynamical information becomes necessary.

Electron spin resonance (ESR) provides these pieces of information by measuring the end-to-end distance distribution. ESR has been used to quantify the distances between two spin-labeled sites in a range of 1.5 to 8.0 nm[61, 124-127] in peptides,[84] proteins,[112, 113, 128-133] nano-sized oligomers,[115, 134] RNA,[135-138] aggregates of peptides in a membrane,[87, 139-141] and to determine the orientations and distances of radical centers involved in the photosynthesis system.[142, 143] By labeling spin-labels at two ends of the nanostructures, we have demonstrated, in the previous work,[144] the use of ESR to quantify the lengths and flexibility of bis-peptide oligomers with 4-8 building blocks. The flexibility was quantified by the standard deviation of the label-to-label

distance distribution functions. The distance distribution functions were also compared with those from molecular dynamics (MD) simulations. The distance distributions obtained by molecular dynamics overestimates the most probable interspin distance for the long oligomers (6-8 building blocks) by as much as 7 Å, limiting by applicability of the MD simulation to predict the overall structures.[144] The failure of MD simulation in predicting the overall structures might be because the force field used in MD are not suitable to represent the dynamics of these materials. Therefore, an approach that measures appropriate structural parameters is necessary. Recently, Jeschke *et al*[145] elegantly used a coarse-grained model to obtain persistence length and flexibility of molecular rods of poly(para-phenylene ethynylene)s from the ESR results. In these molecules the structural parameters were simplified due to the presence of double and triple bonds in the oligomers. For the case of bis-peptide oligomers, however, the determination of geometrical parameters is key to elucidating their structure and dynamic flexibility. In this work, we provide an approach to analyze the flexibility of bis-peptide nanostructures and measure geometric constraints from ESR results. The constraints are useful for the design of new nanomaterials.

4.3 METHODS

- *Conformational model of bis-peptide nanostructures*

In order to enhance our ability to predict the overall shapes of bis-peptide nanostructures from ESR, we generated a joint-stiff segment model to describe the possible conformations of the oligomers. The sequence of the oligomers is built from a fundamental monomer unit. The procedure is summarized as shown in Scheme 1.

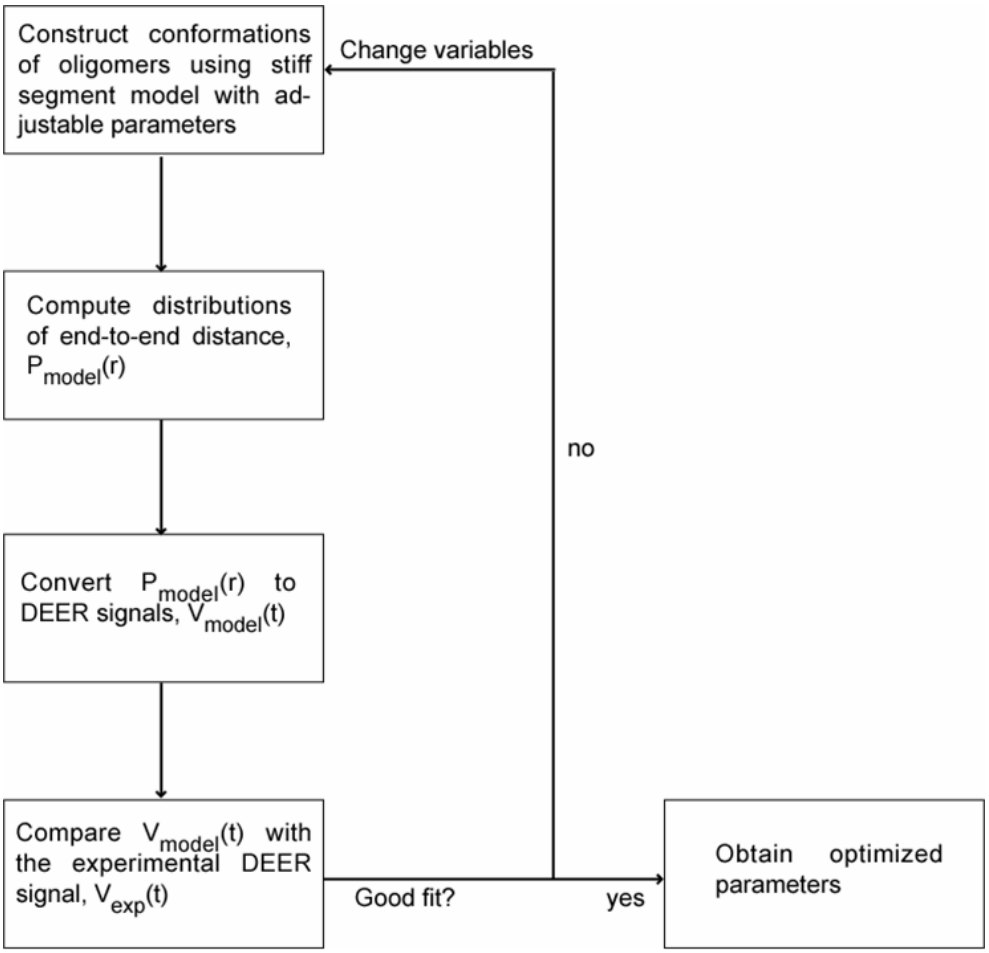

Scheme 4-1: Flow chart showing the process in obtaining the optimized parameters

Each oligomer is represented as a series of joint-stiff segments.[146] The distribution of the end-to-end length depends on the orientation that each stiff segment holds with respect to the preceding segment.

A potential, guided by the MD simulation, is constructed with several adjustable parameters. Then, a conformational ensemble of end-to-end lengths is constructed, and the end-to-end distance distribution of the ensemble, $P_{model}(r)$, is calculated. The theoretical DEER signal, $V_{model}(t)$, is calculated based on the $P_{model}(r)$. Finally, the parameters are optimized by comparing the DEER signal obtained from the model, $V_{model}(t)$, to that from the experiment, $V_{EXP}(t)$. Details of each step are provided in subsequent subsections. The detail of the model and the procedure for obtaining the geometrical constraints are described in this section.

A model of *bis*-peptide oligomers is developed by using a sequence of relatively stiff segments, r_{ij}, connected by flexible joints. The subscripts *i* and *j* represent two adjacent monomer units. In the model, the quaternary carbon center of each monomer locates a joint. The position of the joint is given by Cartesian coordinates of (x_i, y_i, z_i) with the origin on a quaternary carbon center as shown in Figure 4-1a and 4-1b. The axes (x_i, y_i, z_i) are shown in Figure 4-1a. The direction of the x-axis is defined as the sum of a vector connecting the quaternary carbon *i* with the carbon labeled CC (*i*-CC) and the vector labeled *i*-CN (see Figure 4-1a). The x-y plane is the plane connecting CN-i-CC-CN. The y-axis direction points towards the vector connecting the carbon labeled CC and the nitrogen labeled CN. The z-axis is generated following the right-handed rule. The locations of the spin-labels at the ends are specified by two coordinates (x_{SL1}, y_{SL1}, z_{SL1}) and (x_{SL2}, y_{SL2}, z_{SL2}) at the positions of the nitroxide's nitrogens. The directions of these coordinates are not defined because they are not important, since we are interested only the locations of the spin-labels.

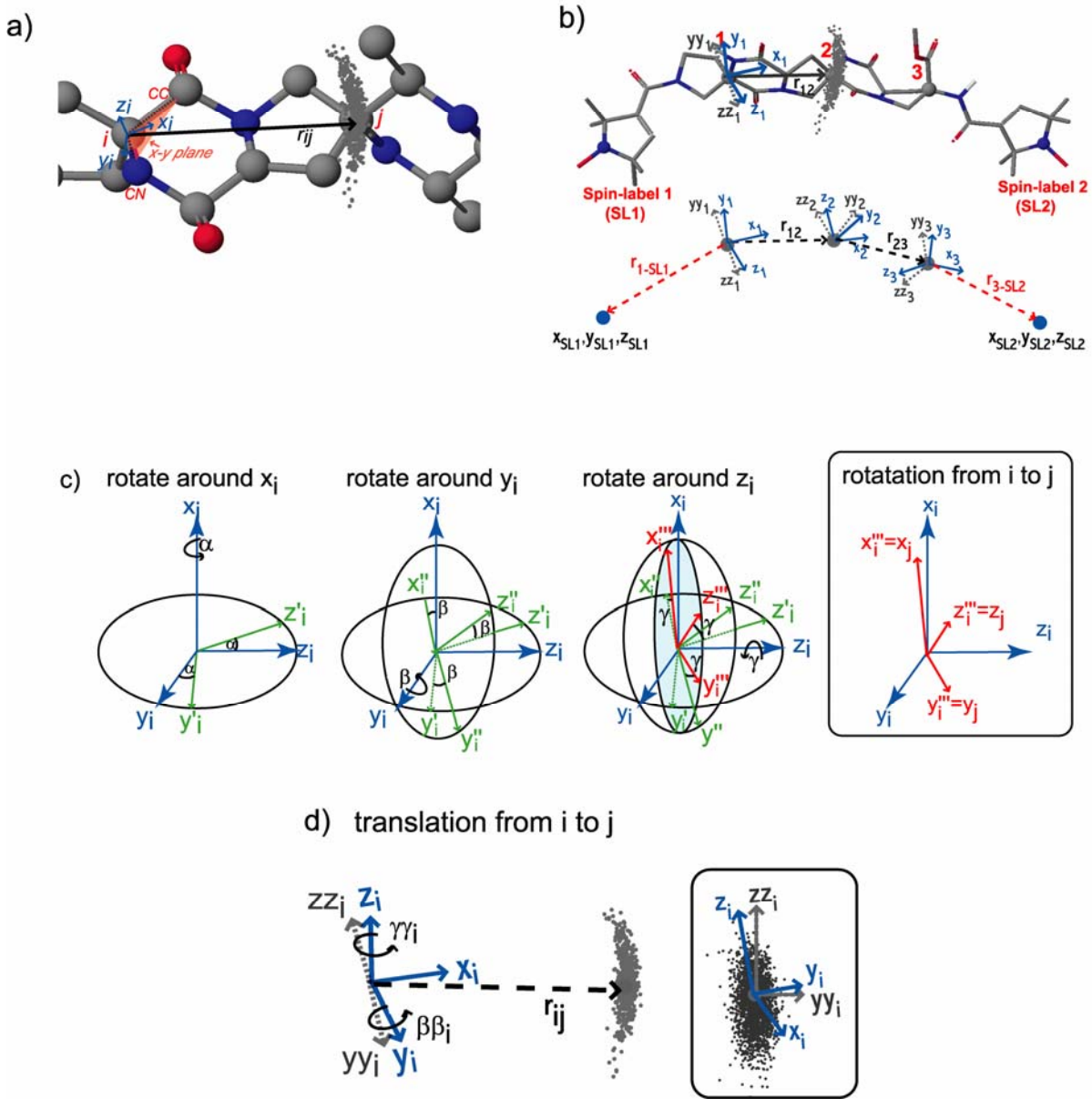
a)
CC
zi
xi
i
yi
x-y plane
CN
rij
j
b)
yy1
y1
x1
1
2
3
r12
zz1
z1
Spin-label 1
(SL1)
Spin-label 2
(SL2)
zz2
z2
yy2
y2
x2
r23
yy3
y3
x3
z3
zz3
r1-SL1
r3-SL2
xSL1,ySL1,zSL1
xSL2,ySL2,zSL2
c)
rotate around xi
rotate around yi
rotate around zi
rotatation from i to j
xi
α
z'i
ω
zi
yi
y'i
x''i
β
z''i
y''i
x'''i
γ
z'''i
y'''i
x'''i=xj
z'''i=zj
y'''i=yj
d)
translation from i to j
zzi
zi
γγi
xi
rij
ββi
yyi
yi

Figure 4-1: a) Molecular structure of the monomer showing the normalized axes (x_i, y_i, z_i) centered at the quaternary carbon *i*. The direction of the x-axis is defined as the sum of a vector connecting the carbon *i* with the carbon labeled CC (*i*-CC) and a vector *i*-CN. The x-y plane is the plane connecting CN-i-CC-CN. The y-axis is orthogonal to the x-axis and points towards the vector connecting CC to CN. The z-axis is generated following the right-handed rule; b) *Top panel*: a three-mer bis-peptide showing the Cartesian coordinate of (x_1, y_1, z_1) centered at the quaternary carbon centers. A stiff segment vector r_{12} connects monomer 1 to 2. As a result of Amber94 simulation, the grey dots represent the possible locations of the quaternary carbon of the second monomer showing an ellipsoidal motion. This motion influences the direction of vector r_{12}. Therefore, an additional coordinate system (yy_1, zz_1) is required in order to direct the vector r_{12} to the middle of the ellipsoidal motion, i.e., to the next quaternary carbon. The zz_i axis is along the longitudinal axis of the ellipsoidal motion and yy_i is perpendicular to the axis. The angles $\beta\beta_i$ and $\gamma\gamma_i$ rotate the y_i axis, and the z_i axis, respectively. They provide the direction to translate the coordinate *i* to *j*. *Lower panel:* The joint stiff-segment model of a three-mer bis-peptide showing vectors r_{12}, and r_{23} vectors that connect monomer 1 to 2 and 2 to 3, respectively. The vectors $r_{1\text{-}SL1}$ and $r_{3\text{-}SL2}$ connects the first monomer with the first spin-label, and the last monomer with the second spin-label, respectively; c) Rotation operations transform (x_i,y_i,z_i) to (x_j,y_j,z_j) starting with rotation around x_i-axis, then, subsequent rotation around the y_i, and z_i axes. The angles, α, β, γ, are rotated around x_i, y_i, and z_i, respectively. The inset shows the old (x_i,y_i,z_i) and new (x_j,y_j,z_j) axes. d) Parameters involve in the translation from the monomer i^{th} to j^{th}, i.e., the length (r_{ij}) and direction of the vector r_{ij}. The direction of r_{ij} requires the angles $\beta\beta_i$ and $\gamma\gamma_i$.

The main-chain is constructed by connecting the quaternary carbon centers with relatively stiff segment vectors, r_{ij}. Figure 4-1b (upper panel) shows the structure of the *bis*-peptide oligomer with three monomer units, and the coordinate of the first building block is shown. The lower panel of Figure 4-1b shows details of the model. Vectors, $\vec{r}_{12}$, and $\vec{r}_{23}$ represent the directions and distances that connect these monomers to the next adjacent unit. In addition, the vectors connecting the spin-labels to the main chain are carried out in the same approach. The vector $r_{1\text{-}SL1}$ and $r_{n\text{-}SL2}$ connect the first monomer to the first spin-label, and the last monomer to the second spin-label, respectively.

To obtain an end-to-end distance of each oligomer, the coordinates indicating the locations of the building blocks in the chain and the two spin-labels are required. In the model, the quaternary carbon center of the first building block is set at the origin point (0,0,0). The coordinate of the next building blocks and spin-labels are calculated with respect to that of the first building block. The transformation from one building block to the next is performed by *rotational* and *translational* operations that are illustrated in Figure 4-1c and 4-1d, respectively. To perform those operations, which transform coordinate *i* to *j*, six parameters are needed. Three of these are the angles, α_i, β_i, and γ_i involved in the rotation of axis (x_i,y_i,z_i) to (x_j,y_j,z_j). Figure 4-1c shows the sequence of the rotation. The x_i-axis was rotated at the angle α_i. Then, the rotation was subsequently performed around y_i and z_i axes, at the angles β_i and γ_i, respectively. This rotational operator, $\hat{R}_{ij}$, is described in Equation (4-1).

$$\hat{R}_{ij} = \hat{R}_{z,i}(\gamma_i)\hat{R}_{y,i}(\beta_i)\hat{R}_{x,i}(\alpha_i) \qquad (4\text{-}1)$$

Here, $\hat{R}_{x,i}(\alpha_i), \hat{R}_{y,i}(\beta_i), \text{and } \hat{R}_{z,i}(\gamma_i)$ are the rotation matrices[147] rotating at angle α around x_i-axis, β around y_i-axis, and γ around z_i-axis, respectively.

The translational operation translates monomer *i* to *j*. Molecular dynamics simulation helped us determine the initial parameters that transforms monomer *i* to *j* in the main chain. Here, Amber94 force field[119] was performed on a three-mer *bis*-peptide in water. The simulation predicts the location of the second quaternary center as an ellipsoidal motion as shown by the grey dots in Figure 4-1a and 4-1b. This ellipsoidal motion influences the direction of the segment vector r_{ij} for the translation from monomer *i* to *j*. The motion is represented as the grey dots in Figure 4-1a and 4-1b, and results in the vector r_{ij} not aligning with the axis x_i. Therefore, the additional axes of yy_i and zz_i concerning the ellipsoidal motion of the next adjacent monomer, *j*, is introduced. The coordinate (yy_i, zz_i) directs the segment vector r_{ij} to point at the middle of the ellipsoidal motion, i.e., to the equilibrium position of the next quaternary carbon *j* (see Figure 4-1d). Three parameters involved in the translation from monomer *i* to *j* are the length of vector r_{ij}, the angles $\beta\beta_i$, and $\gamma\gamma_i$ that rotate around y_i and z_i axes, respectively. Equation (4-2) describes the sequence of translation.

$$\vec{T}_{ij} = r_{ij}\, \hat{R}_{z,i}(\gamma\gamma_i)\, \hat{R}_{y,i}(\beta\beta_i)\, \vec{u}_{x,i} \qquad (4\text{-}2)$$

The vector $\vec{u}_{x,i}$ is a unit vector along x_i-axis. The operators $\hat{R}_{y,i}(\beta\beta_i)$, and $\hat{R}_{z,i}(\gamma\gamma_i)$ are rotation matrices rotating around y_i-axis at $\beta\beta_i$ angle, and z_i-axis at $\gamma\gamma_i$ angle, respectively, and r_{ij} is the length between the monomer *i* and *j*. The total transformation from monomer *i* to *j* is performed by:

$$\vec{v}_j = \hat{R}_{ij}\, \vec{v}_i + \vec{T}_{ij} \qquad (4\text{-}3)$$

Here, $\vec{v}_i$ and $\vec{v}_j$ are the vectors describing the coordinates of the previous and next joints, respectively.

All six parameters can be parameterized for the building blocks in the main-chain. These parameters describe the elements of main-chain flexibility as determined by the Amber94 force field. The probability distribution function for each parameter, shown in Figure 4-2, was found to be a Gaussian. Hence the potential function, V(x), based on Amber94 force field[119] for each model may be written as:

$$V(x) = k_x (x - x_0)^2 \qquad (4\text{-}4)$$

where x represents each mode of the potential function relative to the parameters, r_{ij}, α_i, β_i, g_i, $\beta\beta_i$, and $\gamma\gamma_i$. The terms k_x and x_0 are the force constant and the equilibrium value based on the parameter x, respectively. The total potential energy, U(x), is the sum of the individual modes, x_m, of each monomer unit, *i*, as shown in Equation (4-5).

$$U(x) = \sum_{i=1}^{n} \sum_{m=1}^{6} (k_{x_{m,i}} (x_{m,i} - x_{0_{m,i}})^2) \qquad (4\text{-}5)$$

where m is the number of the mode of the potential function, and i = 1, 2, .. , n, where n is the total number of the building block. The values of x_0 and k_x from MD are reported in Table 1.

The dynamics of the last monomer and the two spin-labels illustrated by MD are complicated and were not parameterized. The MD trajectory was performed on a dimer attached to two spin-labels. The possible locations of the last monomer with respect to the previous unit are stored in a table composed of 959 rows. Each row is composed of six parameters needed to transform the previous unit to the next one. The locations of the two spin-labels were carried out in the same way. Two tables contain 959 rows of the locations corresponding to the individual spin-labels.

- *Calculating Distance distribution function of the model, $P_{model}(r)$*

A conformational ensemble of the nanostructure is constructed in order to obtain the end-to-end distance distribution. The procedure used to build a trajectory is described as following: *first*, the values of parameters (r, α, β, γ, $\beta\beta$, $\gamma\gamma$) for each monomer unit were randomly generated. To produce a distance distribution that reflects the result from Amber94 simulations, each random number representing the value of each parameter is determined by the corresponding Gaussian distribution function denoted in Figure 4-2.

Therefore, the random number for each parameter is not generated from a uniform distribution, but from a Gaussian of the corresponding mean value (r_0, α_0, β_0, γ_0, $\beta\beta_0$, $\gamma\gamma_0$) with the standard deviation determined by the corresponding force constant (k_r, k_α, k_β, k_γ, $k_{\beta\beta}$, $k_{\gamma\gamma}$). This procedure for generating the 'pseudo-random' number is performed using the inversion or rejection method implemented in Matlab program. The parameters of the last building block and the spin-labels were randomly read off from the tables. *Second*, the location of each quaternary carbon center and the spin-labels are calculated by Equation (4-3) using the selected parameters. Each trajectory of the molecular chain was built by connecting the monomer segments and connecting the spin-labels at the ends. The distances between the spin-labels were calculated from the coordinates at the ends. *Finally,* the distance distribution, $P_{model}(r)$, was obtained from the histogram plot of the distances for 20,000 different trajectories. To ensure that result from 20,000 simulation steps converged, the calculation for 100,000 steps was performed and the result was comparable to that from 20,000 steps.

- *Refinement of the initial parameters*

The distance distributions, $P_{model}(r)$, obtained from the MD parameters are not comparable to those from ESR experiment. Therefore, the search for better parameters was performed by non-linear least square fitting with ESR data of all five oligomers. First, the distributions $P_{model}(r)$ are converted into theoretical DEER time-domain signals[126], $V_{model}(t)$, using Equation (4-6).

$$V_{model}(t) = \int_{r=r_1}^{r_2} \int_{\theta=0}^{\pi/2} P_{model}(r_{SL}) \left[\cos(\nu_{12})\, t)\right] \sin\theta d\theta dr \tag{4-6}$$

where $$\nu_{1,2} = \frac{\mu_0\, g_1\, g_2\, \beta^2\, (3\cos^2\theta - 1)}{4\pi\hbar\, r_{SL}^{\,3}} \tag{4-7}$$

Here, μ_0 is the vacuum permittivity, g_1 and g_2 are the isotropic g-factors of each electron, β is the Bohr magneton, $\hbar$ is Planck's constant, r_{SL} is the interspin vector between the two nitroxide at the ends, r_1 and r_2 is the minimum and maximum range of distance in the distance distribution of $P_{model}(r)$, θ is the angle between the interspin vector and the external magnetic field, and t is the time-domain axis.

The theoretical DEER time-domain signals, $V_{model}(t)$, of all five oligomers are compared to the corresponding DEER data, V(t), and a chi-square values, χ^2, was calculated as:

$$\chi^2 = \sum_{i=1}^{5} \frac{\sum_{k=1}^{N} (V_{model\,k,i}(t) - V_{exp\,k,i}(t))^2}{N-1} \tag{4-8}$$

where $k = 1, 2, \ldots N$, where N is the number of variable.

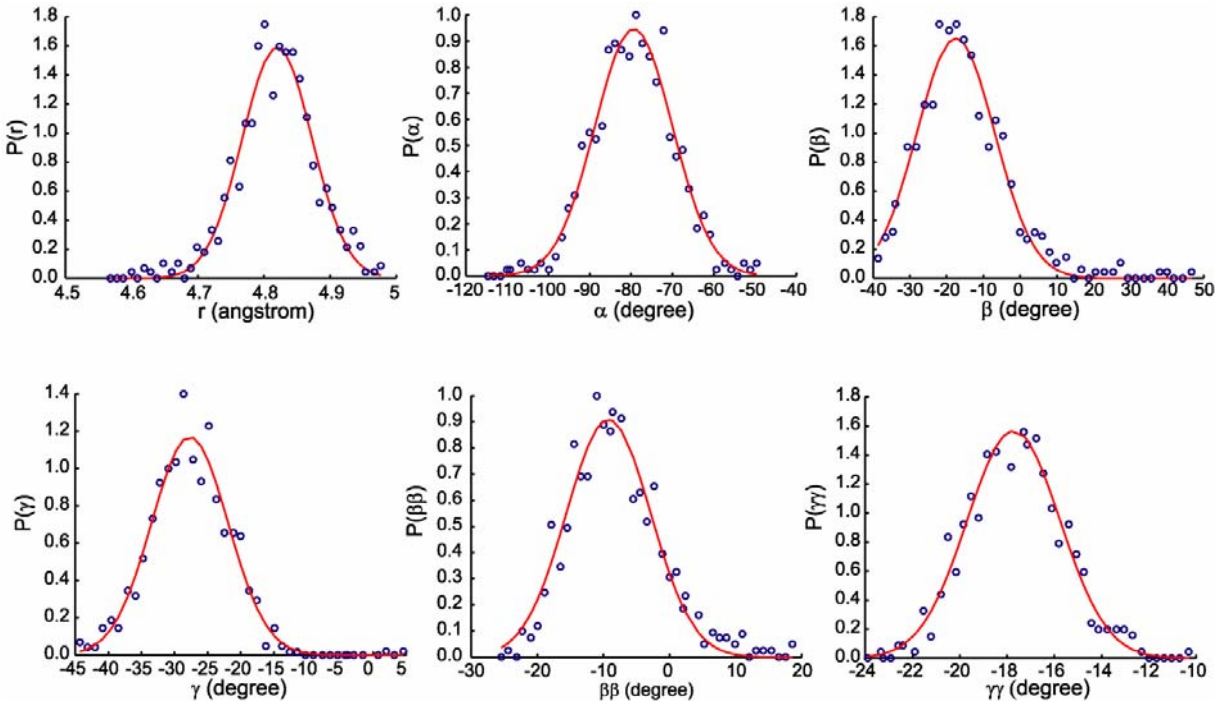

Figure 4-2: As a result of Amber94 simulation, the plots of the distribution functions (dotted line) as a function of six parameters, *i.e.,* the length of the stiff segment (r_{ij}), the angles between axes x_i and x_j (α), y_i and y_j (β), z_i and z_j (γ), x_i and xx_i ($\beta\beta$), and y_i and yy_i ($\gamma\gamma$), are shown. The functions fit with Gaussian distributions (solid lines) with the mean values for r = 4.82 Å, α = -79.32°, β = -17.53°, γ = -27.73°, $\beta\beta$ = -9.04°, and $\gamma\gamma$ = -17.75°, and the corresponding force constants k_r = 180.06 kcal/(mol·rad.^{2}), k_α = 18.01 kcal/(mol·rad.^{2}), k_β = 14.78 kcal/(mol·rad.^{2}), k_γ = 48.92 kcal/(mol·rad.^{2}), $k_{\beta\beta}$ = 40.56 kcal/(mol·rad.^{2}), and $k_{\gamma\gamma}$ = 425.62 kcal/(mol·rad.^{2}). These initial values of the parameters and the force fields show discrepant results when compared with the ESR data of the 6-8 oligomer *bis*-peptides. The optimum parameters representing the proper dynamics of the molecular rods are adjusted by non-linear least square fitting.

All procedures for the parameter optimization are carried out using a home-written Matlab program (The Mathworks, Inc.). The minimization of the non-linear least square fitting is performed using the Nelder-Mead simplex algorithm[148] as implemented in the Matlab program. The procedure of the fitting is concluded in the Scheme 1.

Details of the experimental and data analysis to obtain experimental distance distributions, $P_{exp}(r)$, are presented in Chapter3.

4.4 RESULTS AND DISCUSSION

The segment stiff model is used to construct the conformational structures of the *bis*-peptide oligomers. The objective of the model is to improve our ability to predict the overall shape and flexibility of an arbitrary sequence of the bis-peptide nanostructures based on this *bis*-amino acid. The model represents the position of each quaternary carbon center in the *bis*-peptide chain as a building block unit. A Cartesian coordinate is centered at each quaternary carbon (Figure 4-1a and 4-1b). The building blocks are connected by a relative segment vector r_{ij} where *i* and *j* are two adjacent building blocks. The spin-labels are modeled as additional vectors, $r_{1\text{-}SL1}$ and $r_{n\text{-}SL2}$, that connect the two spin-labels to the first and the last building blocks, respectively. The transformation from one coordinate to the next adjacent one requires six parameters as determined from Amber94 simulation and is described in the Methods section. The initial values of those parameters, obtained from MD are presented in Table 1. The corresponding force constants of those parameters, i.e., k_r, k_α, k_β, k_γ, $k_{\beta\beta}$, and $k_{\gamma\gamma}$, are reported as well.

Table 4-1: Parameters obtained from Amber94 for the transformation of monomer *i* to *j* in the backbone chain

Equilibrium value	r_0 [a]	α_0 [b]	β_0 [b]	γ_0 [b]	$\beta\beta_0$ [b]	$\gamma\gamma_0$ [b]
	4.82	-79.32	-17.53	-27.73	-9.04	-17.75
Force constant	k_r [c]	k_α [d]	k_β [d]	k_γ [d]	$k_{\beta\beta}$ [d]	$k_{\gamma\gamma}$ [d]
	180.06	18.011	14.78	48.93	40.56	425.62

a: Å
b: degree
c: kcal/(mol·Å^2)
d: kcal/(mol·rad^2)

The positions of the two spin-labels are computed to determine an end-to-end distance of a *bis*-peptide. The distance distribution $P_{model}(r)$ is determined using a simulation described in the Methods section and is converted to DEER signal, $V_{model}(t)$, using Equation (4-6). To test whether the parameters taken from Amber94 properly represent the main-chain conformation of the *bis*-peptide, we compared the distance distributions acquired from the experiment, $P_{exp}(r)$, with those from the model, $P_{model}(r)$. Initially, the $P_{model}(r)$ was calculated using the parameters taken from Amber94. The comparison of $P_{exp}(r)$ with $P_{model}(r)$ for the number of monomer unit, n, of 4 to 8 oligomers is shown in Figure 4-3. The $P_{model}(r)$ does not properly represent the experimental signals for longer oligomers. The model provides narrower distance distributions and longer most probable distances. Particularly, the model most severely misrepresents the DEER signal for n=8 oligomer. The failure of the prediction for longer oligomers was previously reported from our work.[144] In the earlier work, MD simulations of n=4 to 8 oligomers were obtained with Amber94 force field. The distance distributions from the MD overestimated the most probable interspin distance for long oligomers by ~ 2, 2.5 and 7 Å for n=6, 7, and 8, respectively.[144]

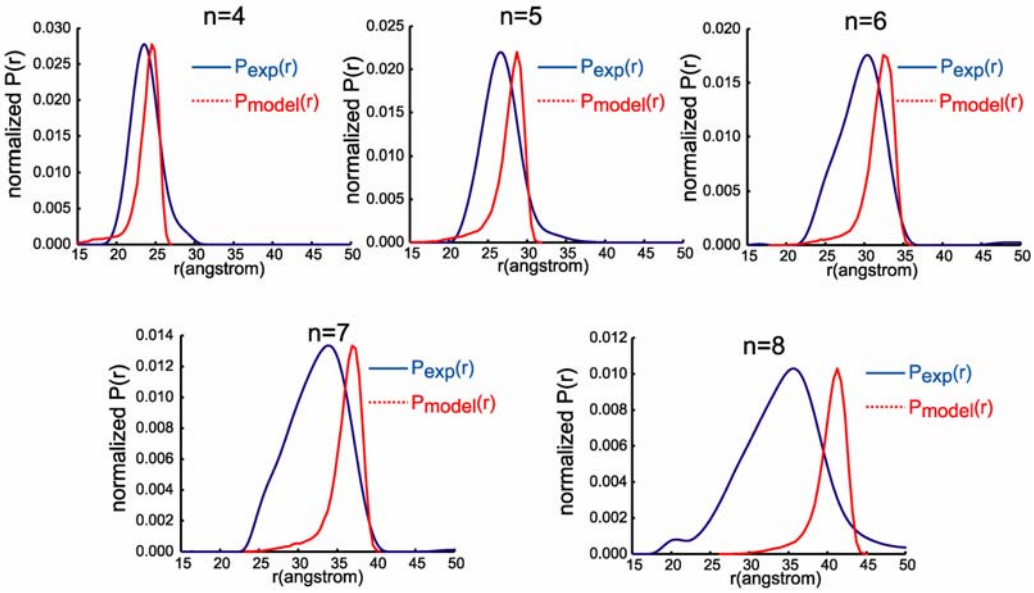

Figure 4-3: Distance distributions of n=4 to 8 oligomers from the joint stiff-segment model derived from Amber94 using the initial parameters (dashed lines), and from experiments (solid lines). The distributions from the initial parameters are narrower, and they overpredict the most probable distances for n=5, 6, 7, and 8 oligomers.

To search for the optimum parameters that properly represent the conformation of all *bis*-peptide structures, we performed simultaneous non-linear least square minimization for data from all five oligomers. The initial parameters were primarily used for the starting point of the non-linear least square (NLLS) fitting procedure.

There are, in principle, twelve adjustable variables, *i.e.*, the equilibrium values of r_0, α_0, β_0, γ_0, $\beta\beta_0$, $\gamma\gamma_0$, and their corresponding force constants, *i.e.*, k_r, k_α, k_β, k_γ, $k_{\beta\beta}$, and $k_{\gamma\gamma}$. However, there are only five experimental distribution functions. Each of these distribution functions in essence provides a mean distance, a standard deviation, and a skew parameter (the distribution functions are highly skewed). To obtain a reasonable fit, the number of variables for NLLS fitting needs to be reduced. Initially, all force constants were kept fixed and the six parameters of r_0, α_0, β_0, γ_0, $\beta\beta_0$, and $\gamma\gamma_0$ were varied. The results provide distributions of $P_{model}(r)$ that better fit to the most probable distances but were much narrower than the experimental distributions (results not shown). Therefore, it is necessary to vary the force constants during the NLLS procedure as well. After performing the fitting procedure with many different starting points, the parameters r_0 was changed by no more than 2%, and 10% for the angle α_0. The values for r_0 and α_0 predicted from MD were physically reasonable. The monomer length r_0 should be around 4.82 Å. The angle α_0 should be around -70° to -90° so that the fused five- and six- membered rings are not too constrained. These two parameters, therefore, were kept fixed. Similarly, changing the angles of β_0, γ_0, and $\alpha\alpha_0$ by less than 20% provides negligible changes of the distance distributions. On the other hand, the angle $\beta\beta_0$ has more influence on the distribution functions. For this reason, the parameters β_0, γ_0, and $\beta\beta_0$ were kept fixed while $\gamma\gamma_0$ was varied. Reducing the force constants of k_α, k_β, k_γ, and $k_{\beta\beta}$ to between 2 and 4 kcal/(mole·rad.^{2}) provides comparable widths of $P_{model}(r)$ to those of $P_{exp}(r)$. The force constants of k_r and $k_{\gamma\gamma}$ have no

influence in the change of distance distributions. The optimized parameters were obtained by varying the $\gamma\gamma_0$ angle and four force constants, *i.e.*, k_α, k_β, k_γ, and $k_{\beta\beta}$.

The optimized parameters and their starting values are reported in Table 4-2. The fonts in red indicate parameters that were varied. Figure 4-4 shows the results from the non-linear least square fitting. The fitting DEER signal of n=8 oligomer is shown in Figure 4-4f to demonstrate that the optimized parameters provide better fit of data than the initial parameters provided by MD. Figure 4-4a to 4-4e shows the trajectories of the bis-peptide oligomers calculated by the simulation described in the Methods section using the optimized parameters. The end-to-end distance distributions predicted from the joint-stiff segment model, $P_{model}(r)$, are shown together with the experimental distance distributions, $P_{exp}(r)$, which were determined by Tikhonov regularization method[74, 149] using DeerAnalysis program.[149] Previously, we reported the results from the same experimental DEER signals.[144]

The distribution functions compare well with the experimental results. The most probable distances predicted from $P_{exp}(r)$ and $P_{model}(r)$ are in good agreement for n=6-7 oligomers. For n=8 oligomer, the $P_{model}(r)$ shows longer most probable distance than $P_{exp}(r)$ by ~1 Å. These results are an improvement when compared to the results from MD simulation, which overestimated the most probable distances by ~ 2, 2.5, and 7 Å for n=6, 7, and 8 oligomers.[144]

The changes of the parameters imply that the force constants influence the flexibility and the distance distributions of the *bis*-peptide chains. The comparison between the optimized parameters and those obtained from MD indicates that the force constants of k_α, k_β, k_γ, and $k_{\beta\beta}$ predicted from MD are too high, leading to overly narrow distance distributions and extended mean distances.

Table 4-2: Comparison between initial and optimized parameters

Initial parameters[a]	r_0[c]	α_0[d]	β_0[d]	γ_0[d]	$\beta\beta_0$[d]	$\gamma\gamma_0$[d]
	4.82	-79.32	-17.53	-27.73	-9.04	-17.75
	k_r[e]	k_α[f]	k_β[f]	k_γ[f]	$k_{\beta\beta}$[f]	$k_{\gamma\gamma}$[f]
	180.06	18.011	14.78	48.93	40.56	425.62
Optimized parameters[b]	r_0[c]	α_0[d]	β_0[d]	γ_0[d]	$\beta\beta_0$[d]	$\gamma\gamma_0$[d]
	4.93	-77.23	-20.28	-6.27	-19.12	-21.06
	k_r[e]	k_α[f]	k_β[f]	k_γ[f]	$k_{\beta\beta}$[f]	$k_{\gamma\gamma}$[f]
	181.24	2.114	3.245	2.876	3.041	416.25

a. chi-square values: 0.0128 for n=4, 0.0339 for n=5, 0.1229 for n=6, 0.1505 for n=7, 0.3238 for n=8. The total chi-square = 0.644.

b. chi-square values: 0.0130 for n=4, 0.0037 for n=5, 0.0286 for n=6, 0.0392 for n=7, 0.0193 for n=8. The total chi-square = 0.1038.

c. Å.

d. degree.

e. kcal/(mol·Å^2).

f. kcal/(mol·rad^2).

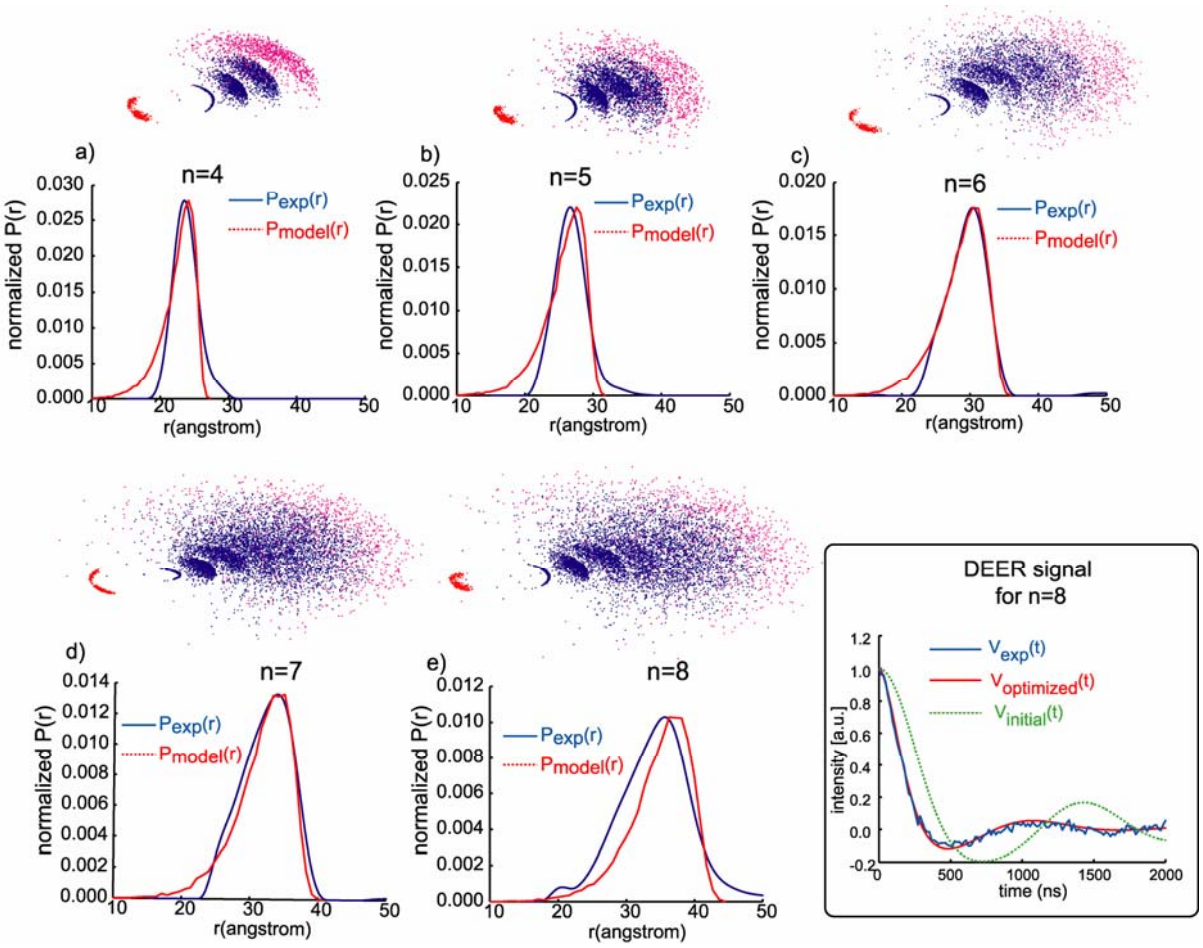

Figure 4-4: Trajectories for a) n=4; b) n=5; c) n=6; d) n=7; and e) n=8 oligomers. The blue dots represent the positions of quaternary carbon centers and the red dots represent the spin-labels at the ends for 2000 different trajectories. The position of the first quaternary carbon center is held fixed. The distance distributions of the model (dashed line) and experimental (solid line) are compared. The $P_{model}(r)$ distributions were calculated using the adjusted parameters with 20,000 simulation steps. The $P_{exp}(r)$ distributions were calculated from experimental data using Tikhonov regularization. The inset shows the DEER signals of the n=8 oligomer obtained from experiment (blue), from the model using initial parameters (dashed line), and from the model using optimized parameters (red line). The optimized parameters provide better fit to experimental signal than the initial parameters.

After the NLLS fitting, the optimized force constants were reduced by 10 times for k_α, 5 times for k_β, 24 times for k_γ, and 20 times for $k_{\beta\beta}$ when compared to the initial parameters. The equilibrium values of r_0, α_0, β_0, γ_0, $\beta\beta_0$, and $\gamma\gamma_0$ are similar to those guided by MD. The parameter that was varied, $\gamma\gamma_0$, was slightly increased by *c.a.* 3 degrees, *i.e.*, from -17.74° to -21.06°.

Some discrepancies between the $P_{model}(r)$ and $P_{exp}(r)$ remain. The $P_{model}(r)$ for n=4 and 5 oligomers shows a broader distribution towards shorter distances and have longer most probable distance than $P_{exp}(r)$ by ~1 Å for n=5 oligomer. The model predicts a range of distances from 12 to 27 Å for n=4, and 15 to 32 Å for n=5 as shown in Figure 4-4a and 4-4b, respectively. The lower distances less than 20 Å are mostly likely not sampled in the DEER experiments[46, 126] and the mean value of the distance distribution is altered to slightly shorter distances.

The dynamics of the chain can also be visualized from the model, i.e., the flexibility of the chain is increasing as the number of building block increases. For the longest oligomer (n=8) the broadening of $P_{model}(r)$ is the most deviated from the $P_{exp}(r)$. The deviation might be related to the error from the data processing using Tikhonov regularization.[149, 150] On the other hand, the error from the model fitting might be responsible to the narrow distance distributions. The fitting was simplified by reducing the variables from twelve to five parameters. Furthermore, the orientations of the two nitroxides were not parameterized which might lead to some uncertainty in predicting the distance distributions.

4.5 SUMMARY

In conclusion, we demonstrate an approach for the analysis of the flexibility of the *bis*-peptide nanorods using the joint-stiff segment model. The model provides improved parameters for the MD simulations of *bis*-peptides. There are limited force fields that properly simulate the dynamics and conformations of conformationally restricted nanostructures. Amber94 force field is an established force field widely used for proteins and organic molecules,[151] which is a good candidate for the simulation of nanomaterials. Our results, however, showed that Amber94 does not properly represent the conformations of the *bis*-peptide nanorods for long oligomers. We can obtain the optimized parameters by varying five variables, *i.e.*, the angle $\gamma\gamma_0$, and five force constants of k_α, k_β, k_γ, and $k_{\beta\beta}$. The parameters obtained from the model provide better fit than the MD parameters. The parameters between two adjacent monomers are 4.82 Å for r_0, -79.3° for α_0, -17.52° for β_0, and -9.04° for γ_0, -27.73° for $\beta\beta_0$, and -21.06° for $\gamma\gamma_0$. The flexibility of the main chain is influenced by the force constants of k_r=180.06 kcal/(mol.Å^2), k_α=2.114 kcal/(mol.rad^2), k_β=3.245 kcal/(mol.rad^2), k_γ=2.876 kcal/(mol.rad^2), $k_{\beta\beta}$=3.041 kcal/(mol.rad^2), and $k_{\gamma\gamma}$=425.25 kcal/(mol.rad^2). Among these parameters, $\gamma\gamma_0$, k_α, k_β, k_γ, $k_{\beta\beta}$ were varied. The *bis*-peptide materials can be synthesized in different shapes by controlling the stereoisomer of the chiral Carbon centers.[123] The improved parameters provided by the joint-stiff segment model will aid in the designs of functional nanostructures with well-defined structure. The overall shapes and flexibility of an oligomer composed of an arbitrary number of these monomers can now be calculated in minutes.

4.6 ACKNOWLEDGEMENT

This research was supported by a NSF CAREER Award (MCB0346898).

APPENDIX A

PHASE CYCLE

Table A-1: General phase cycle for the COSY experiment

φ1	φ2	A1	B1	A2	B2
+x	+x	+a	+b	0	0
-x	+x	-a	-b	0	0
+y	+x	0	0	-a	-b
-y	+x	0	0	+a	+b

Tabel A-1 presents the normal phase cycle used for COSY experiment. The phase's φ_1 and φ_2 are the phases of the first and second pulses, respectively, and A1, B1, A2, and B2 are the memory addresses. The first two steps provide the real component in t_1 and the second two provide the imaginary component in t_1. This basic four-step phase cycle then gives the full hypercomplex 2D data set from which the S_{c-} signal may be extracted. To this basic phase cycle the four-step CYCLOPS sequence is added, making it a 16 step phase cycle. For each step of the phase cycle the signal is averaged and then the phases of the pulses changed for the next step of

the phase cycle. By implementing CYCLOPS as shown in Table A-2 fast temporal cancellation of some of the dead-time artifacts can be achieved.

Table A-2: Modified phase cycle of COSY experiment for reducing dead-time artifacts

φ1	φ2	A1	B1	A2	B2
+x	+x	+a	+b	0	0
-x	+x	-a	-b	0	0
+y	+y	+b	-a	0	0
-y	+y	-b	+a	0	0
-x	-x	-a	-b	0	0
+x	-x	+a	+b	0	0
-y	-y	-b	+a	0	0
+y	-y	+b	-a	0	0
+y	+x	0	0	-a	-b
-y	+x	0	0	+a	+b
-x	+y	0	0	-b	+a
+x	+y	0	0	+b	-a
-y	-x	0	0	+a	+b
+y	-x	0	0	-a	-b
+x	-y	0	0	+b	-a
-x	-y	0	0	-b	+a

APPENDIX B

DEER-ESR DATA PROCESSING

B.1 BACKGROUND CORRECTION

B.1.1 Functional form fitting

$V_{inter}(t)$ can be determined by applying a functional form that fits to the last part of V(t), generally around the last two-third of the signal. A theory suggests that the intermolecular interaction between electron spins can be in presented as a *stretch exponential*, which is normally used for the background fitting, and is in the form of[152]

$$V_{inter}(t) = \exp(-\kappa t^{\alpha}) \qquad \text{(B-1)}$$

which is equivalent to

$$\ln[-\ln(V(t))] = \ln(\kappa) + \alpha \ln(t) \qquad \text{(B-2)}$$

κ is a constant. According to the cited references[61, 152, 153], α is a distinctive feature for the 3D, 2D, or 1D distribution of spins in the system under investigation. In most cases of diluted samples in solution, the confinement of electron spins is 3D distribution, and α is equal to 1. For 2D distribution, $\alpha = 2/3$, and for 1D distribution, $\alpha = 1/3$.

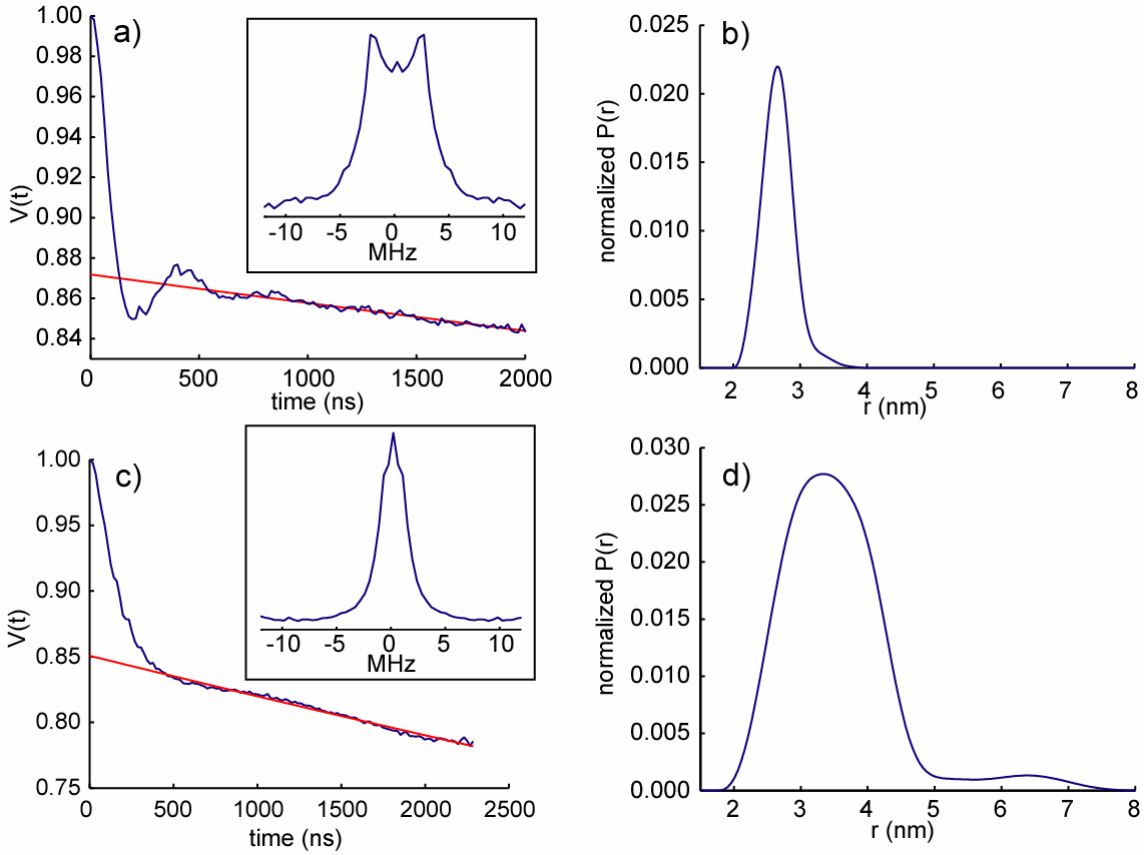

Figure B-1: DEER signal (blue) and baseline fitting function (red) of a) 5-mer bis-peptide and c) flexible 7-mer bis-peptide. The corresponding distance distribution of a) and c) is shown in b) and d), respectively. The insets show the Fourier Transform of the time-domain data after baseline subtraction. The comparison of these two cases emphasizes the influence of intermolecular interaction to the distance distribution. a) the intermolecular interaction is effectively removed. The other case where the intermolecular interaction is not completely removed is shown in c).

This method is efficient when the distance distribution is narrow and is dominated by distances shorter than 4 nm[154] as shown in Figure B-1a. The data is obtained from a relatively rigid five-mer *bis*-peptide. The $V_{inter}(t)$ in Figure B-1a fits with κ=0.054, and α=1. The distance distribution shows mean distance of 2.6 nm and standard deviation of 0.2 nm. In contrast, the analysis becomes more challenging for the system of flexible molecules that display broad distance distributions, and/or longer distance than 4 nm (between 4 and 6 nm). The data in this case is shown in Figure B-1c, which is obtained from a flexible seven-mer bis-peptide. The signal in Figure B-1c demonstrates the influence of the intermolecular interaction on the modulation depth of the signal. The concentration of the sample in both cases (Figure B-1a and B-1c) is 0.2 mM in aqueous buffer solution. However, the molecule in Figure B-1a is shorter and more rigid. The intermolecular interaction only contributes to the decay for the last two-third of the signal, and can be subtracted out by fitting the last part of V(t) with the exponential functional form. On the other hand, for the flexible 7-mer bis-peptide, the intermolecular interaction not only contributes to the decay at the latter part of the signal, but also to lower the modulation depth, due to the broader distance distribution. It is clear in Figure B-2a that at a lower concentration (0.1 mM) the modulation is more distinguished for the first 600 ns of the signal. It can be concluded that the broader distribution at higher concentration is partly due to the intermolecular interaction. In this situation, one can use the data from both concentrations to subtract the intermolecular contribution, which is discussed in the next section.

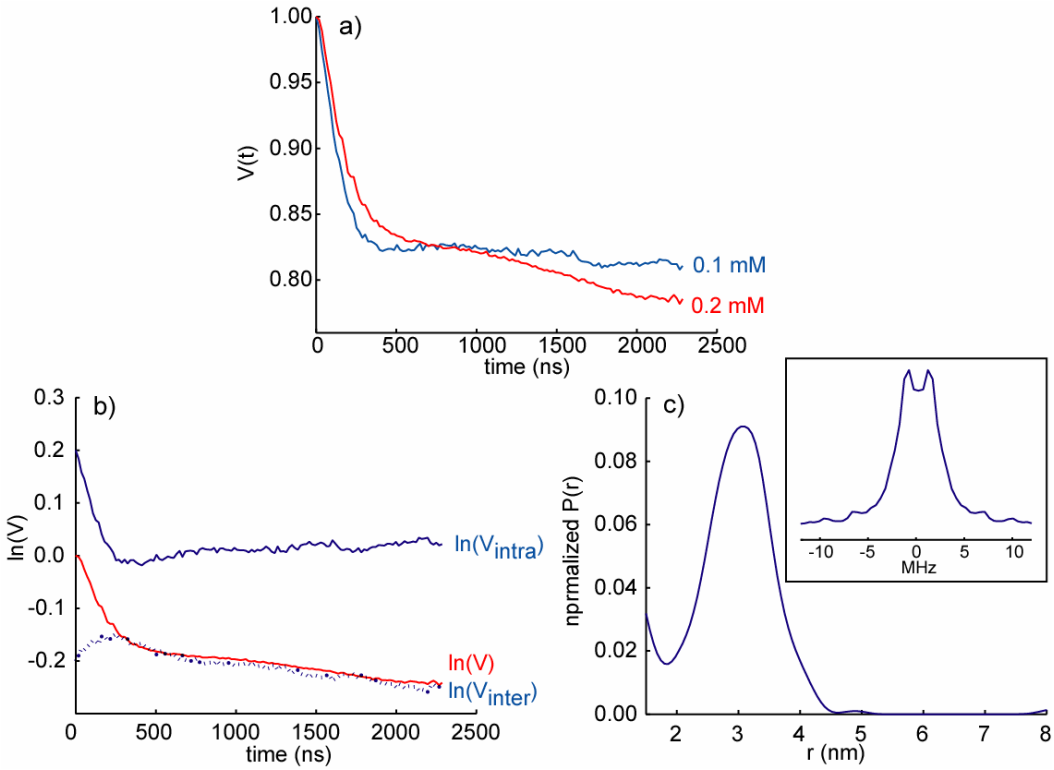

Figure B-2: Procedure of Baseline subtraction for a flexible 7-mer bis-peptide (see text). a) DEER signal of 0.1 mM (blue) and 0.2 mM (red) of flexible 7-mer bis-peptide, b) the signal in natural logarithmic scale showing $V_{inter}(t)$ in dotted line, $V_{intra}(t)$ in blue, and the DEER signal V(t) in red, c) distance distribution of $V_{inter}(t)$. The inset shows Fourier Transform after baseline subtraction. The spectrum indicates distinct frequency at 90° of pake pattern.

B.1.2 Experimental fitting

The experimental signal, V(t), is described as the multiplication between $V_{inter}(t)$ and $V_{intra}(t)$. The $V_{inter}(t)$ contribution is concentration dependent, and can be written as [139, 152, 155]

$$V_{inter}(t) = \exp[-C\, f(t)] \qquad \text{(B-3)}$$

where C is the concentration of spin labels and f(t) is an arbitrary function depending on the time, t. If the DEER signals are obtained from two different concentrations, i.e., C_1 and C_2, assuming that the $V_{intra}(t)$ from both concentrations are identical since they represent the interspin distance from the same molecular structure, the function f(t) can be determined using Equation (B-4)

$$\ln(V_2) - \ln(V_1) = (C_1 - C_2)\, f(t) \qquad \text{(B-4)}$$

where V_1 and V_2 are the experimental V(t) obtained for the concentrations C_1 and C_2, respectively. Figure B-2 represents the processing of the same V(t) signal shown in Figure B-1c. The additional data of more diluted V(t) was acquired. The separation of $V_{inter}(t)$ and $V_{intra}(t)$ was performed using Equation B-4. The $V_{intra}(t)$ is obtained as $\ln(V) - \lambda \ln(V_{inter})$, where λ is adjusted so that, at the last two-third of the signal, the coincidence of $d[\ln(V)]/dt$ and $d[\lambda \ln(V_{inter})]/dt$ is met. This step is performed to decrease the effect of the uncertainty in concentration, i.e., C_1 and C_2.

The result obtained from this approach is more convincing than that shown in Figure B-1c. The Fourier Transform of the $V_{intra}(t)$ shown in the inset indicates a distinct frequency at 90° of 'pake pattern', whereas that in Figure B-1c shows a spike at zero frequency indicating that the baseline subtraction is not sufficient.

B.2 LIMITING VALUE OF $V_{INTRA}(T)$: V_P

A DEER experiment is used for distance measurement between two electron spins in the range of 1.5 to 8.0 nm. It is also useful in the determination of number of clusters in peptide complexes[139, 152, 155-157]. Recently, Prisner el al[115] demonstrated the use of DEER to calculate the number of spin-labels in samples with well-defined geometry. The nanostructure of bis-peptide oligomers in this research also provides valuable DEER data that can be used to calibrate the number of the spin labels in a sample of unknown spin number.

The $V_{intra}(t)$ represents the electron dipole interaction, which is obtained by baseline subtraction of V(t). The general feature of $V_{intra}(t)$ oscillates at the frequency corresponding to inverse of intramolecular distance at short time t, and decays to a limiting value (V_p) at the end. The V_p value depends on the number of spin labels, and the probability of spin flip induced by the pumping pulse (p_b). For a simple case of identical groups of N number of spin labels[157]

$$V_p \sim 1-(N-1)p_b \qquad \text{(B-5)}$$

Figure B-3a shows $V_{intra}(t)$ for bis-peptide oligomer of 4-8 monomers performed on MS2 resonator. In this case, N is 2, and V_p is read off from the $V_{intra}(t)$ plot which is ~0.93. The parameter p_b is calculated using Equation (B-5), and is equal to 0.07. The parameter p_b depends on the excitation profile of the pumping pulse, and should remain the same for the same pulse length. In this case, around 7% of the spin is excited by 48 ns pumping pulse equipped with MS2 resonator. In Figure B-3b, the experiment was performed on MS3 resonator, and the p_b value is different from the previous case due to the different excitation profile of the resonators. The V_p is ~0.88 for MS3 resonator providing the p_b of 0.12. This p_b value indicates that ~12% of the spin is excited.

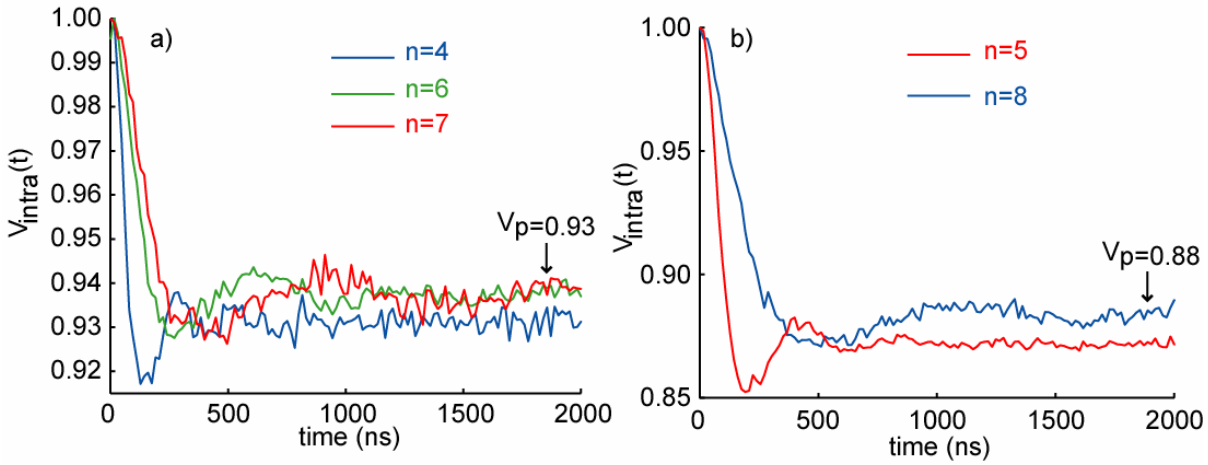

Figure B-3: DEER data showing the V_p values for 48 ns pumping pulse of a) bis-peptide oligomers of n=4 (blue), 6 (green), and 7 (red) performed on MS2 resonator, and b) n=5 (red) and 8 (blue) oligomers performed on MS3 resonator.

Table A-1 provides the p_b values at different experimental conditions. Note that the p_b parameter depends on the type of resonator (MS2 or MS3), and does not vary much with the length of pumping pulse.

The samples with unknown number of spin-labels can be determined by performing the same experimental condition.

Table B-1: Values of p_b acquired at different type of resonators and pulse lengths

Pumping pulse length (ns)	Type of resonator	p_b	% spin excited
32	MS2	0.07	7
32	MS3	0.13	13
32	MS2	0.07	7
48	MS2	0.07	7
48	MS2	0.07	7
48	MS3	0.12	12

BIBLIOGRAPHY

1. Zavoiski, E., *J. Phys. USSR* **1945,** 9, 211.

2. Berliner, L. J., *Spin labeling: theory and applications*. Academic Press: New York, 1976; p 592.

3. Faulhammer, H. G.; Denniger, G.; Hartl, P. J.; Azhayev, A. V.; Schwoerer, M.; Sprinzl, M., Spin-labelled analogues of GDP and GTP as site-specific reporter group for guanosine nucleotide-binding proteins. *Biochimica et Biophysica Acta* **1986,** 884, (1), 182-190.

4. McConnell, H. M.; Hubbell, W. L., Molecular motion in spin-labeled phospholipids and membranes. *Journal of the American Chemical Society* **1971,** 93, 314-326.

5. Berliner, L. J.; Grunwald, J.; Hankovszky, H. O.; Hideg, K., A novel reversible thiol-specific spin label: papain active site labeling and inhibition. *Analytical Biochemistry* **1982,** 119, 450-455.

6. Graceffa, P., Spin labeling of protein sulfhydryl groups by spin trapping a sulfur radical: application to bovine serum albumin and myosin. *Archives of Biochemistry and Biophysics* **1983,** 225, 802-808.

7. Manosa, J.; Palau, J.; Lawrence, J. J., Association-dissociation of histone oligomers. A spin label study. *International Journal of Peptide & Protein Research* **1984,** 24, 533-542.

8. Zeidan, H. M.; Pearson, K. H.; Brown, S. G.; Han, P. F., Microenvironment around the essential cysteine residues in chicken liver fructose-1,6-bisphosphatase as analyzed by ESR spin labeling. *Biochimica et Biophysica Acta, Protein Structure and Molecular Enzymology* **1986,** 870, 141-147.

9. Nakayama, S.; Watanabe, T.; Takahashi, K.; Hoshino, M.; Yoshida, M., Comparative study on the active sites of ficin and papain by the spin labeling method. *Journal of Biochemistry (Tokyo, Japan)* **1987,** 102, 531-535.

10. Zhao, B.; Musci, G.; Sugawara, Y.; Berliner, L. J., Spin-label and fluorescence labeling studies of the thioester bonds in human α2-macroglobulin. *Biochemistry* **1988,** 27, 5304-5308.

11. Todd, A. P.; Cong, J.; Levinthal, F.; Levinthal, C.; Hubbell, W. L., Site-directed mutagenesis of colicin E1 provides specific attachment sits for spin labels whose spectra are sensitive to local conformation. *Protein: Structure, Function, and Genetics* **1989,** 6, 294-305.

12. Hubbell, W. L.; Gross, A.; Lagen, R.; Lietzow, M. A., Recent advances in site-directed spin labeling of proteins. *Current Opinion in Structural Biology* **1998,** 8, 649-656.

13. Hubbell, W. L.; Cafiso, D. S.; Altenbach, C., Identifying conformation changes with site-directed spin labeling *Nature Structural Biology* **2000,** 7, 735-739.

14. Hubbell;, W. L.; Altenbach, C., Investigation of structure and dynamics in membrane proteins using site-directed spin labeling. *Current Opinion in Structural Biology* **1994,** 4, 566-573.

15. Hubbell;, W. L.; Mchaourab;, H. S.; Altenbach;, C.; Leitzow, M. A., Watching proteins move using site-directed spin labeling. *Structure* **1996,** 4, 779-783.

16. Fajer, P. G., Site directed spin lebelling and pulsed dipolar electron paramagnetic resonance (double electron-electron resonance) of force activation in muscle. *Journal of Physics: Condensed Matter* **2005,** 17, S1459-S1469.

17. Schneider, D. J.; Freed, J. H., *Calculating slow motional magnetic resonance spectra: A user's guide*. Plenum Publishing Corporation: 1989; Vol. 8.

18. Schrieir, S.; Polnaszek, C. F.; Smith, I. C. P., Spin labels in membrans: Problems in practice. *Biochimica et Biophysica Acta, Reviews on Biomembranes* **1978,** 515, (375-436).

19. Griffith, O. H.; Dehlinger, P. J.; Van, S. P., Shape of the hydrophobic barrier of phospholipid bilayers (evidence for water penetration in biological membranes). *Journal of Membrane Biology* **1974,** 15, 159-192.

20. Kivelson, D., Theory of ESR linewidths of free radicals. *Journal of Chemical Physics* **1960,** 33, 1094-1106.

21. Schweiger, A.; Jeschke, G., *Principles of pulse electron paramagnetic resonance*. Oxford University Press: 2001; p 578.

22. Mchaourab, H. S.; Lietzow, M. A.; Hideg, K.; Hubbell, W. L., Motion of spin-labeled side chains in T4 lysozyme. Correlation with protein structure and dynamics. *Biochemistry* **1996,** 35, (24), 7692-7704.

23. Hubbell, W. L.; Mchaourab, H. S.; Altenbach, C.; Leitzow, M. A., Watching proteins move using site-directed spin labeling. *Structure* **1996,** 4, 779-783.

24. Farahbakhsh, Z.; Altenbach, C.; Hubbell, W. L., Spin labeled cysteines as sensors for protein-lipid interaction and conformation in rhodopsin. *Photochemistry and Photobiology* **1992,** 56, 1019-1033.

25. Altenbach, C.; Yang, K.; Farrens, D.; Khorana, H. G.; Hubbell, W. L., Structural features and light-dependent changes in the cytoplasmic interhelical E-F loop region of rhodopsin: a site-directed spin labeling study. *Biochemistry* **1996,** 35, (38), 12470-12478.

26. Voss, J.; He, M.; Hubbell, W. L.; Kaback, H. R., Site-directed spin labeling demonstrates that transmembrane XII in the lactose permease of *Escherichia coli* is an α-helix. *Biochemistry* **1996,** 35, (39), 12915-12918.

27. Oh, K. J.; Zhan, H.; Cui, C.; Hideg, K.; Collier, R. J.; Hubbell, W. L., Membrane conformation of the isolated transmembrane domain of diptheria toxin: a site directed spin labeling study. *Biophysical Journal* **1996,** 70, 140.

28. Morin, B.; Bourhis, J.-m.; Belle, V.; Woudstra, M.; Carriere, F.; Guigliarelli, B.; Fournel, A.; Longhe, S., Assessing induced folding of an intrinsically disordered protein by site-directed spin-labeling electron paramagnetic resonance spectroscopy. *Journal of Physical Chemistry B* **2006,** 110, (20596-20608).

29. Lagerstedt, J. O.; Budamagunta, M. S.; Oda, M. N.; voss, J. C., Electron paramagnetic resonance spectroscopy of site-directed spin labels reveals the structural heterogeneity in the N-terminal domain of ApoA-I in solution. *Journal of Biological Chemistry* **2007,** 282, (12), 9143-9149.

30. Qu, K.; Vaughn, J. L.; Sienkiewicz, A.; Scholes, C. P.; Fetrow, J. S., Kinetics and motional dynamics of spin-labeled yeast iso-1-cytochrome c. 1. Stopped-flow electron paramagnetic resonance as a probe for folding/unfolding of the C-terminal helix spin-labeled at cysteine. *Biochemistry* **1997,** 102, 2884-2897.

31. Rink, T.; Riesle, J.; Oesterhelt, D.; Gerwert, K.; Steinhoff, H. J., Spin-labeling studies of the conformational changes in the vicinity of D36, D38, T46 and E161. *Biophysical Journal* **1997,** 73, 983-993.

32. McConnell, H. M., Indirect hyperfine interactions in the paramagnetic resonance spectra of aromatic free radicals. *Journal of Chemical Physics* **1956,** 24, 764-767.

33. Atherton, N. M., *Principles of electron spin resonance*. Ellis Horwood and Prentice Hall: 1993.

34. Carrington, A.; McLachlan, A. D., *Introduction to magnetic resonance with applications to chemistry and chemical physics*. Haper International Edition.

35. Abragam, A., *Principles of nuclear magnetism*. Clarendon: Oxford, 1961.

36. Slichter, C. P., *Principles of magnetic resonance*. 3 ed.; Springer: Berlin, 1996.

37. Schneider, D. J.; Freed, J. H., Spin relaxation and motional dynamics. *Advances in Chemical Physics* **1989,** 73, 387-527.

38. Budil, D. E.; Lee, S.; Saxena, S.; Freed, J. H., Nonlinear-least-squares analysis of slow-motion EPR spectra in one and two dimensions using a modified Levenberg-Marquardt algorithm. *Journal of Magnetic Resonance, Series A* **1996,** 120, 155-189.

39. Patyal, B. R.; Crepeau, R. H.; Gamliel, D.; Freed, J. H., Two-dimensional Fourier-transform ESR in the slow-motional and rigid limits: SECSY-ESR. *Chemical Physics Letters* **1990,** 175, 445-452.

40. Lee, S.; Budil, D. E.; Freed, J. H., Theory of two-dimensional Fourier transform electron spin resonance for ordered and viscous fluids. *Journal of Chemical Physics* **1994,** 101, 5529-5558.

41. Gorcester, J.; Freed, J. H., Two-dimensional Fourier transform ESR correlation spectroscopy. *Journal of Chemical Physics* **1988,** 88, 4678-4693.

42. Millhauser, G. L.; Freed, J. H., Two-dimensional electron spin echo spectroscopy and slow motions. *Journal of Chemical Physics* **1984,** 81, 37-48.

43. Freed, J. H., Theory of slow tumbling ESR spectra for nitroxides. In *Spin labeling: Theory and applications*, Berliner, L. J., Ed. Academic Press: New York, 1976; Vol. I, pp 53-132.

44. Fiori, W. R.; Miick, S. M.; Millhauser, G. L., Increasing sequence length favors α-helix over 3_{10}-helix in alanine-based peptide: Evidence for a length-dependent structural transition. *Biochemistry* **1993,** 32, 11957-11962.

45. Eaton, S. S.; More, K. M.; Swant, B. M.; Eaton, G. R., Use of the EPR half-field transition to determine the interspin distance and the orientation of the interspin vector in systems with two unpaired electrons. *Journal of the American Chemical Society* **1983,** 105, 6560-6567.

46. Larsen, R. G.; Singel, D. J., Double electron-electron resonance spin-echo modulation: Spectroscopic measurement of electron spin pair separations in orientationally disordered solids. *Journal of Chemical Physics* **1993,** 98, (7), 5134-5146.

47. Mims, W. B., Some applications of pulse techniques in EPR. *Applied Magnetic REsonance* **1991,** 2, 595-609.

48. Berliner, L. J.; Eaton, G. R.; Eaton, S. S., *Distance measurements in biological systems by EPR*. Kluwer/Plenum Publication: New York, 2000; Vol. 19, p 614.

49. Manjasetty, B. A.; Turnbull, A.; Bussow, K.; Chance, M. R., Recent advances in protein structure analysis. *Recent Research Developments in Biochemistry* **2006,** 7, 47-71.

50. Wuthrich, K., *NMR of proteins and nucleic acids*. Wiley: New York, 1986.

51. Stryer, L., Fluorescence energy transfer as a spectroscopic ruler. *Annual Review of Biochemistry* **1978,** 47, 819-846.

52. Schuler, B.; Lipman, E. A.; Steinbach, P. J.; Kumke, M.; Eaton, W. A., Polyproline and the "spectroscopic ruler" revisited with single-molecule fluorescence. *Proceedings of the National Academy of Science of the United States of America* **2005,** 102, (8), 2754-2759.

53. Eaton, S. S.; Eaton, G. R., Measurement of spin-spin distances from the intensity of the EPR half-field transition. *Journal of the American Chemical Society* **1982,** 104, 5002-5003.

54. Rabenstein, M. D.; Shin, Y.-K., Determination of the distance between two spin labels attached to a macromolecule. *Proceedings of the National Academy of Sciences of the United States of America* **1995,** 92, 17610-17614.

55. Xiao, W.; Shin, Y.-K., EPR spectroscopic ruler: The method and its applications. In *Distance Measurements in Biological Systems by EPR*, Kluwer Academic/Plenum Publishers: 2000; pp 249-276.

56. Kornilova, A. Y.; Wishart, J. F.; Xiao, W.; Lasey, R. C.; Fedorova, A.; Shin, Y.-K.; Ogawa, M. Y., Design and Characterization of A Synthetic Electron-Transfer Protein. *Journal of the American Chemical Society* **2000,** 122, 7999-8006.

57. Altenbach, C.; Oh, K.-J.; Trabanino, R. J.; Hideg, K.; Hubbell, W. L., Estimation of inter-residue distances in spin labeled proteins at physiological temperatures: Experimental strategies and practical limitations. *Biochemistry* **2001,** 40, 15471-15482.

58. Mchaourab, H. S.; Oh, K. J.; Fang, C. J.; Hubbell, W. L., Conformation of T4 Lysozyme in solution. Hinge-bending motion and the substrate-induced conformational transition studied by sited-directed spin labeling. *Biochemistry* **1997,** 36, 307-316.

59. Sangmi, J.; Becker, J. S.; Yonkunas, M.; Coalson, R.; Saxena, S., Unfolding of alanine-based peptides using electron spin resonance distance measurements. *Biochemistry* **2006,** 45, (38), 11666-11673.

60. Prisner, T.; Rohrer, M.; MacMillan, F., Pulsed EPR spectroscopy: Biological applications. *Annual Review of Physical Chemistry* **2001,** 52, 279-313.

61. Milov, A. D.; Maryasov, A. G.; Tsvetkov, Y. D., Pulsed electron double resonance (PELDOR) and its applications in free-radicals research *Applied Magnetic Resonance* **1998,** 15, (1), 107-143.

62. Jeschke, G., Distance measurements in the nanometer range by pulse EPR. *ChemPhysChem* **2002,** 3, 927-932.

63. Saxena, S.; Freed, J. H., Double quantum two-dimensional Fourier Transform electron spin resonance: distance measurements. *Chemical Physcis Letters* **1996,** 251, (1,2), 102-110.

64. Saxena, S.; Freed, J. H., Theory of double quantum two-dimensional electron spin resonance with application to distance measurements. *Journal of Chemical Physics* **1997,** 107, (5), 1317-1340.

65. Borbat, P. P.; Freed, J. H., Multiple-quantum ESR and distance measurements. *Chemical Physcis Letters* **1999,** 313, 145-154.

66. Borbat, P.; Mchaourab, H. S.; Freed, J. H., Protein structure determination using long-distance constraints from double-quantum coherence ESR: Study of T4 Lysozyme
Journal of the American Chemical Society **2002,** 124, (19), 5304-5314.

67. Pannier, M.; Veit, S.; Godt, A.; Jeschke, G.; Spiess, H. W., Dead-Time free measurement of dipole-dipole interactions between electron spins. *Journal of Magnetic Resonance* **2000,** 142, (2), 331-340.

68. Eaton, S. S.; Eaton, G. R., Measurements of interspin distances by EPR. *Electron Paramagnetic Resonance* **2004,** 19, 318-337.

69. Bowman, M. K.; Maryasov, A. G.; Kim, N.; DeRose, V. J., Visualization of distance distribution from pulsed double electron-electron resonance data *Applied Magnetic Resonance* **2004,** 26, (1-2), 23-39.

70. Pake, G. E., Nuclear resonance absorption in hydrated crystals: fine structure of the proton line. *Journal of Chemical Physics* **1948,** 16, 327.

71. Jeschke, G.; Panek, G.; Godt, A.; Bender, A.; Paulsen, H., Data analysis procedures for pulse ELDOR measurements of broad distance distributions *Applied Magnetic Resonance* **2004,** 26, (1-2), 223-244.

72. Chiang, Y.-W.; Borbat, P. P.; Freed, J. H., The determination of pair distance distributions by pulsed ESR using Tikhonov regularization. *Journal of Magnetic Resonance* **2005,** 172, 279-295.

73. Jeschke, G.; Koch, A.; Jonas, U.; Godt, A., Direct conversion of EPR dipolar time evolution data to distance distributions. *Journal of Magnetic Resonance* **2001,** 155, 72-82.

74. Tikhonov, A. N.; Arsenin, V. Y., *Solutions of ill-posed problems*. Wiley: New York, 1977.

75. Chiang, Y.-W.; Borbat, P. P.; Freed, J. H., Maximum entropy: A complement to Tikhonov regularization for determination of pair distance distributions by pulsed ESR. *Journal of Magnetic Resonance* **2005,** 177, 184-196.

76. Jeschke, G.; Chechik, V.; Ionita, P.; Godt, A.; Zimmermann, H.; Banham, J.; Timmel, C. R.; Hilger, D.; Jung, H., DeerAnalysis2006 - a comprehensive software package for analyzing pulsed ELDOR data. *Applied Magnetic Resonance* **2006,** 30, (3-4), 473-498.

77. *The program is freely available at www.mpip-mainz.mpg.de/~jeschke/distance.html*.

78. Miick, S. M.; Millhauser, G. L., Measuring Heisenberg spin exchange between spin-labeled peptides with 2D ELDOR. *Journal of Magnetic Resonance, Series B* **1994,** 104, 81-84.

79. Milov, A. D.; Tsvetkov, Y. D.; Formaggio, F.; Crisma, M.; Toniolo, C.; Raap, J., Self-assembling properties of membrane-modifying peptides studied by PELDOR and CW-ESR spectroscopies. *Journal of the American Chemical Society* **2000,** 122, (16), 3843-3848.

80. Borbat, P. P.; Costa-Filho, A. J.; Earle, K. A.; Moscicki, J. K.; Freed, J. H., Electron spin resonance in studies of membranes and proteins. *Science* **2001,** 291, 266-269.

81. Crepeau, R. H.; Saxena, S.; Lee, S.; Patyal, B.; Freed, J. H., Studies on lipid membranes by two-dimensional Fourier transform ESR: enhancement of resolution to ordering and dynamics. *Biophysical Journal* **1994,** 66, 1489-1504.

82. Patyal, B. R.; Crepeau, R. H.; Freed, J. H., Lipid-gramicidin interactions using two-dimensional Forier-transform electron spin resonance. *Biophysical Journal* **1997,** 73, 2201-2220.

83. Costa-Filho, A. J.; Shimoyama, Y.; Freed, J. H., A 2D-ELDOR study of the liquid ordered phase in multilamellar vesicle membranes. *Biophysical Journal* **2003,** 84, 2619-2633.

84. Milov, A. D.; Maryasov, A. G.; Tsvetkov, Y. D.; Raap, J., Pulsed ELDOR in spin-labeled polypeptides *Chemical Physics Letters* **1999,** 303, (1-2), 135-143.

85. Jeschke, G.; Pannier, M.; Godt, A.; Spiess, H. W., Dipolar spectroscopy and spin alignment in electron paramagnetic resonance. *Chemical Physics Letters* **2000,** 331(2,3,4), 243-252.

86. Pannier, M.; Schaedler, V.; Schoeps, M.; Wiesner, U.; Jeschke, G.; Spiess, H. W., Determination of Ion Cluster Sizes and Cluster-to-Cluster Distances in Ionomers by Four-Pulse Double Electron Electron Resonance Spectroscopy. *Macromolecules* **2000,** 33, 7812-7818.

87. Milov, A. D.; Tsvetkov, Y. D.; Formaggio, F.; Crisma, M.; Toniolo, C.; Raap, J., The secondary structure of a membrane-modifying peptide in a supramolecular assembly studied by PELDOR and CW-ESR spectroscopies *Journal of the American Chemical Society* **2001,** 123, (16), 3784-3789.

88. Milov, A. D.; Tsvetkov, Y. D.; Gorbunova, E. Y.; Mustaeva, L. G.; Ovchinnikova, T. V.; Raap, J., Self-aggregation properties of spin-labeled zervamicin IIA as studied by PELDOR spectroscopy *Biopolymers* **2002,** 64, (6), 328-336.

89. Schweiger, A., Pulsed electron spin resonance spectroscopy: Basic principles, techniques, and examples of applications. *Angewandte Chemie International Edition* **1991,** 30, 265-292.

90. Stillman, A. E.; Schwartz, L. J.; Freed, J. H., Direct determination of rotational correlation time by electron-spin echoes. *Journal of Chemical Physics* **1980,** 73, 3502-3503.

91. Schwartz, L. J.; Stillman, A. E.; Freed, J. H., Analysis of electron spin echoes by spectral representation of the stochastic Liouville equation. *Journal of Chemical Physics* **1982,** 77, 5410-5425.

92. Saxena, S.; Freed, J. H., Two-Dimensional Electron Spin Resonance and Slow Motions. *Journal of Physical Chemistry A* **1997,** 101, 7998-8008.

93. Meirovitch, E.; Freed, J. H., Analysis of slow-motional electron spin resonance spectra in smectic phases in terms of molecular configuration, intermolecular interactions, and dyanmics. *Journal of Physical Chemistry* **1984,** 88, 4995-5004.

94. Jacobsen, K.; Oga, S.; Hubbell, W. L.; Risse, T., Determination of the orientation of T4 lysozyme vectorially bound to a planar-supported lipid bilayer using site-directed spin labeling. *Biophysical Journal* **2005,** 88, 4351-4365.

95. Xu, D.; Crepeau, R. H.; Ober, C. K.; Freed, J. H., Molecular dynamics of a liquid crystalline polymer studied by Two-Dimensional Fourier Transform and CW ESR. *Journal of Physical Chemistry* **1996,** 100, 15873-15885.

96. Borbat, P. P.; Crepeau, R. H.; Freed, J. H., Multifrequency two-dimensional Fourier transform ESR: an X/Ku-band spectrometer. *Journal of Magnetic Resonance* **1997,** 127, 155-167.

97. Freed, J. H., New technologies in electron spin resonance. *Annual Review of Physical Chemistry* **2000,** 51, 655-689.

98. Costa-Filho, A. J.; Crepeau, R. H.; Borbat, P. P.; Ge, M.; Freed, J. H., Lipid-gramicidin interactions: Dynamic structure of the boundary lipid by 2D-ELDOR. *Biophysical Journal* **2003,** 84, 3364-3378.

99. Schneider, D. J.; Freed, J. H., In *Advances in Chemical Physics*, Hirschfelder, J. O.; Wyatt, R. E.; Coalson, R. D., Eds. Wiley: New York, 1989; Vol. 63.

100. Cavalu, S.; Damian, G., Rotational correlation times of 3-carbamoyl-2,2,5,5-tetramethyl-3-pyrrolin-1-yloxy spin label with respect to heme and non-heme proteins *Biomacromolecules* **2003,** 4, 1630-1635.

101. Altenbach, C.; Marti, T.; Khorana, H. G.; Hubbell, W. L., Transmembrane protein structure: spin labeling of bacteriorhodopsin mutants. *Science* **1990,** 248, 1088-1092.

102. Millhauser, G. L., Selective placement of electron spin resonance spin labels: new structural methods for peptides and proteins. *Trends in Biochemical Sciences* **1992,** 17, 448-452.

103. Raucher, D.; Fajer, P. G., Orientation and Dynamics of Myosin Heads in Aluminum Fluoride Induced Pre-Power Stroke States: An EPR Study. *Biochemistry* **1994,** 33, 11993-11999.

104. Farrens, D. L.; Altenbach, C.; Yang, K.; Hubbell, W. L.; Khorana, H. G., Requirement of rigid-body motion of transmembrane helixes for light activation of rhodopsin. *Science* **1996,** 274, 768-770.

105. Poirier, M. A.; Xiao, W.; Macosko, J. C.; Chan, C.; Shin, Y.-K.; Bennett, M. K., The synaptic SNARE complex is a parallel four-stranded helical bundle. *Nature Structural Biology* **1998,** 5, 765-769.

106. Polese, A.; Anderson, D. J.; Millhauser, G.; Formaggio, F.; Crisma, M.; Marchiori, F.; Toniolo, C., First Interchain Peptide Interaction Detected by ESR in Fully Synthetic, Template-Assisted, Two-Helix Bundles. *Journal of the American Chemical Society* **1999,** 121, 11071-11078.

107. Merianos, H. J.; Cadieux, N.; Lin, C. H.; Kadner, R. J.; Cafiso, D. S., Substrate-induced exposure of an energy-coupling motif of a membrane transporter. *Nature Structural Biology* **2000,** 7, 205-209.

108. Perozo, E.; Cortes, D. M.; Sompornpisut, P.; Kloda, A.; Martinac, B., Open channel structure of MscL and the gating mechanism of mechanosensitive channels. *Nature* **2002,** 418, 942-948.

109. Levins, C. G.; Schafmeister, C. E., The synthesis of functionalized nanoscale molecular rods of defined length. *Journal of the American Chemical Society* **2003,** 125, (16), 4702-4703.

110. Levins, C. G.; Schafmeister, C. E., The synthesis of curved and linear structures from a minimal set of monomers. *Journal of Organic Chemistry* **2005,** 70, (22), 9002-9008.

111. Astashkin, A. V.; Hara, H.; Kawamori, A., The pulse electron-electron double resonance and "2+1" electron spin echo study of the oriented oxygen-evolving and Mn-depleted preparation of photosystem II. *Journal of Chemical Physics* **1998,** 108, (9), 3805-3812.

112. Bennati, M.; Weber, A.; Antonic, J.; Perlstein, D. L.; Robblee, J.; Stubbe, J. A., Pulsed ELDOR spectroscopy measures the distance between the two tyrosyl radicals in the R2 subunit of the E-coli ribonucleotide reductase *Journal of the American Chemical Society* **2003,** 125, (49), 14988-14989.

113. Sale, K.; Song, L. K.; Liu, Y. S.; Perozo, E.; Fajer, P., Explicit treatment of spin labels in modeling of distance constraints from dipolar EPR and DEER *Journal of the American Chemical Society* **2005,** 127, (26), 9334-9335.

114. Nakamura, M.; Ueki, S.; Hara, H.; Arata, T., Calcium structural transition of Human Cardiac Troponin C in Reconstituted Muscle Fibres as studied by site-directed spin labelling. *Journal of Molecular Biology* **2005,** 348, 127-137.

115. Bode, B. E.; Margraf, D.; Plackmeyer, J.; Durner, G.; Prisner, T. F.; Schiemann, O., Counting the monomers in nanometer-sized oligomers by pulsed electron-electron double resonance. *Journal of the American Chemical Society* **2007,** 129, 6736-6745.

116. Hinderberger, D.; Schmelz, O.; Rehahn, M.; Jeschke, G., Electrostatic site attachment of divalent counterions to rodlike Tuthenium(II) coordination polymers characterized by EPR spectroscopy. *Angewante Chemie International Edition* **2004,** 43, 4616-4621.

117. Hinderberger, D.; Spiess, H. W.; Jeschke, G., Dynamics, site binding, and distribution of counterions in polyelectrolyte solutions studied by Electron Paramagnetic Resonance Spectroscopy. *Journal of Physical Chemistry B* **2004,** 108, 3698-3704.

118. Grimsdale, A. C.; Mullen, K., The chemistry of organic nanomaterials. *Angewante Chemie International Edition.* **2005,** 44, 5592-5629.

119. Cornell, W. D.; Cieplak, P.; Bayly, C. I.; Gould, I. R.; Kenneth M. Merz, J.; Ferguson, D. M.; Spellmeyer, D. C.; Fox, T.; Caldwell, J. W.; Kollman, P. A., A second generation force field

for the simulation of proteins, nucleic acids, and organic molecules. *Journal of the American Chemical Society* **1995,** 117, 5179-5197.

120. Schafmeister, C. E., Private Publication.

121. Martin, R. E.; Pannier, M.; Diederich, F.; Gramlich, V.; Hubrich, M.; Spiess, H. W., Determination of end-to-end distances in a series of TEMPO diradicals of up to 2.8 nm length with a new four-pulse double electron electron resonance experiment. *Angewante Chemie International Edition* **1998,** 37, 2833-2837.

122. Deniz, A. A.; Dahan, M.; Grunwell, J. R.; Ha, T.; Faulhaber, A. E.; Chemla, D. S.; Weiss, S.; Schultz, P. G., Single-pair fluorescence resonance energy transfer on freely diffusing molecules: Observation of Forster distance dependence and subpopulations. *Proceedings of the National Academy of Science of the United States of America* **1999,** 96, 3670-3675.

123. Schafmeister, C. E., Molecular lego. *Scientific American* **2007,** 296, (2), 76.

124. Saxena, S.; Freed, J. H., Theory of double quantum two-dimensional electron spin resonance with application to distance measurements. *J. Chem. Phys.* **1997,** 107, (5), 1317-1340.

125. Borbat, P.; Freed, J. H., *Double-quantum ESR and distance measurements*. Kluwer Academic/Plenum Publishers: 2000; Vol. 19.

126. Pannier, M.; Veit, S.; Godt, A.; Jeschke, G.; Spiess, H. W., Dead-time free measurement of dipole-dipole interactions between electron spins. *J. Magn. Reson.* **2000,** 142, (2), 331-340.

127. Jeschke, G.; Polyhach, Y., Distance measurements on spin-labelled biomacromolecules by pulsed electron paramagnetic resonance. *Physical Chemistry Chemical Physics* **2007,** 9, 1895-1910.

128. Borbat, P.; Mchaourab, H. S.; Freed, J. H., Protein structure determination using long-distance constraints from double-quantum coherence ESR: Study of T4 Lysozyme
J. Am. Chem. Soc. **2002,** 124, (19), 5204-5314.

129. Borbat, P.; Ramlall, T. F.; Freed, J. H.; Eliezer, D., Inter-helix distances in Lysophospholipid micelle-bound α-Synuclein from Pulsed ESR measurements. *Journal of the American Chemical Society* **2006,** 128, (31), 10004-10005.

130. Arata, T.; Aihara, T.; Ueda, K.; Nakamura, M.; Ueki, S., Calcium structural transition of troponin in the complexes, on the thin filament, and in muscle fibres, as studied by site-directed spin-labelling EPR *Regulatiory Mechanisms of Striated Muscle Contraction Advances in Experimental Medicine and Biology* **2007,** 592, 125-135.

131. Hara, H.; Tenno, T.; Shirakawa, M., Distance determination in human ubiquitin by pulsed double electron-electron resonance and double quantum coherence ESR methods *J. Magn. Reson.* **2007,** 184, (1), 78-84.

132. Fajer, P. G., Directed spin labelling and pulsed dipolar electron paramagnetic resonance (double electron - electron resonance) of force activation in muscle. *J. Phys. Condens. Matter* **2005,** 17, (18), S1459-S1469.

133. Xu, Q.; Ellena, J. F.; Kim, M.; Cafiso, D. S., Substrate-dependent unfolding of the energy coupling motif of a membrane transport protein determined by double electron-electron resonance *Biochemistry* **2006,** 45, (36), 10847-10854.

134. Pfannebecker, V.; Klos, H.; Hubrich, M.; Volkmer, T.; Heuer, A.; Wiesner, U.; Spiess, H. W., Determination of end-to-end distances in oligomers by pulsed EPR *Journal of Physical Chemistry* **1996,** 100, (32), 13428-13432.

135. Piton, N.; Schiemann, O.; Mu, Y. G.; Stock, G.; Prisner, T.; Engels, J. W., Synthesis of spin-labeled RNAs for long range distance measurements by PELDOR *Nucleotides Nucleotides & Nucleic Acids* **2005,** 24, (5-7), 771-775.

136. Schiemann, O.; Piton, N.; Mu, Y. G.; Stock, G.; Engels, J. W.; Prisner, T. F., A PELDOR-based nanometer distance ruler for oligonucleotides *J. Am. Chem. Soc.* **2004,** 126, (18), 5722-5729.

137. Schiemann, O.; Weber, A.; Edwards, T. E.; Prisner, T. F.; Sigurdsson, S. T., Nanometer distance measurements on RNA using PELDOR *Journal of the American Chemical Society* **2003,** 125, (12), 3434-3435.

138. Cai, Q.; Kusnetzow, A. K.; Hubbell, W. L.; Haworth, I. S.; Gacho, G. P. C.; Van Eps, N.; Hideg, K.; Chambers, E. J.; Qin, P. Z., Site-directed spin labeling measurements of nanometer distances in nucleic acids using a sequence-independent nitroxide probe *Nucleic Acids Research* **2006,** 34, (17), 4722-4730.

139. Salnikov, E. S.; Erilov, D. A.; Milov, A. D.; Tsvetkov, Y. D.; Peggion, C.; Formaggio, F.; Toniolo, C.; Raap, J.; Dzuba, S. A., Location and aggregation of the spin-labeled peptide trichogin GA IV in a phospholipid membrane as revealed by pulsed EPR *Biophysical Journal* **2006,** 91, (4), 1532-1540.

140. Milov, A. D.; Tsvetkov, Y. D.; Formaggio, F.; Oancea, S.; Toniolo, C.; Raap, J., Solvent effect on the distance distribution between spin labels in aggregated spin labeled trichogin GA IV dimer peptides as studied by pulsed electron-electron double resonance *Phys. Chem. Chem. Phys.* **2004,** 6, (13), 3596-3603.

141. Milov, A. D.; Tsvetkov, Y. D.; Formaggio, F.; Oancea, S.; Toniolo, C.; Raap, J., Aggregation of spin labeled trichogin GA IV dimers: Distance distribution between spin labels in frozen solutions by PELDOR data *J. Phys. Chem. B* **2003,** 107, (49), 13719-13727.

142. Kawamori, A.; Katsuta, N.; Mini, H.; Ishii, A.; Minagawa, J.; Ono, T. A., Positions of Q(A) and Chl(Z) relative to tyrosine Y-Z and Y-D in photosystem II studied by pulsed EPR *Journal of Biological Physics* **2002,** 28, (3), 413-426.

143. Kawamori, A.; Katsuta, N.; Hara, H., Structural analysis of three-spin systems of photosystem II by PELDOR *Applied Magnetic Resonance* **2003,** 23, (3-4), 557-569.

144. Pornsuwan, S.; Bird, G.; Schafmeister, C. E.; Saxena, S., Flexibility and lengths of bis-peptie nanostructures by electron spin resonance. *Journal of the American Chemical Society* **2006,** 128, (12), 3876-3877.

145. Godt, A.; Schulte, M.; Zimmermann, H.; Jeschke, G., How flexible are Poly(*para*-phenyleneethynylene)s? *Angew. Chem. Int. Edit.* **2006,** 45, 7560-7564.

146. de Gennes, P.-G., *Scaling concepts in polymer physics*. Cornell Univ. Press: Inthaca, New York, 1979.

147. Goldstein, H.; Poole, C. P.; Safko, J. L., *Classical Mechanics*. 3 ed.; Addison Wesley: 2002; p 680.

148. Lagarias, J. C.; Reeds, J. A.; Wright, M. H.; Wright, P. E., Convergence properties of the Nelder-Mead simplex method in low dimensions. *SIAM Journal of Optimization* **1998,** 9, (1), 112-147.

149. Jeschke, G.; Chechik, V.; Ionita, P.; Godt, A.; Zimmermann, H.; Banham, J.; Timmel, C. R.; Hilger, D.; Jung, H., DeerAnalysis2006 - a comprehensive software package for analyzing pulsed ELDOR data. *Appl. Magn. Reson.* **2006,** 30, (3-4), 473-498.

150. Chiang, Y.-W.; Borbat, P. P.; Freed, J. H., The determination of pair distance distributions by pulsed ESR using Tikhonov regularization. *J. Magn. Reson.* **2005,** 172, 279-295.

151. Hornak, V.; Abel, R.; Okur, A.; Strockbine, B.; Roitberg, A.; Simmerling, C., Comparison of multiple Amber force fields and development of improved protein backbone parameters. *Proteins: Structure, Function, and Bioinformatics* **2006,** 65, 712-725.

152. Milov, A. D.; Erilov, D. A.; Salnikov, E. S.; Tsvetkov, Y. D.; Formaggio, F.; Toniolo, C.; RAap, J., Structure and spatial distribtuion of the spin-labelled lipopeptide trichogin GA IV in a phospholipid membrane studied by pulesd electron-electron double resonance (PELDOR). *Physical Chemistry Chemical Physics* **2005,** 7, 1794-1799.

153. Kutsovsky, Y. E.; Mariasov, A. G.; Aristov, Y. I.; Parmon, V. N., Electron spin echo as a tool for investigatin of surface structure of finely dispersed fractal solids. *Reaction Kinetics and Catalysis Letters* **1990,** 42, 19-24.

154. Banham, J. E.; Timmel, C. R.; Abbott, R. J. M.; Lea, S. M.; Jeschke, G., The characterization of weak protein-protein interactions: evidence from DEER for the trimerization of a von willebrand factor A domain in solution. *Angewandte Chemie, International Edition* **2006,** 45, (7), 1058-1061.

155. Milov, A. D.; Tsvetkov, Y. D.; Formaggio, F.; Oancea, S.; Toniolo, C.; Raap, J., Aggregation of spin labeled Trichogin GA IV dimers: distance distribution between spin labels in frozen solutions by PELDOR data. *Journal of Physical Chemistry B* **2003,** 107, 13719-13727.

156. Milov, A. D.; Tsvetkov, Y. D.; Raap, J., Aggregation of trichogin analogs in weakly polar solvents: PELDOR and ESR studies *Applied Magnetic Resonance* **2000,** 19, (2), 215-226.

157. Milov, A. D.; Tsvetkov, Y. D.; Formaggio, F.; Oancea, S.; Toniolo, C.; Raap, J., Solvent effect on the distance distribution between spin labels in aggregated spin labeled trichogin GA IV dimer peptides as studied by pulsed electron-electron double resonance. *Physical Chemistry Chemical Physics* **2004,** 6, 3596-3603.